STRESS- AND TEMPERATURE-INDUCED PHASE TRANSFORMING ARCHITECTED MATERIALS WITH MULTISTABLE ELEMENTS

by

Yunlan Zhang

A Dissertation

Submitted to the Faculty of Purdue University

In Partial Fulfillment of the Requirements for the degree of

Doctor of Philosophy

Lyles School of Civil Engineering

West Lafayette, Indiana

December 2019

THE PURDUE UNIVERSITY GRADUATE SCHOOL
STATEMENT OF COMMITTEE APPROVAL

Dr. Pablo D. Zavattieri

Lyles School of Civil Engineering

Dr. Nilesh D. Mankame

General Motors Global Research & Development

Dr. Santiago Pujol

Lyles School of Civil Engineering

Dr. Andres Arrieta

School of Mechanical Engineering

Approved by:

Dr. Dulcy Abraham

Head of the Graduate Program

To my parents Yiuying Cui and Jian Zhang.

To my wonderful husband Lucas Laughery

ACKNOWLEDGMENTS

I would like to express my gratitude to the people who helped me get to where I am today, starting with my family- Xiuying Cui and Jian Zhang for their support and understanding throughout the years while I concentrated on the research topics I was enjoying and their forgiveness on my lack of company. I would also like to thank my husband Lucas Laughery for his encouragement, patience, and support throughout my graduate studies.

Pablo Zavattieri has provided me with great opportunities and constant support. Discussions with him have given me enormous benefits to my understanding of the mechanics of materials. I appreciate Professor Mirian Velay-Lizancos, Dr. Nilesh Mankame, and Professor Santiago Pujol for all the support, encouragement, and guidance they generously provided in both research and life. I would like to thank Professor Marc Meyers, Professor Andres Arrieta, and Professor Ramses Martinez for the advice and help they gave me on the research projects on which we worked together. Thank you also to Professor Mete Sozen for providing me help, guidance, and advice whenever I needed.

I would like to thank Mehdi Shishehbor, David Restrepo, Nicolas Guarin, Nobphadon Suksangpanya, Chanhue Jeong, and Ying Wang for mentoring me. I would like to thank Kristiaan Hector, Chidubem Nuela Enebechi, Gordon Jarrold, Phani Saketh Dasika, Sanchez Medina Oscar Andres, Gavin Carter, Valeria Grillo, and Ashley Min, for assisting me with various aspects of this project. I would also like to thank Tarah Sullivan who has worked with me to investigate the shape- and strength- recovery effects of feathers. Finally, I would like to thank William Pollalis and Prateek Shah who worked closely with me to conceive the dynamic portion of this investigation and who conducted the experiments on the earthquake simulator at Bowen Laboratory.

My graduate education would not have been possible without the support from the National Science Foundation and General Motors (grant: CMMI GOALI 1538898) and Air Force Office of Scientific Research (grant: MURI FA9550-15-1-0009).

TABLE OF CONTENTS

LIST OF TABLES

LIST OF FIGURES

ABSTRACT

Author: Yunlan, Zhang. PhD
Institution: Purdue University
Degree Received: December 2019
Title: Stress- and Temperature-induced Phase Transforming Architected Materials with Multistable Elements
Committee Chair: Pablo Zavattieri

Architected materials are a class of materials with novel properties that consist of numerous periodic unit cells. In past investigations, researchers have demonstrated how architected materials can achieve these novel properties by tailoring the features of the unit cells without changing the bulk materials. Here, a group of architected materials called Phase Transforming Cellular Materials (PXCMs) are investigated with the goal of mimicking the novel properties of shape-memory alloys. A general methodology is developed for creating 1D PXCMs that exhibit temperature-induced reverse phase transformations (i.e., shape memory effect) after undergoing large deformations. During this process, the PXCMs dissipate energy but remain elastic (i.e., superelasticity). Next, inspired by the hydration-induced shape recovery of feathers, a PXCM-spring system is developed that uses the superelasticity of PXCMs to achieve shape recovery. Following these successes, the use of PXCMs to resist simulated seismic demands is evaluated. To study how they behave in a dynamic environment and how well their response can be estimated in such an environment, a single degree of freedom-PXCM system is subjected to a series of simulated ground motions. Lastly, the concept of PXCMs is extended into two dimensions by creating PXCMs that achieve superelasticity in two or more directions. Overall, the findings of this investigation indicate that PXCMs: 1) can achieve shape memory and recovery effects through temperature changes, 2) offer a novel alternative to traditional building materials for resisting seismic demands, and 3) can be expanded into two dimensions while still exhibiting superelasticity.

1. INTRODUCTION

1.1 Background

Smart materials can change properties in response to external stimuli such as temperature, magnetic fields, electric fields, moisture, and ion concentration. For example, the crystalline structure of Shape Memory Alloys (SMAs) changes with temperature, thereby changing modulus and lattice parameters[1,2]. In piezoelectric materials, a voltage creates charge redistribution resulting in mechanical strain[3]. Conversely, charge redistribution under an applied strain induces voltages. In feather shafts, the hydration process can soften and swell the beta-keratin fibers and matrix, causing the stiffer buckled fibers to reorient to their original configurations. As a result, feather shafts have the ability to recover their shape and strength with hydration[4,5]. Carnivorous plants such as the Venus Flytrap[6], exhibit movements caused by changing certain key ion concentration. These unique behaviors have prompted the use of these materials and bio-inspired alternatives in applications ranging from cardiac stents to tunable shock absorbers to high-resolution ultrasound monitors.

1.2 Past Investigations

Shape Memory Alloys are a group of smart materials that exhibit complex thermomechanical behavior. The close coupling of mechanical and thermal response in SMAs give them shape memory effect (SME) and superelasticity (SE). Shape Memory Alloys can recover from large deformations to their original shapes by temperature changes. This thermomechanical coupling also gives them superelasticity (SE), in which SMAs exhibit reversible hysteretic curves under cyclic demands[2,7,8]. These properties of SMAs have been exploited across a wide range of scales from compact actuators[9], medical implants, and minimally-invasive surgical instruments[10], to base isolation systems and energy dissipation systems that reduce the dynamic response of structures[11,12]. But SMAs have limitations, such as temperature sensitivity, low fatigue properties, high cost, and relatively low strain range when used as actuators.

The complex and useful behaviors of SMAs have motivated researchers to develop similar materials. These materials, structures, or devices have successfully achieved either shape-memory

effect or superelasticity. For example, to achieve shape memory effects, morphing structures can recover their original shape via the viscoelasticity of the bulk materials[13,14]. Hydrogel devices attain revisable snapping in response to temperature or pH-induced hydrogel shrinkage[15]. 3D-printed architectures consisting of hydrogel and shape-memory polymer (SMP), exhibit shape-memory effects via hydration and temperature-induced expansion and modulus variation[16]. Active composites made of digital polymers can be programmed to change shape and recover via temperature[17]. And digital micro 3D printing technology has made it possible to fabricate tunable microstructures that can recover to their original configurations[18].

Architected materials are an emerging class of materials composed of numerous building blocks. They can achieve novel properties via tailoring the geometry and topology of the unit cells without changing the properties of bulk materials. Several architected materials achieved superelasticity by configuring elementary building blocks without changing bulk materials properties. These architected materials have been proposed for applications such as reusable, solid state energy absorption[19–21], shock absorption or impact isolation[22,23], and reconfigurable structures[24,25]. They have also been used to create metamaterials whose mechanical properties (e.g., compressive modulus, wave propagation behavior) can be altered after the material has been fabricated[20,22,26]. Many of the materials described above are structurally two or three-dimensional because they can resist loads applied along with arbitrary directions. However, they are functionally one-dimensional because they exhibit significant energy dissipation only for loads applied along a preferred loading direction. Recent works address materials that exhibit superelasticity for loads applied along multiple directions. For example, straightforward extensions of functionally one-dimensional architected materials design for two and three dimensions have been proposed by Shan et al. and Ren et al.[27,28] Topology optimization-based automatic synthesis techniques have also been used to generate functionally 2D architected materials unit cells[29]. Two types of architected materials unit cells featuring a 5-bar planar truss and a three-dimensional tetrahedral unit cell have been proposed recently[30]. Some of the architected material designs proposed for auxetic materials[31] and shape reconfigurable materials [25] have the potential to be functionally two- and three- dimensional architected materials. Miura-ori pattern based metamaterials[32], three-dimensional arrays of spherical shells with patterned holes or Bucklicrystals[33], and tape-based three dimensional multistable structures[34], are other examples of materials that might function as

2D or 3D architected materials. However, in most of the above works, the emphasis has either been on the 1D variant of the design or on the response of the higher dimensional material designs to uniaxial loads applied along one direction. In this thesis, two designs for two-dimensional Phase Transforming Cellular Materials (PXCMs) which exhibit superelasticity are studied. The first design is based on a square motif and exhibits four axes of reflectional symmetry (similar to [27–29]). The second design is based on a triangular motif and has six axes of symmetry.

With superelasticity, PXCMs can undergo large deformations, limit forces, and remain elastic. These advantages make PXCMs attractive to structural engineering. For example, buildings exposed to earthquakes are designed to exhibit material nonlinearity in structural elements. This nonlinearity results in the yielding of steel and cracking or crushing of concrete, which results in irreversible damage even in buildings which perform as expected. Buildings that can undergo nonlinear deformations without damage would be ideal. Traditional materials are not capable of this behavior, but PXCMs are capable of it due to their superelasticity. Here, a single degree of freedom-PXCM system exposed to seismic demands is studied via experiments and FE simulations.

1.3 Objectives and Goals

The overall goal of this research is to assess the feasibility of a new class of architected materials that mimic novel properties of active materials (i.e. shape-memory effects and superelasticity of Shape Memory Alloys). More specifically the focus of this work is to create design concepts that employ simple combinations of materials that do not necessarily have any particular active property (such as shape-memory, etc.). Additionally, this work sought to architect materials that can mimic stress- and temperature-induced phase transformations observed in SMAs. Furthermore, to create multi-dimensional architected materials that can exhibit superelasticity, rather than the one-dimensional variant of the design. An additional goal of this work is to understand the response of these materials under loads applied along multiple axes of symmetry rather than the response of higher dimensional material designs due to uniaxial loads applied along one preferred direction. Eventually, utilizing the superelasticity of this new class of architected materials to apply on seismic design.

The objectives of this work are shown as following:

1. To extend the concept of PXCMs to functionally 2D PXCMs that can achieve superelasticity in multiple directions.
2. To establish the analytical, numerical, and experimental programs for the design and analysis of the mechanical behavior of functionally bidimensional PXCMs.
3. To develop design guidelines for the development of PXCMs that can achieve shape-memory effects through external/non-mechanical stimuli.
4. To develop and analyze bioinspired PXCMs with shape-memory properties.
5. To explore potential and innovative applications of PXCMs.

1.4 Thesis Organization

The rest of the thesis is organized as follow:

Chapter 2 presents the design concept of thermal-induced PXCMs. The design guide is provided to determine geometry and materials combination of PXCMs, in order to achieve phase transformation at a certain temperature. The analytical, experimental, and numerical validations of this design concept is also included in this chapter.

Chapter 3 includes the study of shape recovery effects of feathers. A new bio-inspired PXCMs system can achieve shape-memory effects is also proposed in this chapter.

In Chapter 4, a preliminary study of the application of 1D PXCMs in structural engineering is presented. The response of a single degree of freedom with 1D PXCMs and mass system under various seismic demands are studied. The experiments grogram and numerical analysis are included in this chapter.

Chapter 5 shows the process of extending the concept of functional one-dimensional PXCMs into two-dimension. The two types of 2D PXCMs design, *S*- and *T*-type 2D PXCMs, are demonstrated. The energy dissipation capacity and sensitivity of these two types of 2D PXCMs along multiple axes of symmetry are presented in this chapter. The analytical, experimental, and numerical validations of this design concept is also included in this chapter. Preliminary results and plan of the future study on the response of 2D PXCMs undergo the concentrated loading condition is also presented in this chapter.

Finally, the discussions and conclusions of the most important results obtained from this work are summarized and concluded in Chapter 6.

2. TEMPERATURE-INDUCED PHASE TRANSFORMING CELLULAR MATERIALS

The work in this chapter was done in collaboration with Nilesh D. Mankame from General Motors, David Restrepo from The University of Texas at San Antonio, and Mirian Velay-Lizancos from Purdue University.

2.1 Overview

Shape Memory Alloys are a group of smart materials that exhibit complex thermomechanical behavior. The close coupling of mechanical and thermal response in SMAs give them shape-memory effect (SME), wherein they can recover from large deformation back to its original shape via temperature variation. The unique combination of crystal lattice configurations and thermodynamics (energy and entropy) associated with nearly equiatomic alloys also gives them superelasticity (SE), wherein SMAs exhibit reversible hysteretic curves under cyclic demands[2,7,8]. These properties of SMAs have been exploited across a wide range of scales from compact actuators[9], medical implants, and minimally invasive surgical instruments[10], to base isolation systems and energy dissipation systems to reduce the dynamic response of infrastructure[11,12]. But SMAs have limitations, such as low fatigue properties, high cost, and relatively low strain range when used as actuators. The complex and functional behaviors of these materials have motivated researchers to develop similar materials. These materials, structures, or devices have gone successfully achieved one of shape-memory or superelasticity. For example, morphing structures can recover their original shape via the viscoelasticity of the bulk materials[13,14]. Hydrogel devices attain revisable snapping in response to temperature or pH-induced hydrogel shrinkage[15]. 3D printed architectures composed of hydrogel and shape-memory polymer (SMP), exhibit shape-memory due to the temperature and hydration induced formation or destruction of soft cross-links between parts of the same or adjacent chains[16]. Active composites made of digital polymers can be programmed to change shape and recover via temperature[17]. And digital micro 3D printing technology has made it possible to fabricate tunable microstructures that can recover to the original configurations[18]. Several architected materials also can achieve superelasticity by configuring the elementary building blocks without changing the bulk materials properties. 1D metamaterials

comprise a number of compliant mechanisms building blocks, such as curved beams[19,35] and constrained tilted beams[36], exhibit superelasticity via the snap-through behavior of these building blocks. 2D metamaterials are composed of bistable mechanisms as building blocks exhibit SE when loads come along multiple directions[25,37]. These works have successfully achieved one of two novel behaviors of SMAs, shape-memory effect or superelasticity, but not both. An architected material that can perform both, stress- and temperature-induced phase transformation by using simple mechanisms and combination of materials is proposed here.

2.2 Analytical model, design, and validation

A design concept that employs a simple combination of materials that do not require active properties such as shape-memory to design materials in order to mimic the stress- and temperature-induced phase transformation observed in Shape Memory Alloys (SMAs) is presented. We demonstrate this design concept using Phase Transforming Cellular Materials (PXCMs) fabricated with two widely-used digital materials in additive manufacturing. Our PXCMs exhibit the complex thermomechanical behavior of SMAs. The superelastic behavior of PXCMs is described in our previous works on 1D and 2D PXCMs[19]. This study focusses on how to design and tune PXCMs to exhibit shape-memory effects via temperature variation.

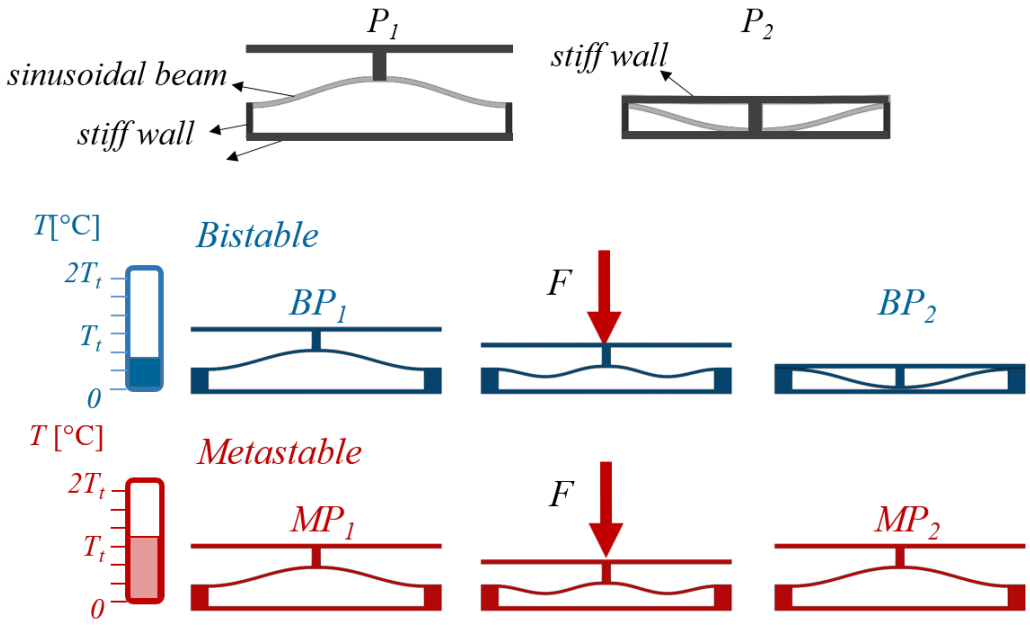

Figure 2.1: A PXCM building block is bistable at a low temperature and is metastable at a high temperature.

Shape Memory Alloys can transform between lattice phases through temperature and stress stimuli. Here, Figure 2.1 shows how PXCMs can also transform between geometric configurations (phases), BP_1, BP_2, MP_1, and MP_2 via temperature and stress stimuli. The geometric configurations shown in Figure 2.1 define phases at the elementary building block level. The transitions between these configurations are denoted as phase transformations. In these PXCMS, a building block consists of a bistable/metastable (*B/M*) sinusoidal beam with stiff walls at its midpoint and at its ends as supports. It can transform from P_1 to P_2 via an external load (Figure 2.1). Once the load is released, a bistable building block remains at P_2, but a metastable building block will return to P_1 without an external force being applied. Here, the phase transformation of in demonstrated on a building block (Figure 2.1).

One key aspect of the phase transformation shown in Figure 2.1 is that the behavior of a PXCM building block switches from bistable (*B*) to metastable (*M*) at a transition temperature (T_t). When the current temperature T is smaller than T_t, a building block is bistable (Figure 2.1, blue row). We define the configuration of this building block under zero external load in its original stable configuration as BP_1. If an external load is applied, the building block can transform into its second stable configuration, BP_2 (Figure 2.1 blue row). Because BP_2 is a stable configuration, the building block will remain in BP_2 even when the applied load is removed – an external force is needed to return to BP_1. When T exceeds T_t, the building block is metastable (Figure 2.1, red row), meaning an applied load can transform the block from MP_1 to MP_2 via stress. In contrast to the previous case, in this case, the building block will return to MP_1 if the load is released (i.e., no external force is needed).

We define when $T > T_t$, $T=T_h$ and $T < T_t$, $T=T_l$ by specifying the materials and geometry of the PXCM. The Force-displacement (*F-d*) relationship of the generalized bistable and metastable building blocks undergoing both stress-induced phase transformation cases are shown in Figure 2.2 and Figure 2.3. The local maximum and minimum forces are defined as the peak force, F_p, and the valley force is defined as F_v. The *F-d* relationship can be divided into three regimes as shown in Figure 2.2 and Figure 2.3. Regime 2, between F_p and F_v, exhibits negative stiffness. Regimes 1 and 3 exhibit positive stiffness. When $T=T_h$, $F_v > 0$ the building block is metastable as shown by

the red line in Figure 2.3. When $T=T_l$, $F_v < 0$ the building block is bistable as shown by the blue line in Figure 2.2. The ratio r_b is defined as the ratio of $-F_v/F_p$ to describe the bistability of a building block. The bistability of a building block increases with the value of r_b. When r_b is positive, a building block is bistable, and when it is negative a building block is metastable. As temperature increases, $F_v \rightarrow F_p$, and $r_b \rightarrow -1$, and consequently the negative stiffness regime disappears. This leads the building block to behave as an elastic spring which is neither bistable nor metastable.

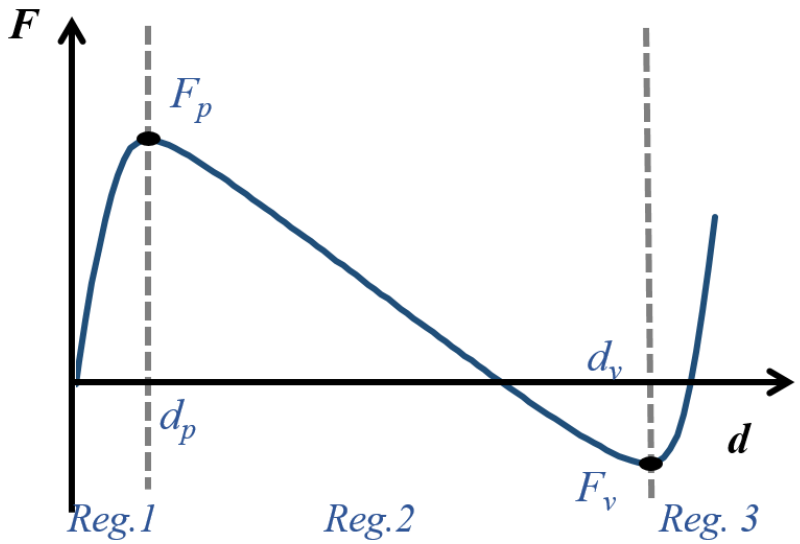

Figure 2.2: *F-d* relation of a building block when it is bistable.

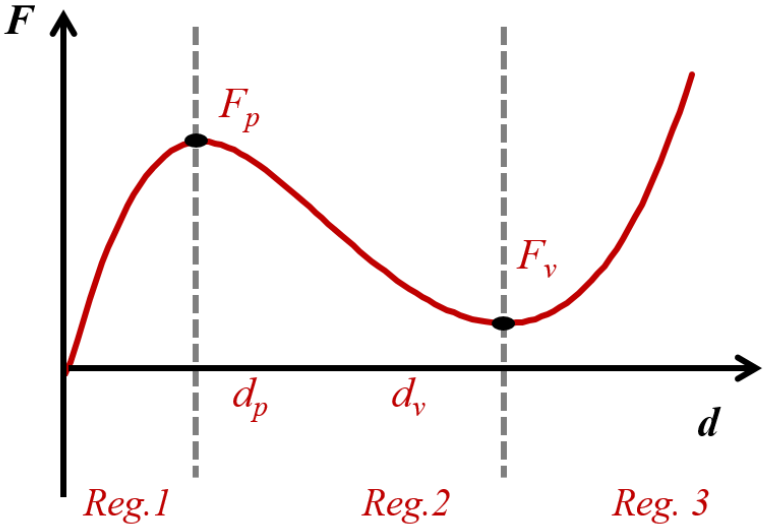

Figure 2.3: *F-d* relation of a building block when it is metastable.

As an analogy to SMAs: MP_1, MP_2, BP_1, and BP_2 are equivalent to austenite (A), detwinned martensite (M^+), thermal martensite (M^+/M^-), and detwinned martensite (M^+) phases (Figure 2.4). Here we refer the twinning and detwinning process between M^+ and M^- also as phase transformation. Parallels between phase transformations of PXCMs and in SMAs are illustrated in Figure 2.4. Temperature-induced phase transformation takes place when the temperature in a building block in BP_2 increases from T_l to T_h without external forces. When the material becomes metastable, the material undergoes a phase transformation from MP_2 to MP_1 without any external force. This process is equivalent to SMAs transforming from Austenite (A) to a mixture of twinned and detwinned martensite phases (M^-/M^+) by decreasing temperature[2]. This temperature-induced phase transformation process is schematically plotted in the stress-strain-temperature (σ-ε-T) diagram in Figure 1c as points ③ → ④ → ⑤ → ⑥. When temperature reaches T_l, stress can induce a building block to transform from BP_1 into BP_2, similar to how SMAs transform from M^-/M^+ into M^+ (points ⓪ → ① → ② → ③ in the same figure). SMAs can recover from detwinned martensite to austenite (M^+ to A) by increasing temperature. Instead of holding an external force-free condition at T_h, if a loading-unloading cycle applies to this PXCMs building block, the $\sigma - \varepsilon$ relation shows reversible hysteresis corresponding to points ⑥ → ⑦ → ⑧ → ⑨ → ⑩ → ⑪ in Figure 2.4. This reversible hysteresis is equivalent to the reversible transformation of SMAs from $A \rightarrow M^+ \rightarrow A$ via stress, also known as superelasticity.

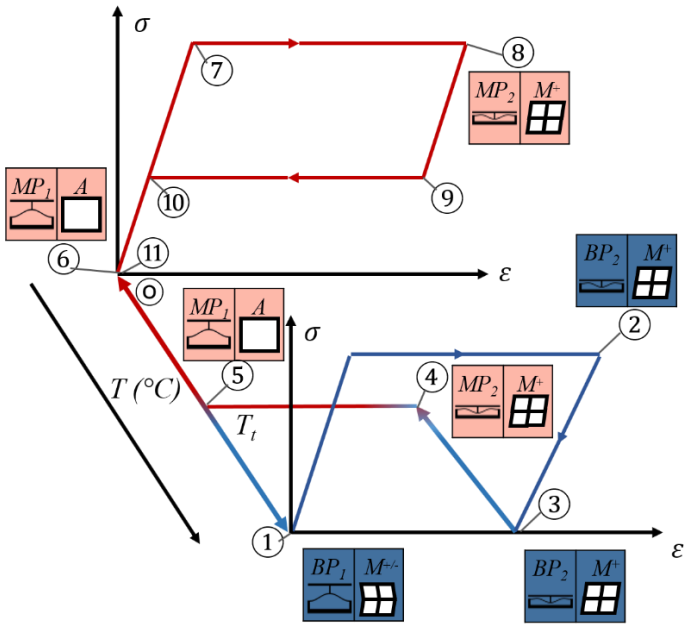

Figure 2.4: A schematic plot shows the analogy of PXCMs to SMAs through stress- and temperature-induced phase transformation diagram.

The *F-d* relationship of a building block is determined by both the thermomechanical properties of its base materials and geometry. Differences in the mechanical properties of the base materials, m_1 and m_2, are similar at low temperatures but these differences increase with temperature (Figure 2.4). In our PXCMS, the stiff walls at the ends of the sinusoidal beam are made of material m_2, whereas the remaining structure is made of material m_1. Figure 2.5 shows such a building block exhibits the SME.

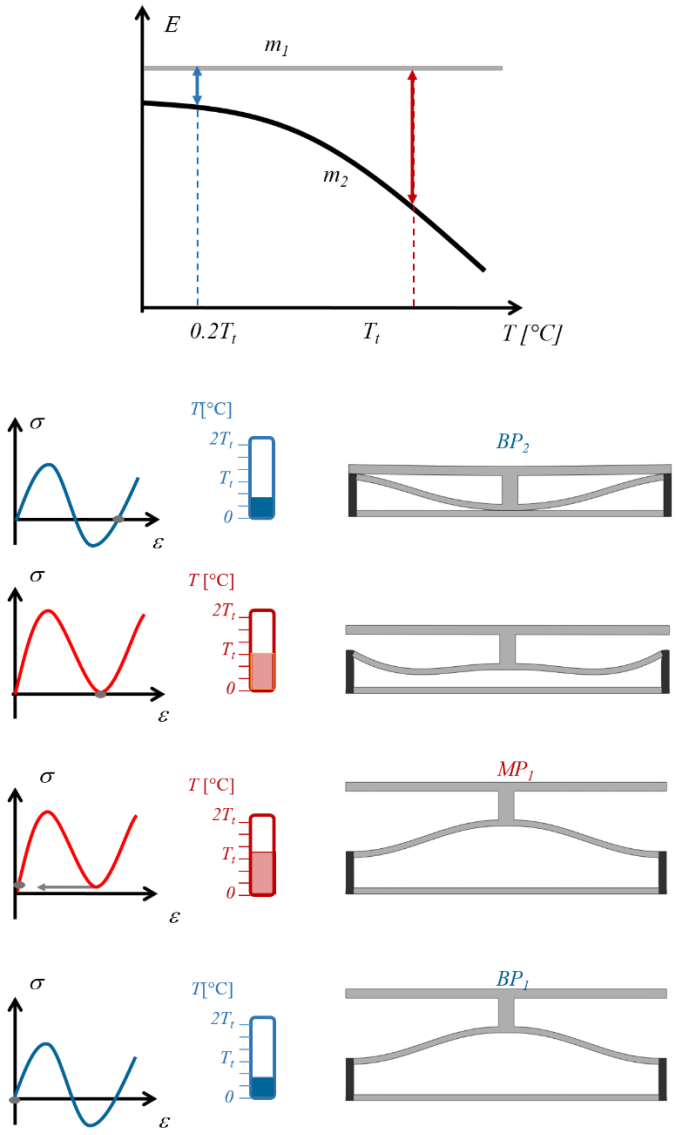

Figure 2.5: A PXCM building block made of m_1 and m_2 transforming between phases via temperature variation.

Figure 2.6 shows a 3D-printed PXCM prototype comprising three of these building blocks. This prototype was fabricated using a multi-material polymer 3D printer Connex 350. The shape of the sinusoidal beam follows the expression: $Y = \left(\frac{A}{2}\right)[1 - \cos(\frac{2\pi X}{\lambda})]$, where A is the amplitude and λ represents the wavelength Figure 2.7, A group of nondimensional parameters $\pi_1 = \frac{t}{\lambda}, \pi_2 = \frac{A}{\lambda}, \pi_3 = \frac{t_s}{\lambda}, and\ \pi_4 = \frac{E_2}{E_1}$, determine how the *F-d* relationship of PXCMs undergo the phase transformation at different temperatures (see Appendix A). Here, t is the thickness of the sinusoidal beam, t_s is the width of a stiff wall, and k_a and k_s represent the axial stiffnesses of the sinusoidal beam and stiff walls, respectively[19,38,39]. Here, stiffness is approximated as $k_a = \frac{E_1 bt}{\lambda}$ and $k_s = \frac{E_2 bt}{2t_s}$ where E_1 and E_2 are the elastic moduli of m_1 and m_2, and b is the out of plane thickness of the building block (Figure A1). The variable c describes the level of the stiffness the stiff walls provide to a building block. The bistability of PXCMs is governed by the nondimensional parameters $c = \frac{1}{2\pi_3/\pi_4+1} = \frac{1}{k_a/k_s+1}$ and $Q = \pi_2/\pi_1 = A/t$. If the geometry and base materials of a building block are known, the value of c depends only on the temperature. The variable c ranges from 0 to 1, where larger values correspond to higher transitional constraints from the two stiff walls, and thus higher bistability. When $k_s \gg k_a$, $c \rightarrow 1$, and the building block is equivalent to a sinusoidal beam under the clamped-clamped boundary condition. As $k_s \ll k_a$ and $c \rightarrow 0$, the building block is equivalent to a free sinusoidal beam with no constraint (Figure A2).

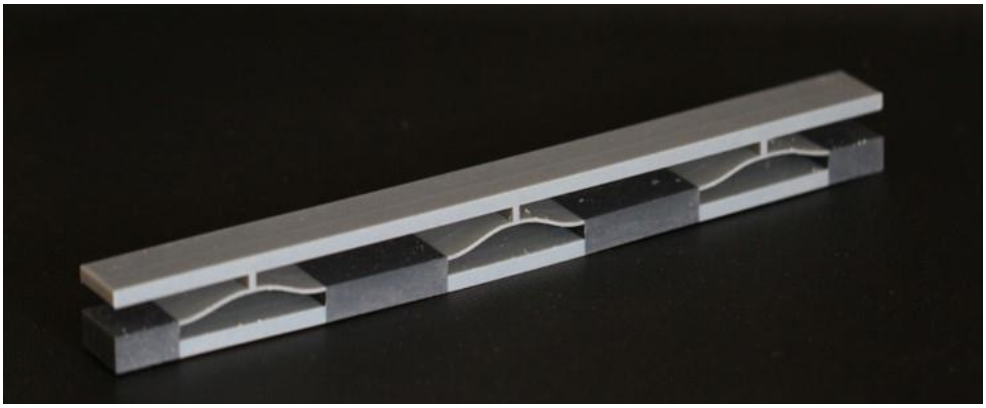

Figure 2.6: A 3D printed PXCM sample.

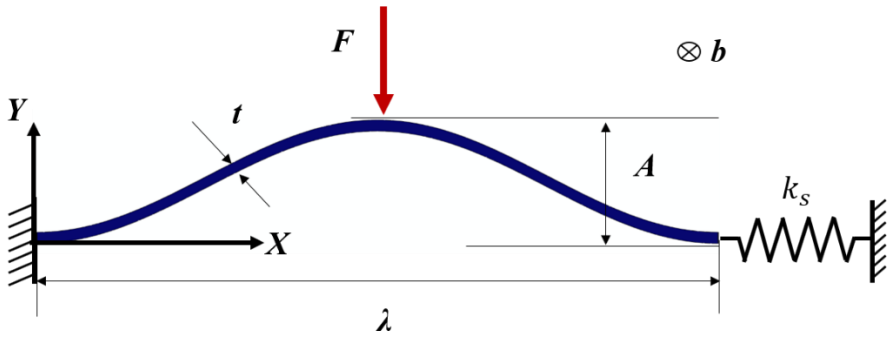

Figure 2.7: PXCM building block can be simplified into a sinusoidal beam-spring model.

If a PXCM is made of a single homogeneous isotropic material, the parameter Q governs bistability[19,38,39]. Although PXCMs typically comprise two materials, at T_l they behave as a homogeneous isotropic material because the elastic modulus of m_1 and m_2 are similar (Figure 2.5). As a result, the bistability of PXCMs at T_l is still governed by the parameter Q. At the transition temperature, T_t, the elastic modulus of m_2 becomes much lower than the elastic modulus of m_1. Accordingly, c decreases to a point where the stiff walls (material m_2) can no longer provide enough constraint to keep the sinusoidal beam bistable (Figure 2.5). This makes the unit cell transition from being bistable at $T_l << T_t$ to being metastable at $T_h >> T_t$.

To capture this variation, an analytical model was derived by simplifying a PXCM building block as a sinusoidal beam connected to a translational spring (Figure 2.7). The normalized force-displacement (f-δ) relationship of a building block undergoing single phase transformation is derived by using superposition buckling mode method. This relationship is described by Eq. 2.1-Eq. 2.3, where p is the axial force in a sinusoidal beam. During the phase transformation, the building block goes through three primary buckling modes, *mode 1, mode 2, and mode 3* (Figure A3). At the beginning and end of phase transformation, the axial force p is small, and the building block transforms through *mode 1*. Once p increases to the threshold of *mode 2* or *mode 3*, the building block then switches to *mode 2* or *mode 3* which depends on whether the rotational motion in the middle of the building block is constrained. Toward the end of phase transformation, p reduces to the threshold of *mode 1*. As a result, the building block switches back to *mode 1*. The f-δ relationship of a sinusoidal beam going through these three modes is denoted by f_1-δ, f_2-δ and f_3-δ. Here, f_1 intersects with f_2 and f_3 twice. The intersection between f_1- δ, f_2- δ and f_3- δ is where

the sinusoidal beam switches from *mode 1* to *mode 2* or *mode 3*. The f- δ relation is the combination of f_1-d outside two points of intersection and f_2- δ or f_3- δ between the two points of intersection. The Appendix A contain additional details about the derivation of the equations governing this response. These analytical equations are essential tools to design PXCMs achieving SME.

$$f_1 = \sum_{j=1,5,9,13\ldots}^{\infty} \frac{4(N^2 - N_1^2)}{N_j^2(N^2 - N_j^2)^2} f_1{}^2 - N_1^2 f_1 + \frac{N^2(N^2 - N_1^2)^2}{12Q^2c} - \frac{N_1^2 N^2(N^2 - 2N_1^2)}{16} = 0 \quad \text{Eq. 2.1}$$

Where $N^2 = \frac{pl^2}{EI}$,

$$f_2 = \frac{1}{\sum_{j=1,5,9,13\ldots}^{\infty} \frac{8}{N_j^2(N_2{}^2 - N_j^2)^2}} \left(\frac{N_2^2}{N_2^2 - N_1^2} - \delta \right) \quad \text{Eq. 2.2}$$

$$f_3 = \frac{1}{\sum_{j=1,5,9,13\ldots}^{\infty} \frac{8}{N_j^2(N_3{}^2 - N_j^2)^2}} \left(\frac{N_3^2}{N_3^2 - N_1^2} - \delta \right) \quad \text{Eq. 2.3}$$

Figure 2.8 illustrates how the $\sigma - \varepsilon$ relation and bistability (r_b) of a building block (Q=A/t=3.5) is influenced by c from FE simulations (details in section A3). Here, σ is F divided by gross cross-section area and ε is d divided by the original height of the building block. The bistability of a building block is described by $r_b = -F_v / F_p = -\sigma_v / \sigma_p$. Figure 2.8 indicates that the bistability of this building block decreases with c, which depends on temperature (Figures A6-8). Hotter temperatures decrease c and r_b (Figures A6 &7), therefore decreasing bistability. When the temperature has decreased such that c=0.14, the building block switches from bistable to metastable ($\sigma_v \geq 0$ and $r_b \leq 0$). Subsequently, without any external mechanical loading, the building block can transform from BP_2 to MP_1 simply by heating to T_h such that c>0.14.

There is a limitation on T_h. If temperature continues to increase, eventually $\sigma_v \approx \sigma_p$ and $r_b \rightarrow -1$. As a result, the negative stiffness regime 2 starts to disappear along with distinct phases. Figure 2.9, a phase diagram, illustrates this phenomenon. Each point represents σ_v or σ_p of the building block shown in Figure 2.9 at the corresponding temperatures. At low temperatures, the building block is bistable and it can transform from BP_1 to BP_2 via an external force which causes stress to exceed σ_p. The building block can also return to BP_2 when the external force causes stress reach to

σ_v. At high temperatures, the building block is metastable. When stress reaches σ_p, it transforms from MP_1 to MP_2. Once the stress decreases below σ_v, the block can return to metastable state MP_1. If the temperature is too high, σ_p and σ_v become too close to distinguish. As a result, phase transformation cannot occur.

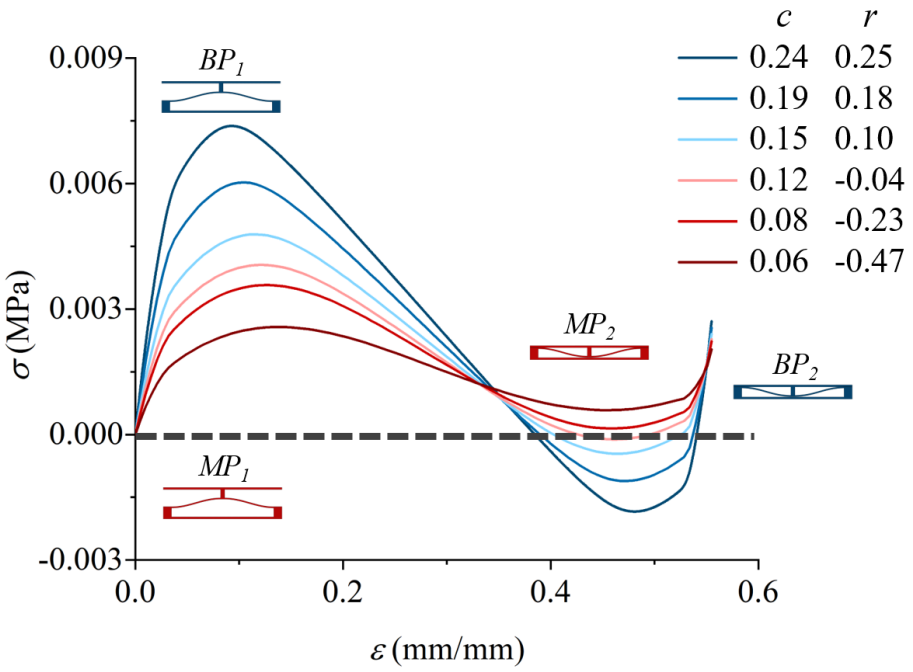

Figure 2.8: $\boldsymbol{\sigma}$-$\boldsymbol{\varepsilon}$ relation of a PXCM building block corresponding to different c.

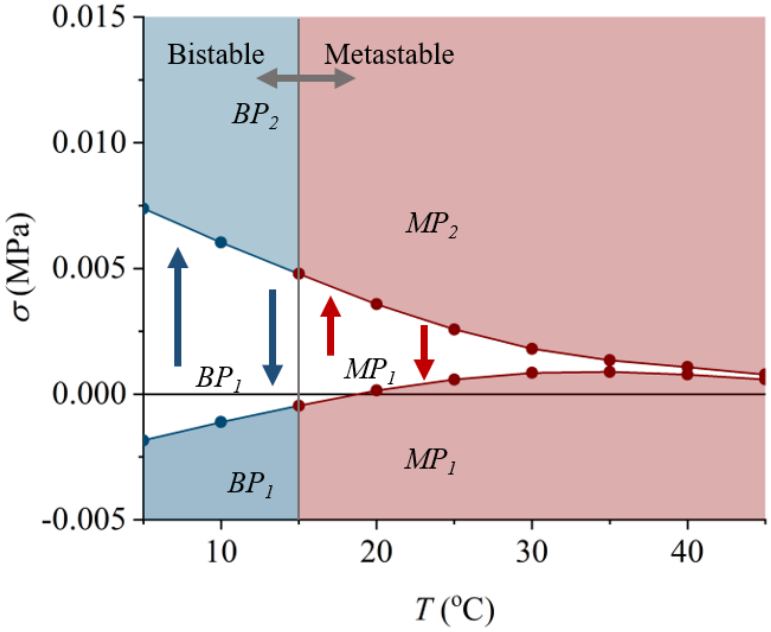

Figure 2.9: Phase transformation of a PXCM building block through temperature and stress.

Figure 2.10 shows how bistability in a PXCM varies with Q and c (see details in secssion A4 in Appendix A). In this figure, blue denotes a bistable region and pink denotes a metastable region. The red curve and black dots represent the critical value of c from analytical equations and FE simulations when a PXCM building block switches between metastable and bistable. Regardless of the geometry or base materials of a building block, there is a unique c_{cr} that depends only on Q. Different geometries or material combinations of PXCMs with the same Q would have the same c_{cr} (Figure A9). A building block is bistable when c is larger than c_{cr}, and metastable when c is smaller than c_{cr}. To program PXCMs to transform between phases, the geometry of the building block and base materials need to be selected to ensure $c=c_{cr}$ at the desired T_t.

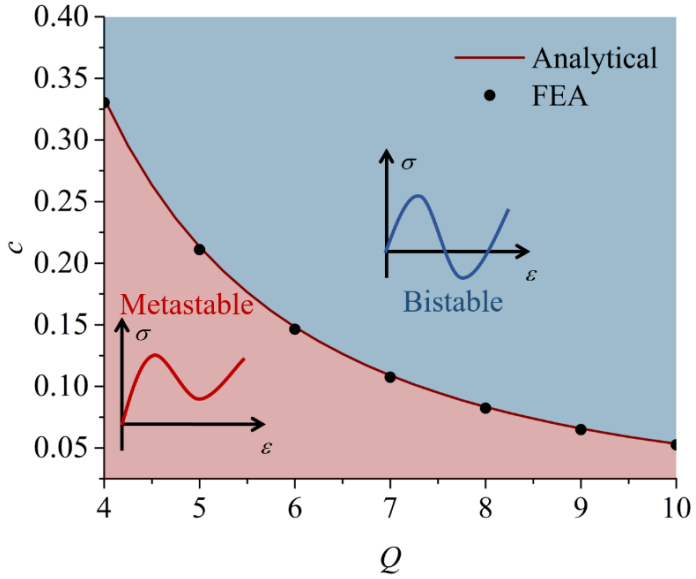

Figure 2.10: c determines the bistability of PXCMs.

In Appendix A4, the method to create design maps for PXCMs is provided. Figure 2.11 shows an example of a design map of a PXCM made of DM_8530 as m_1, and DM_9895 as m_2 (see Figure A5). In this design map $\pi_3 = 0.02$ is fixed and λ=60 mm has been selected because they are the major factors determining the size of PXCMs. Each curve illustrates the transition temperature, T_t, of building blocks with a constant $\pi_2 = \frac{A}{\lambda}$ but different Q. For smaller values of π_2, higher temperatures are required to achieve phase transformation. When π_2 is constant and Q is large, the PXCM becomes more bistable, and higher temperatures are required to transform it from BP_2 to MP_1. More design maps in which other parameters are fixed are shown in Appendix A4.

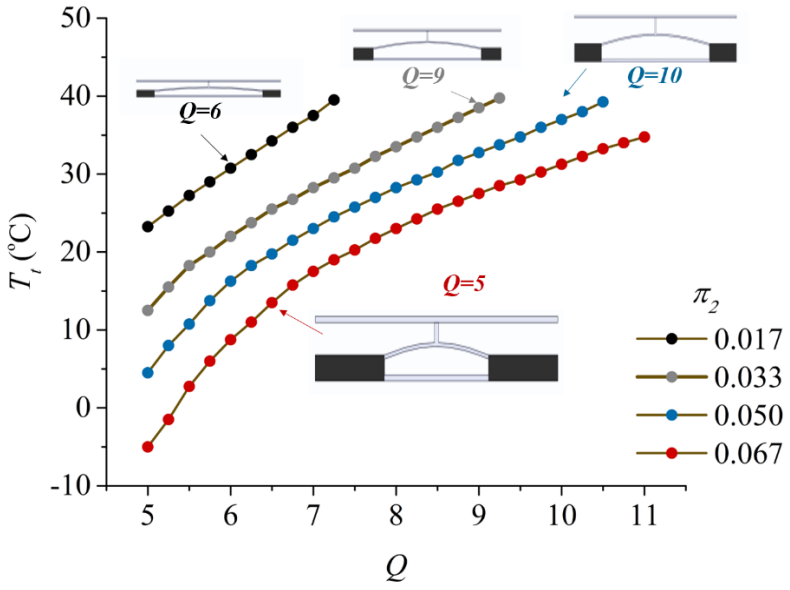

Figure 2.11: Design diagram illustrates the T_t of different PXCM building blocks with different geometry parameters.

To show how to design PXCMs to exhibit the shape-memory effect (SME), a PXCM sample was designed and fabricated for experimental testing. This sample consists of three building blocks made of DM_8530 (m_1) and DM_9895(m_2), designed to transform from BP_2 to MP_1 at T_t=18 °C (Figure 2.6 & Figure 2.12a). The demonstration procedure was as follows:

The specimen is placed on an aluminum 8020 frame. Two aluminum L shape angles were fixed on both sides of the sample to eliminate the move in *X* direction.

(1) At T=T_l=8°C, an applied force compressed the sample such that it transformed from BP_1 to BP_2 and unloaded (Figure 2.12 b),

(2) The sample kept in BP_2 at T_l for 10 minutes.

(3) The temperature increased gradually to T_h=22°C and T_t was recorded.

Figure 2.12 b-f shows the SEM process from both the experiment and FE simulation. As expected, the sample remained in state BP_2 for 10 minutes at 8°C. As the temperature increased, there was no observable change until the temperature reached 18°C (Figure 2.12 b-e). At 18°C, the PXCM began to transform to MP_1. The transformation was complete by 19°C. The transition temperature T_t, obtained from both FE simulation and experiment, were close to the design value derived by the analytical equations (Eq.2.1-2.3). The building blocks made of m_1 exhibited SME. The glass transition temperature of DM_8530 (m_1) is around 48°C, indicating the shape-memory properties

of the base materials did not interfere with the phase transformation. That the sample remained in BP_2 for 10 minutes and did not transform until 20 minutes had passed and $T=T_t$ =18 °C indicates the design method is able to predict the recovery temperature.

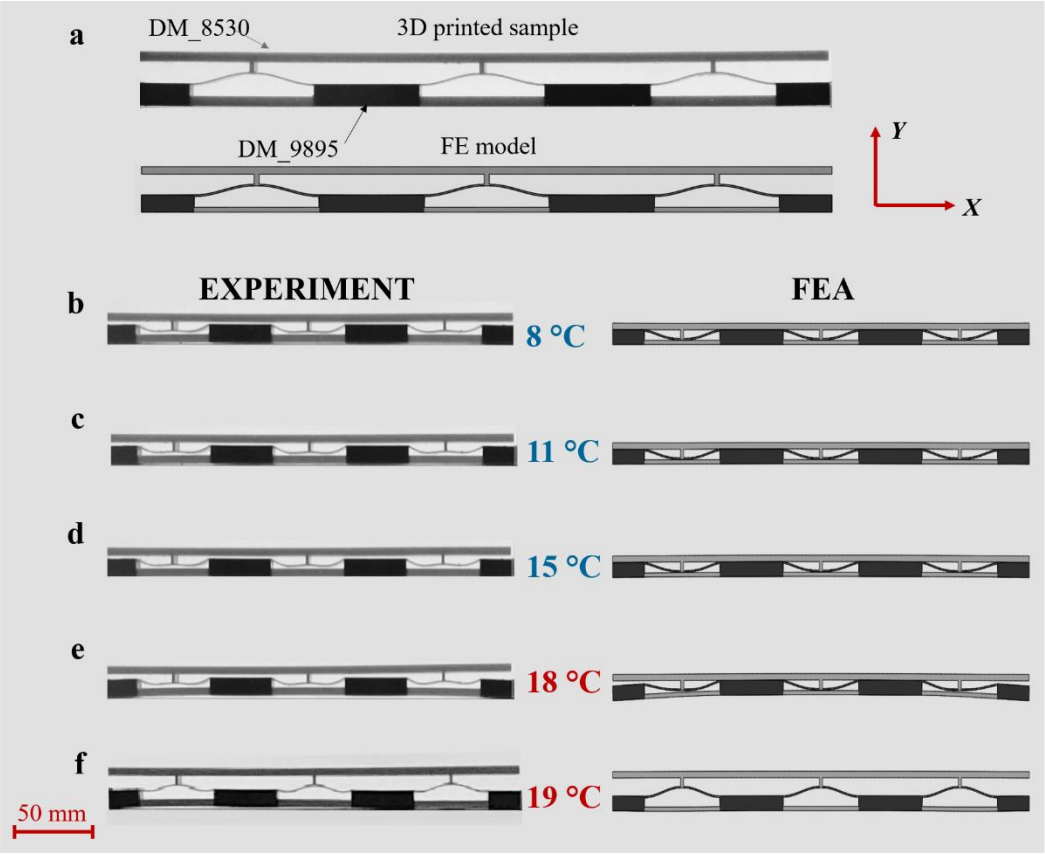

Figure 2.12: Recovery process of the sample from experiments and FEA at different temperature.

2.3 Work and Actuation

The study has demonstrated how PXCMs exhibit SEM and SE like SMAs via FE simulation and experiment. Next, how PXCMs can be used for free recovery (deployable structures) or constrained (prestressed fittings, valves, or actuators) applications like SMAs are investigated. Figure 2.13 shows the *F-d* relation of a PXCM building block at 10, 20, and 28 °C. The valley force, F_v, increases with temperature, and becomes zero when T=20 °C (for T_t=20 °C and F_v=0). This building block can be transformed from BP_1 to BP_2 at 10 °C by applying stress. Under the same temperature, it would remain at BP_2 even after the stress is released. Under the stress-free condition, if temperature increases, the building block can transform from BP_2 to MP_1 at 20 °C. If

a weight w is set atop this building block, the T_t is required to transform the building block from BP_2 to MP_1 with the weight will become the temperature corresponding to $F_v = w$. Therefore, a higher temperature is required to achieve phase transformation if a building block has a load applied on top. A number of simulations were created following this test procedure and are shown in Figure 2.14. Each red dot represents F_v of the same building block under different temperatures. Each black dot represents T_t when this building block transforms from BP_2 to MP_1 with the corresponding weight on top of it. The two curves nearly overlap, indicating this methodology is correct for determining the required temperature T_t to trigger PXCMs to lift a weight.

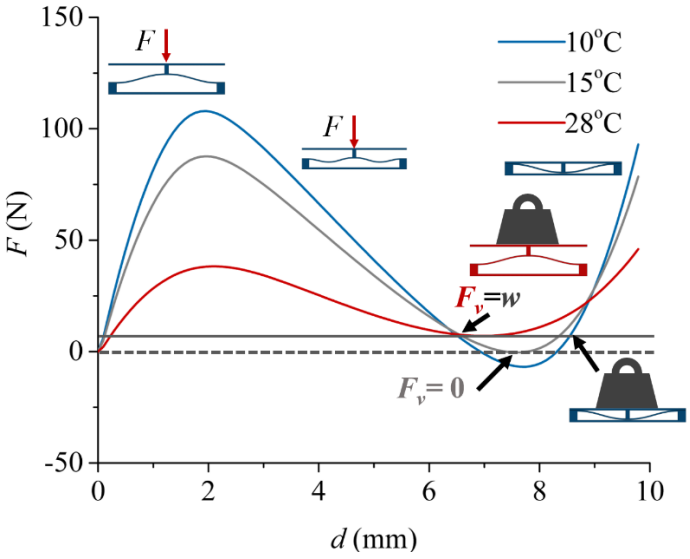

Figure 2.13: A PXCM building block can lift a weight $w=F_v$ at the recovery temperatures.

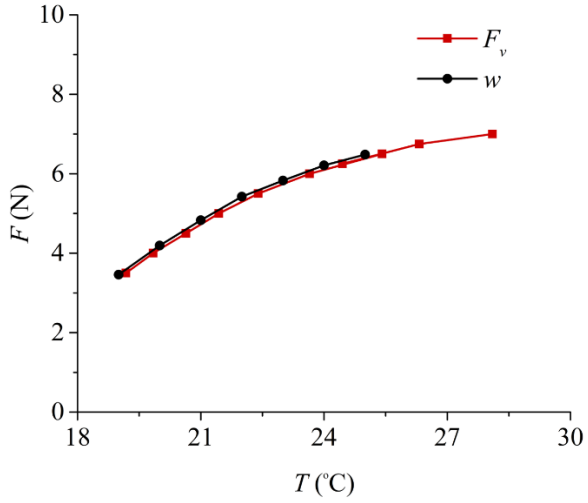

Figure 2.14: F_v of the building block at various temperatures and the weight this building block can lift at different temperatures.

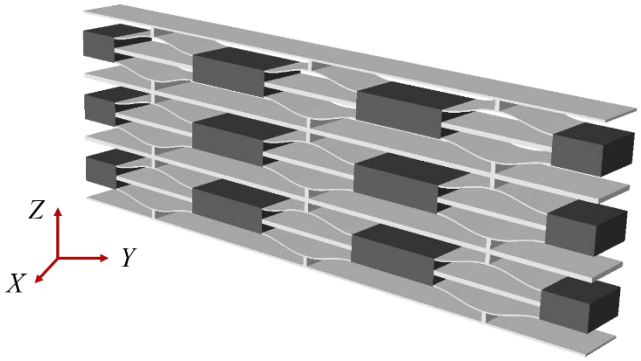

Figure 2.15: A 6 by 3 building blocks sample for FE simulation.

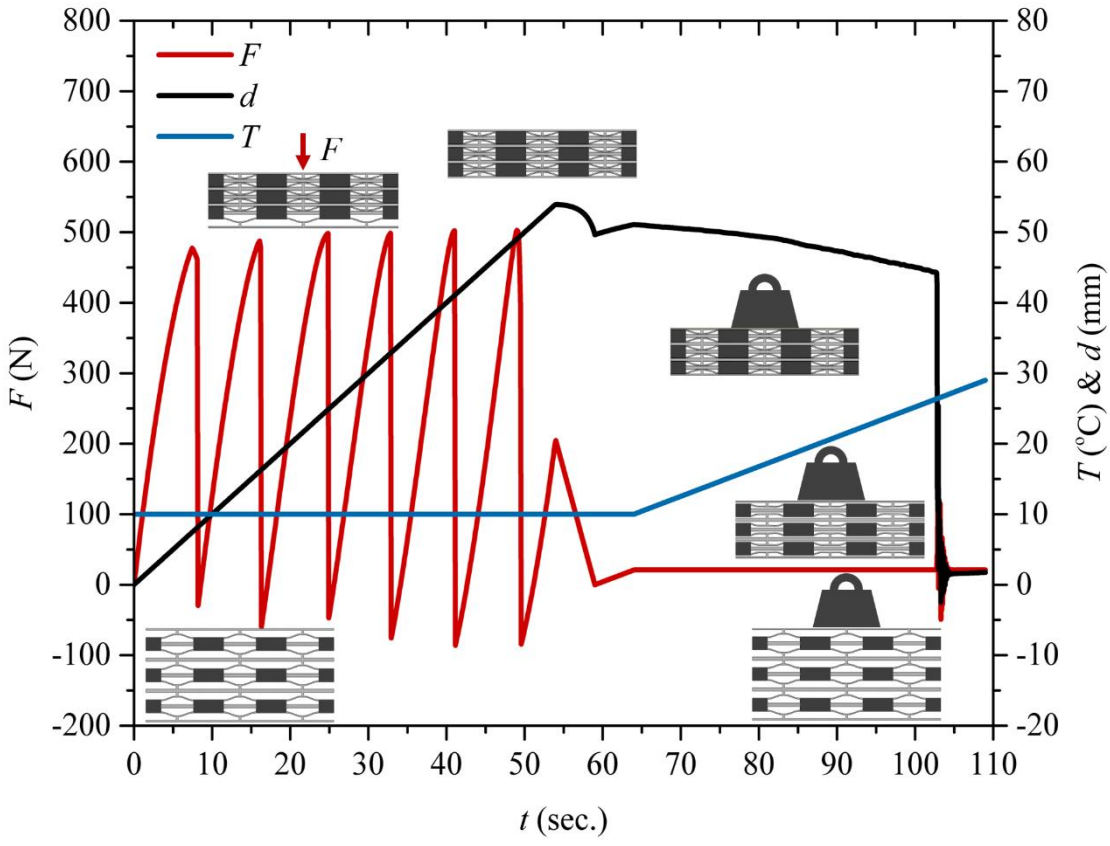

Figure 2.16: *F*, *d*, and *T* vary with *t* during the work process.

To prove this concept, a FE simulation of a 6x3 building block PXCMs model subjected to a stress and temperature cycle was conducted (Figure 2.15). At 10°C, this model was compressed to transform from BP_1 to BP_2. The model remained at BP_2 after the external force is released. Then a weight w=21 N was applied on top of this model as it remained at BP_2. Gradually, the temperature

was increased until the weight was raised, and the model recovered to MP_1. Figure 2.16 presents how the reaction force (F), temperature (T), and displacement (d) of the building block model vary with time. From t=0 to 55 sec, the temperature was held at 10°C and the model was compressed from BP_1 to BP_2 at a constant rate. The F-t curve exhibited a seesaw shape, where the six peaks represent the six rows of building blocks transforming progressively. From t=55 to 60 sec, the model stayed at BP_2 without external loads ($F \rightarrow 0$). From t=60 to 65 sec, the temperature was kept constant and a 21 N weight was applied on top of the sample. The model remained at BP_2. From t=65 to 110 sec., the temperature was increased from 10°C to 30°C. As expected, the model transformed from BP_2 to MP_1 at 28 °C. The phase transformation process was observed by a sudden change in displacement when the temperature reached 28 °C.

2.4 PXCMs Designs

Here, three types of PXCM designs are created. In this chapter has detailed *Type I*. The other two types of PXCMs are also able to mimic the SE and SEM of SMAs. The phase transformations of the three designs are presented in Figure 2.17a-c. *Type I* design has the stiff walls made of material m_2 and the remainder made of material m_1. The phase and bistability of *Type I* PXCMs depends on the level of constraint that stiff walls provide to the building block. This constraint is tuned by temperature (Figure 2.18). In *Type II* PXCMs, the center stiff wall is made of m_2 and the remainder is made of m_1. When temperature increases, the center bar softens and allows the sinusoidal beam to transform back to its original configuration through an asymmetric rotational mode (Figure 2.18 a & c). In *Type III* PXCMs, a small portion of the sinusoidal beams around their inflection points is made of m_2 and the remainder is made of m_1. Under low temperatures, each unit cell is similar to a single isotropic, homogeneous material 1D PXCM building block. When $Q=A/t$ is sufficiently high, the building block can remain at BP_2 under stress-free condition. Under high temperatures, the building block performs like a sinusoidal beam missing two parts which is metastable. Therefore, it can transform from BP_2 to MP_1 via temperature control (Figure 2.18 a & d). All these designs were evaluated and shown to be feasible alternatives using FE simulations, the details of which can be found in the Appendix A.

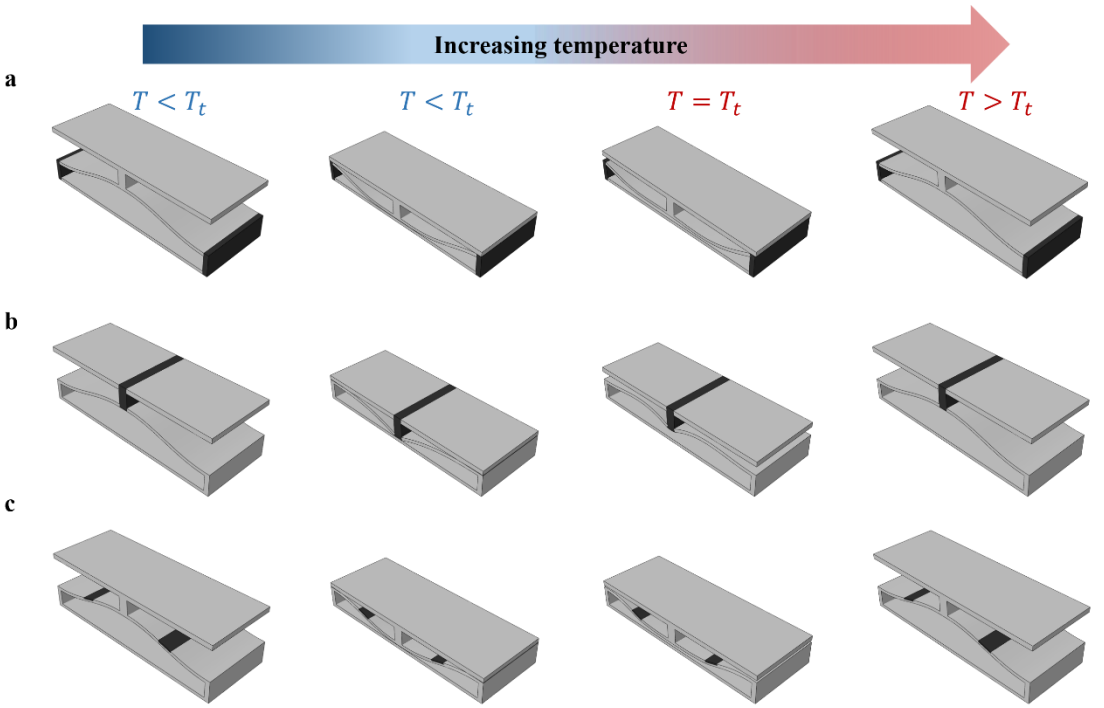

Figure 2.17: PXCMs family. (a)-(c) Demonstrate the building blocks of *Type I*, *II*, and *III* PXCM having temperature-induced phase transformation.

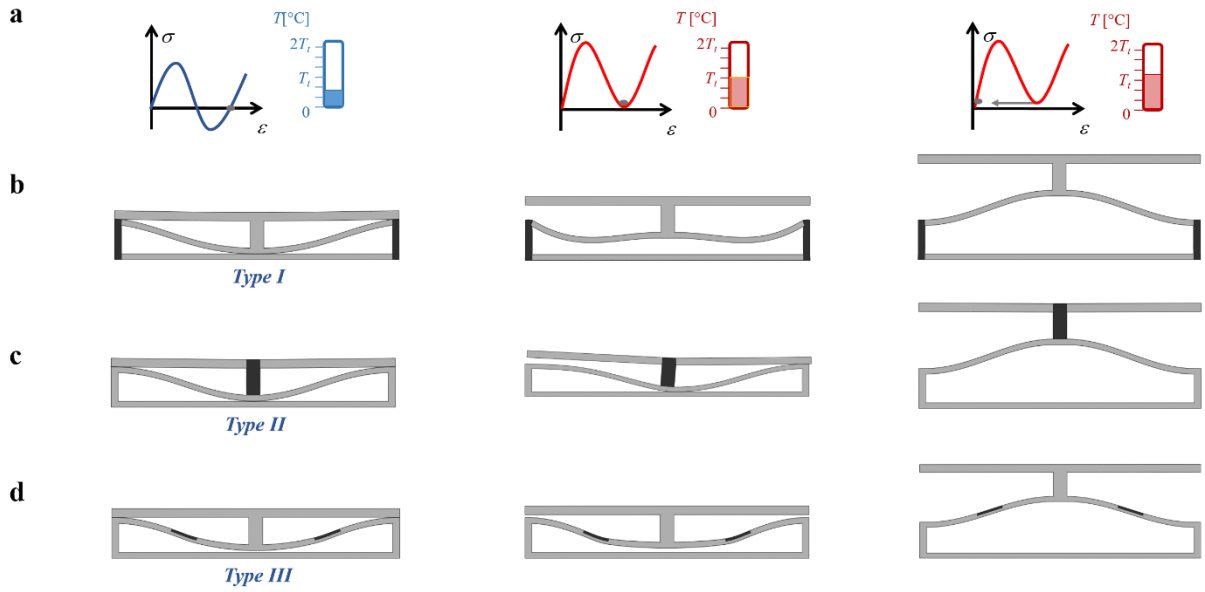

Figure 2.18: (a) Schematically plot σ-ε relation of PXCMs varies with temperature. (b)-(d) FE simulations of three designs transform from BP_2 to MP_1 via increasing temperature.

2.5 Conclusions

A family of smart programmable phase transforming cellular materials (PXCMs) which can mimic the shape-memory effect and superelasticity of Shape Memory Alloys are created. This work have shown how to design the phase transformation of PXCM by controlling the thermomechanical relationship between the stiff walls and the sinusoidal beam. In addition, it demonstrates how to program PXCMs to produce work via temperature change. PXCMs significantly increased the actuation strain capacity to 200% compared with the strain capacity of SMAs, which usually is less than 10%. The transformation stress and temperature of PXCMs can be tailored to suit various applications using the design guide we provided. Temperature is only one method to tune the stiffness and compliance of a bistable/metastable building block to achieve phase transformation. Other physical stimuli such as magnetic fields, moisture contents, or electrical fields can be used to trigger similar effects.

3. BIOINSPIRED PXCMS SHAPE RECOVERY SYSTEM

The work in this chapter was done in collaboration with Tarah N. Sullivan and Prof. Marc Meyers from University of California San Diego. A version of this chapter has been previously published in Advanced Functional Materials https://doi.org/10.1002/adfm.201801250

3.1 Overview

As necessary appendages to the bird wing for flight, feathers have evolved to address the requirements of aerial locomotion. One of the recently discovered, fascinating aspects of this is their ability to recover shape and strength with hydration. This feature significantly enhances the effectiveness of a bird's flying capability as it allows for the natural restoration of feathers damaged by predators or other external forces.

Imperative for bird flight, feathers are an evolutionary marvel designed to be lightweight yet able to endure the intense loads of flight[40]. Flying feathers of birds consist of a main shaft (rachis and calamus) and a vane that branches from the rachis. The rachis is foam-filled and rectangular (Figure 3.1a) while the calamus is hollow and elliptical, embedded under the skin (Figure 3.1b). Although the vane captures the majority of air in flight, it transfers loading to the shaft, which possesses higher rigidity and strength. Integrity of the shaft is therefore essential to a bird's survival, especially since feathers are usually only replaced once a year[41]. Feathers are composed entirely of β-keratin, a "dead tissue" formed by keratinous cells. This biopolymer can be considered a hierarchical fiber-reinforced composite (Figure 3.1 c,d): at the sub-nanoscale crystalline β-keratin filaments (~3 nm in diameter) are embedded within amorphous matrix proteins. This filament-matrix composite forms macrofibrils (~200 nm in diameter) which are surrounded by amorphous intermacrofibrillar material. Macrofibrils then bundle to form fibers (3-5 μm in diameter) and these in turn form ordered lamellae within the dense exterior of the feather shaft[41–43] The fiber direction within these lamellae varies depending on the side and location along the feather shaft as well as the species of bird[44].

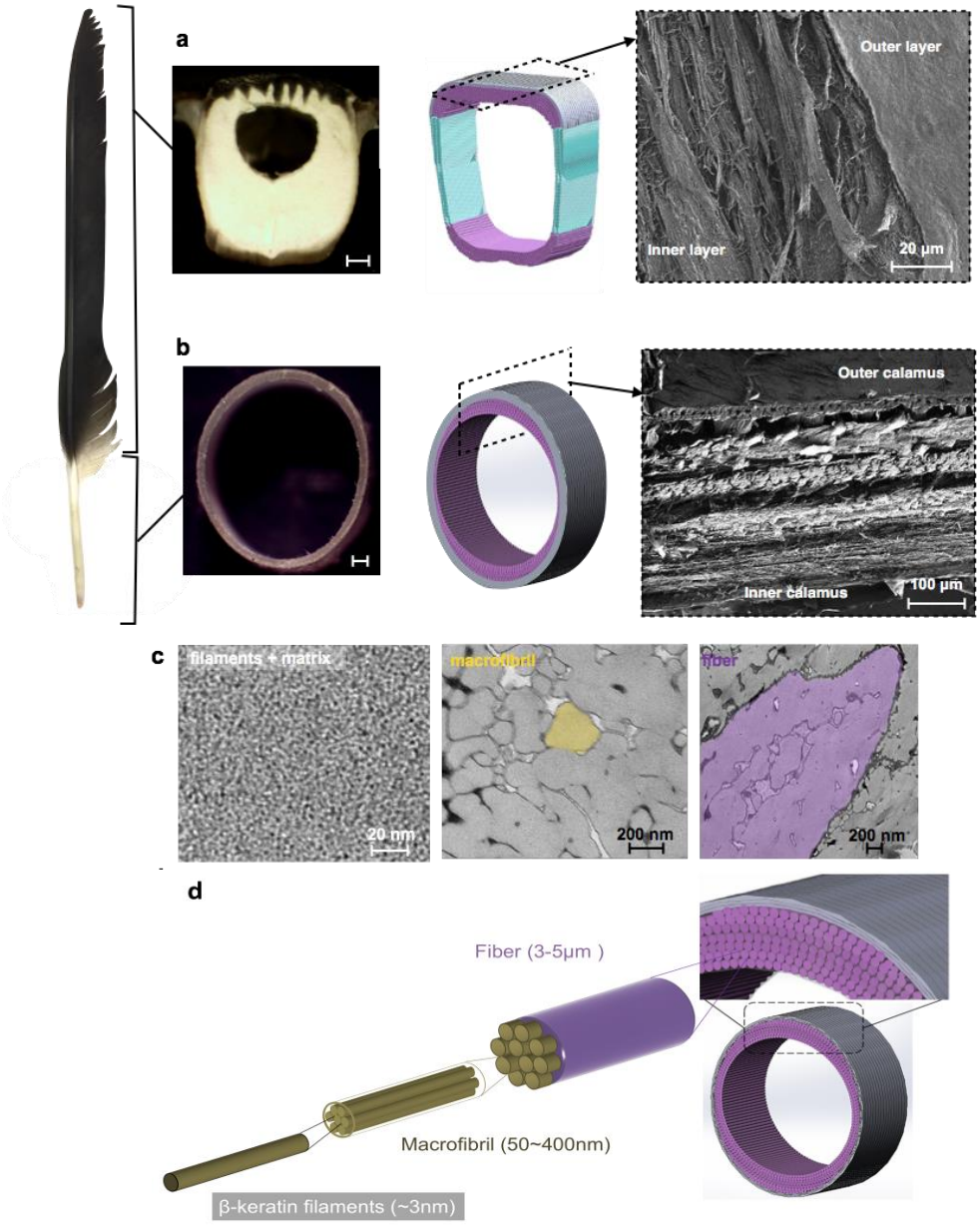

Figure 3.1: The hierarchical structure of the feather. The flight feather of the Cape Vulture (Gyps coprotheres) is divided into the (a) rachis and (b) calamus. Optical microscope images of both sections are shown in the leftmost images (scale bar is 0.5mm). Fiber models of the feather sections illustrate that fibers run longitudinally along the shaft (purple), and circumferentially (gray) within the calamus and dorsal side of the rachis, while fibers alternate at ±45° angles (green) in the lateral walls of the rachis. On the right, SEM images of the dorsal rachis and calamus confirm the orientations of fibers in the corresponding sections of fiber models. (c) TEM images reveal a filament and matrix structure that forms macrofibrils which in turn form fibers, (d) a schematic of this is drawn to clarify this structure.*

* The figure was made by in Tarah N. Sullivan from University of California San Diego

Previous studies on feathers provided the experimental characterization of the fibers and matrix of the feather shaft. It showed that the fibers can remain approximately elastic under the large deformation and the mechanical properties are insensitive to the hydration process. On the contrary, the matrix can develop plastic deformation and during the hydration process, and the cortex shows approximately 20% expansion in cross-section. This part of the study is attending to explain the phenomenon of both shape and strength of the feather shaft cortex recover during the hydration process. Furthermore, a bioinspired PXCMs-spring system is created to mimic the shape recovery behavior of feathers.

3.2 Analytical model to capture the shape recovery effect

The feather cortex is composed of matrix and fibers with different lengths and orientation angles (Figure 3.1). While the architecture of the cortex is complex, the recovery process of cortex can be explained by a simple model based on the previous experimental characterization of the fibers and matrix. Hydration significantly affects the flow stress and Young's Modulus of the matrix only as schematized in Figure 3.2 and induces hydrostatic swelling in the material. For the computational model, the matrix is modeled as an initially elastic-perfectly plastic material and the fibers as linearly elastic. Hydration is added as a hydrostatic strain, ε_{sw}, to the total strain as follows:$\varepsilon = \frac{\sigma}{E} + \varepsilon_{pl} + \varepsilon_{sw}$.

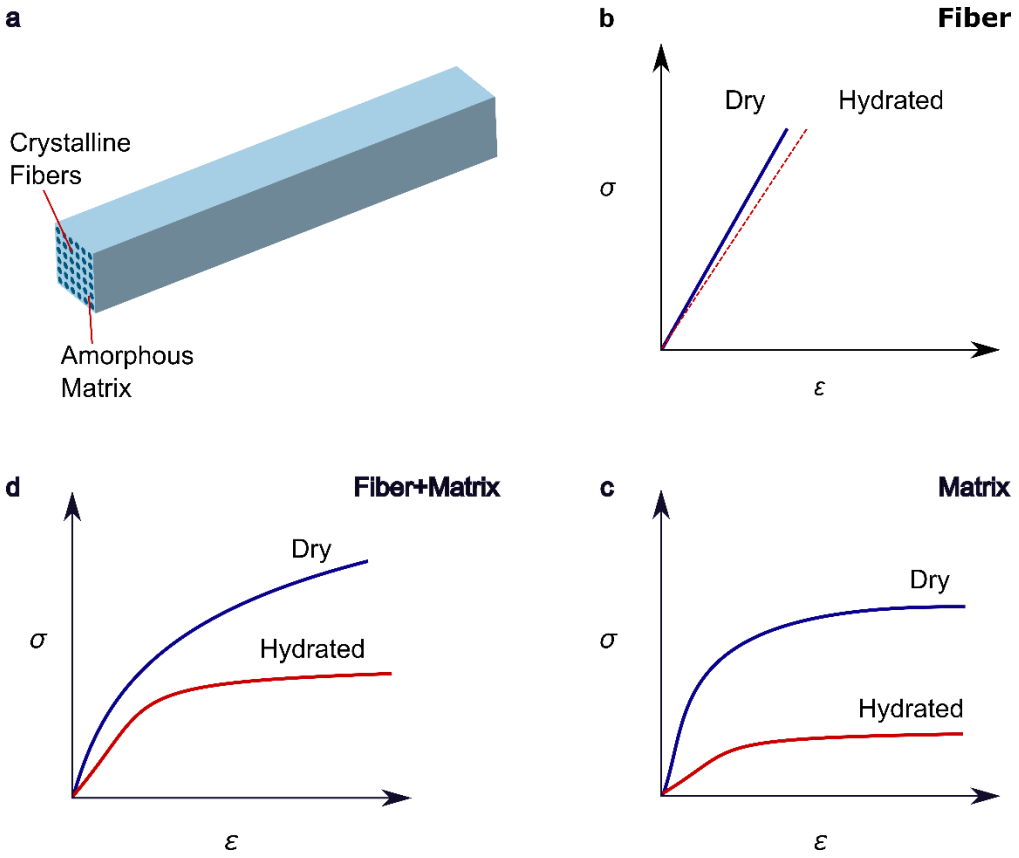

Figure 3.2: Schematic representation of composite (fiber and matrix) response in hydrated and dry conditions. (a) Crystalline fibers in amorphous matrix; (b,c) fiber and matrix responses; fibers are not affected by hydration whereas the matrix softens. (d) Composite response showing a significant difference between dry and hydrated conditions.

3.3 Simulations of shape recovery in the feather

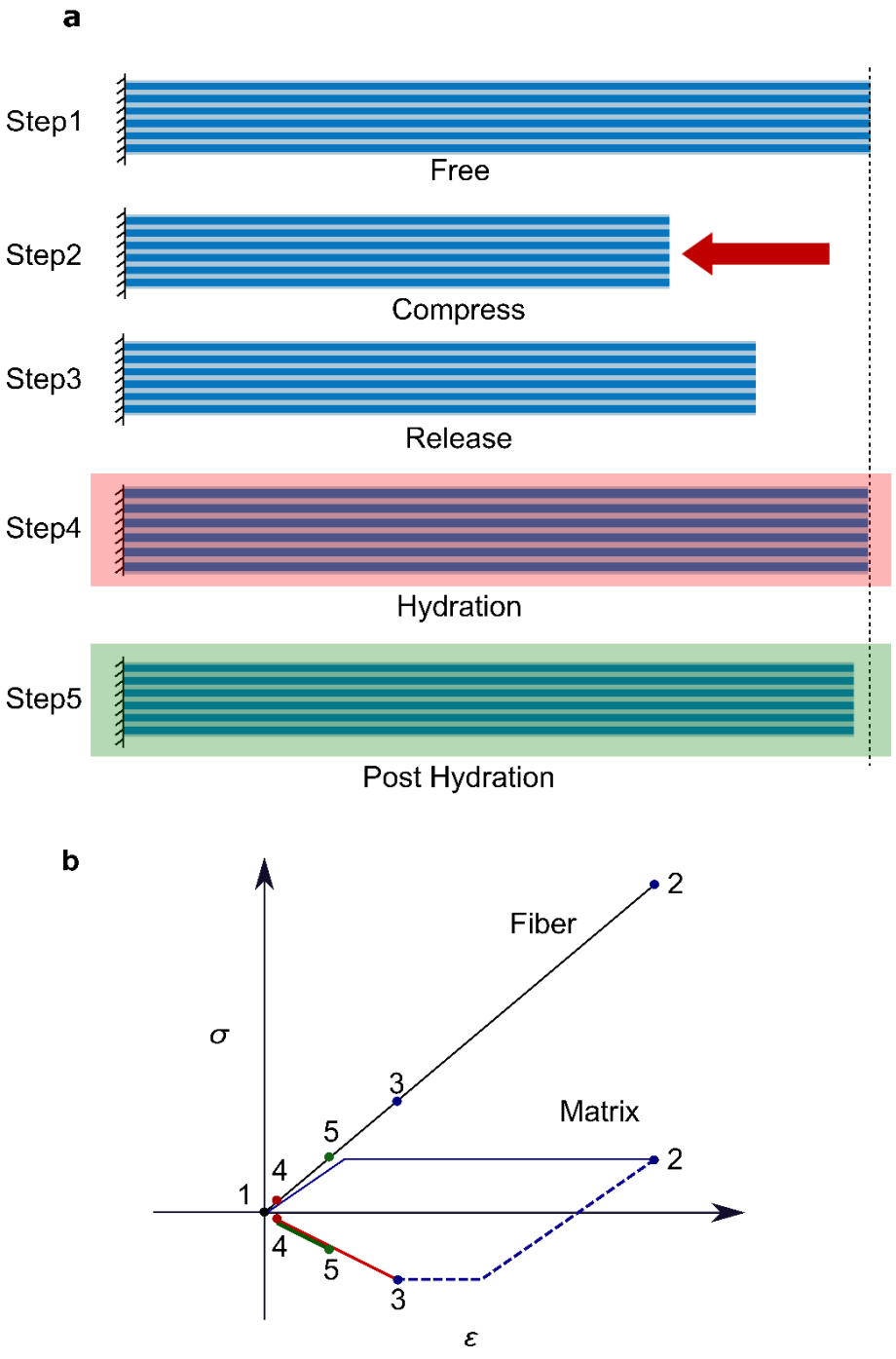

Figure 3.3: Model description: (a) Step 2 and 3 indicate the initial loading and unloading in the dry configuration. Step 4 describes the hydration process where the elastic modulus and flow stress of the matrix drop significantly and swelling occurs, allowing the relaxation of the elastic fibers. Step 5 is the final drying post hydration process, where the matrix shrinks and some minor gain in strain is observed. (b) The stress-strain behavior in the matrix and fiber is plotted. Note that the positive axes denote compression stress and strain.

A simple illustration of this model is shown in Figure 3.3a for a representative volume element of a composite sample under compression. The dark blue and light blue stripes represent fibers and matrix. The matrix and fibers are perfectly bonded together. One end of the sample is constrained in *X* direction. Displacement of the other end of the sample is used to calculate the strain. At Step 1, the composite sample is under the stress and strain-free conditions where,

$$\varepsilon_1 = 0$$

$$\sigma_f = \sigma_m = 0$$

The displacement δ_a is applied to in Step 2 causes matrix undergoing plastic deformation.

$$\varepsilon_2 = \delta_a / l_o = \varepsilon_c + \sigma_{md}^y / E_{md} \quad \text{Eq. 3.1}$$

$$\sigma_m^2 = \sigma_{md}^y \quad \text{Eq. 3.2}$$

$$\sigma_f^2 = \sigma_{md}^y A_m / A_f \quad \text{Eq. 3.3}$$

The load is released in Step 3, inducing permanent deformation and residual stress (e.g., fibers are in compression and the matrix is in tension under equilibrium and free of external loads). To simplify the expression, the parameter ε_c is defined as below.

$$\varepsilon_c = \delta_a / l_o - \sigma_{md}^y / E_{md} \quad \text{Eq. 3.4}$$

The strain and stress at Step 3 are shown as below.

$$\varepsilon_3 = \frac{A_m E_{md} \varepsilon_c}{E_{md} A_m + E_f A_f} \quad \text{Eq. 3.5}$$

$$\sigma_m^3 = -\frac{A_f E_f E_{md} \varepsilon_c}{E_{md} A_m + E_f A_f} \quad \text{Eq. 3.6}$$

$$\sigma_f^3 = \frac{E_f A_m E_{md} \varepsilon_c}{E_{md} A_m + E_f A_f} \quad \text{Eq. 3.7}$$

It should be noted that the plastic deformation only takes place in the matrix while the fibers remain elastic and in compression.$\sigma_m^3 = -\sigma_{md}^y$

$$\varepsilon_3 = \frac{A_m \sigma_{md}^y}{A_f E_f} \quad \text{Eq. 3.8}$$

$$\sigma_f^3 = \frac{A_m \sigma_{md}^y}{A_f} \quad \text{Eq. 3.9}$$

Figure 3.3b shows the stress vs. strain behavior for the matrix and fiber (for convenience, the compressive stress and strain are plotted as positive along the ordinate and abscissa, respectively). The sample is then hydrated to 100% during Step 4. At this point the both, flow stress and Young' Modulus of the matrix drop significantly allowing the fibers that are in compression to stretch and reduce their stress. The matrix also undergoes hydrostatic swelling which helps straighten out the fibers if bending and buckling occurs. As a result, the stress values in the fibers and matrix significantly decrease to values very close to zero (as schematized in Figure 3.2). This process removes some of the permanent plastic deformation induced by the initial load (Step 2). This means that the elastic energy stored in the fibers is sufficient to induce reverse plastic deformation in the matrix. The strain and stress are shown as below.

$$\varepsilon_c' = \varepsilon_c - \varepsilon_{sw} \quad \text{Eq. 3.10}$$

$$\varepsilon_4 = \frac{E_{mh}A_m\varepsilon_c'}{E_{mh}A_m+E_fA_f} \quad \text{Eq. 3.11}$$

$$\sigma_m^4 = -\frac{E_fE_{mh}A_f\varepsilon_c'}{E_{mh}A_m+E_fA_f} \quad \text{Eq. 3.12}$$

$$\sigma_f^4 = \frac{E_fE_{mh}A_m\varepsilon_c'}{E_{mh}A_m+E_fA_f} \quad \text{Eq. 3.13}$$

Finally, the sample is dehydrated back to 0% at Step 5, and the material recovers its original Young's Modulus and Yield stress. While the swelling strain goes back to zero (i.e., ε_{sw} =0), the permanent deformation due to the initial loading step gets significantly reduced during the hydration step. Dehydration leads to a very small amount of loss in the recovery strain, but significantly small than the actual recovery strain gained in the hydration step. The strain and stress are presented as below.

$$\varepsilon_5 = \frac{\varepsilon_c'E_{md}A_m}{E_{md}A_m + E_fA_f} \quad \text{Eq. 3.14}$$

$$\sigma_f^5 = \frac{\varepsilon_c'E_{md}A_mE_f}{E_{md}A_m+E_fA_f} \quad \text{Eq. 3.15}$$

$$\sigma_m^5 = -\frac{\varepsilon_c'E_{md}A_fE_f}{E_{md}A_m+E_fA_f} \quad \text{Eq. 3.16}$$

Figure 3.3b shows the rest of the steps in terms of the stress-strain behavior in the matrix and fiber. As it can be observed, the hydration process in Step 4 almost fully

recovered the stress in both fiber and matrix. The hydration process reduces the elastic modulus and flow stress of the matrix enabling the fibers to stretch and further lower their compressive stress. Furthermore, swelling in matrix creates a hydrostatic stress that push the fibers to recover their original length. It surmises that, if buckling is present, this swelling and push mechanisms allow further strain recovery by straightening out the fibers. The post hydration process in Step 5 is illustrated by a minor increase in strain and stress in Figure 3.3b. Here, the recovery ratio rate r at the end of Step 5 is defined to quantify the level of the recovery. Smaller ε_c', large the recovery rate.

$$r = 1 - \frac{\varepsilon_c'}{\varepsilon_c} = 1 - \frac{\frac{\sigma_{mh}^y}{E_{mh}} + \left(\frac{A_m \sigma_{mh}^y}{E_f A_f} + \varepsilon_{sw}\right)}{\delta_a / l_o - \sigma_{md}^y / E_{md}} \qquad \text{Eq. 3.17}$$

3.4 FE simulations

To verify the hypothesis that the geometry and strength of the feather cortex recovers with hydration, a finite element analysis (FEA) model was developed based on the individual responses of the matrix and fibers. A representative volume element consisting of six fibers embedded in a matrix composite beam (Figure 3.4a) is created to represent a section of the feather shaft cortex. The FEA model considers a plane strain condition, and mechanical properties of the fiber and matrix were obtained from hydrated and dehydrated feather cortex properties. The fibers were assumed to be unaffected by water content and considered to behave linearly elastically, while the matrix was assumed to be an elastic-perfect plastic material. With an increase in water content, the elastic modulus and yield stress of the matrix decreases and the matrix swells. Firstly, a prescribed curvature, κ_{ap}, was applied to the composite by imparting an external bending moment at the ends of the composite. This causes the matrix to plastically deform leading to a permanent curvature, κ_{pl}, shown in Figure 3.4b. While the composite is plastically deformed, 100% water content was gradually applied to the composite through a hydrostatic strain (Figure 3.4c). Concomitant with the hydration, the flow stress of the matrix is decreased. The stress in both the fibers and matrix, and therefore the elastic energy stored in the fibers, significantly drop, leading to a much lower curvature, κh, of the composite. After complete hydration, a post hydration process was applied to the composite to decrease the water content from 100% to 0% (Figure 3.4d). This dehydration process leads to a curvature, κ_d, slightly larger than the hydrated curvature. The shape recovery for

the hydration, r_h, and post hydration step, r_d, can be defined by $r_i = \left|\frac{\kappa_i - \kappa_{pl}}{\kappa_{pl}}\right| \times 100\%$, where $\kappa_i = \kappa_h$ is the curvature of composite beam under 100% hydration, and $\kappa_i = \kappa_d$ is the curvature of composite post hydration. Figure 3.4e shows the shape recovery attained with hydration (r_h), and post hydration (r_d) as a function of the applied curvature, κ_{ap}. While the hydrated sample recovers to a greater extent (99.5%) than the post hydrated sample

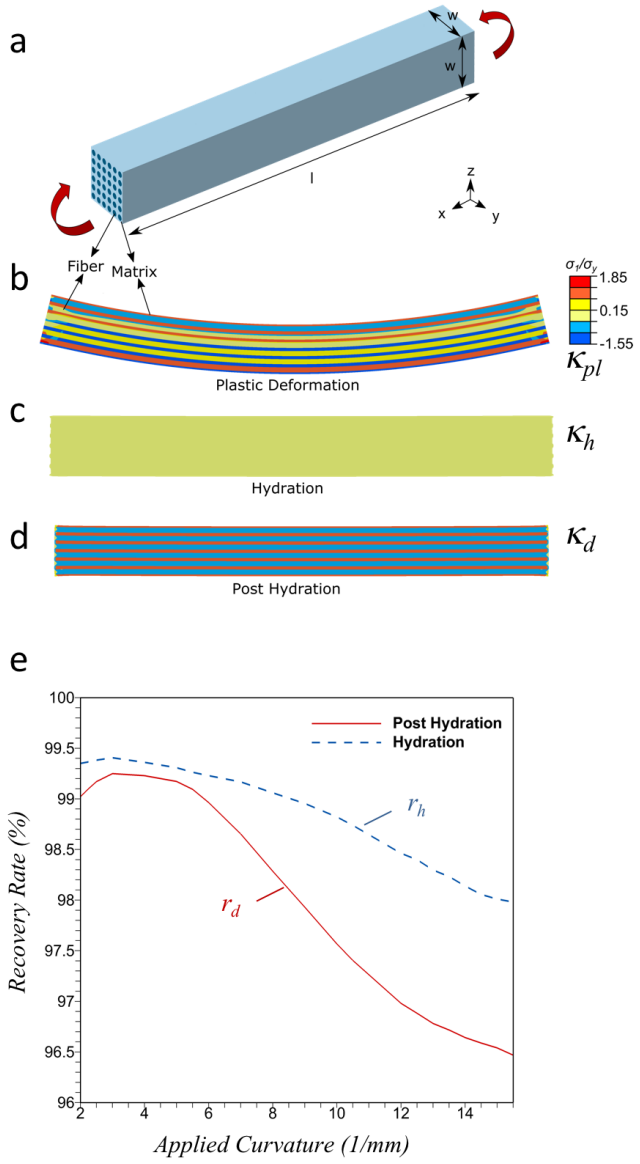

Figure 3.4: FE simulations of the shape recovery process. (a) Schematic of the representative volume element where an applied curvature is prescribed along the composite to induce plastic deformation in the matrix. (b) The deformed composite with residual stress after unloading. (c) After hydration, the residual stress drops significantly, and the section regains its shape. (d) The composite retains much of the shape recovery at post hydration. (e) The recovery rate after hydration and post hydration as a function of the applied curvature yields high values of recovery.

3.5 Bioinspired PXCMs-spring system

Inspired by the shape recovery effects of feathers, a new PXCM-spring system was developed. As introduced in Chapters 2 through 4, a PXCM building block is either bistable or metastable. A building block has two phases – phase 1 and phase 2 – which correspond to two stable geometric configurations. When a PXCM sample, which comprises a number of building blocks, undergoes displacement-controlled cyclic loading it exhibits the Force-displacement (*F-d*) relationship shown in Figure 3.5. The *F-d* relationship is linear until the force reaches a maximum force F_{max}, the first row of unit cells transforms to the second stable configuration. Due to material imperfections, each row of cells collapses progressively, resulting in a serrated *F-d* curve. Each serration represents a row of PXCM building blocks undergoing a phase transformation. Here, the average plateau forces F_{pl}^{l} and F_{pl}^{u} describe the loading and unloading paths. With relatively smooth plateau force – that is, when the amplitude of the serrations is much smaller than F_{pl}^{l} – the $\sigma - \varepsilon$ relationship of a PXCM sample can be approximated as elastic-perfectly plastic. This relationship is similar to the matrix of a feather cortex. Increasing the temperature of the PXCM sample, F_{pl}^{l} decreases and F_{pl}^{u} increases as shown in Figure 3.5b. Using the concept of hydration-induced shape recovery effect on feathers, a system consisting of 1D PXCMs and elastic springs can be designed to exhibit shape recovery effect via temperature changes.

This system was modeled using PXCMs with materials whose elastic moduli decrease when temperature increases, and springs with stiffnesses that are insensitive to temperature changes. The PXCMs act as the matrix in a feather cortex, and the springs act as the fibers. In contrast to shape recover of feathers which is induced by hydration, the shape recovery effect in this PXCM-spring system is triggered by increasing temperature.

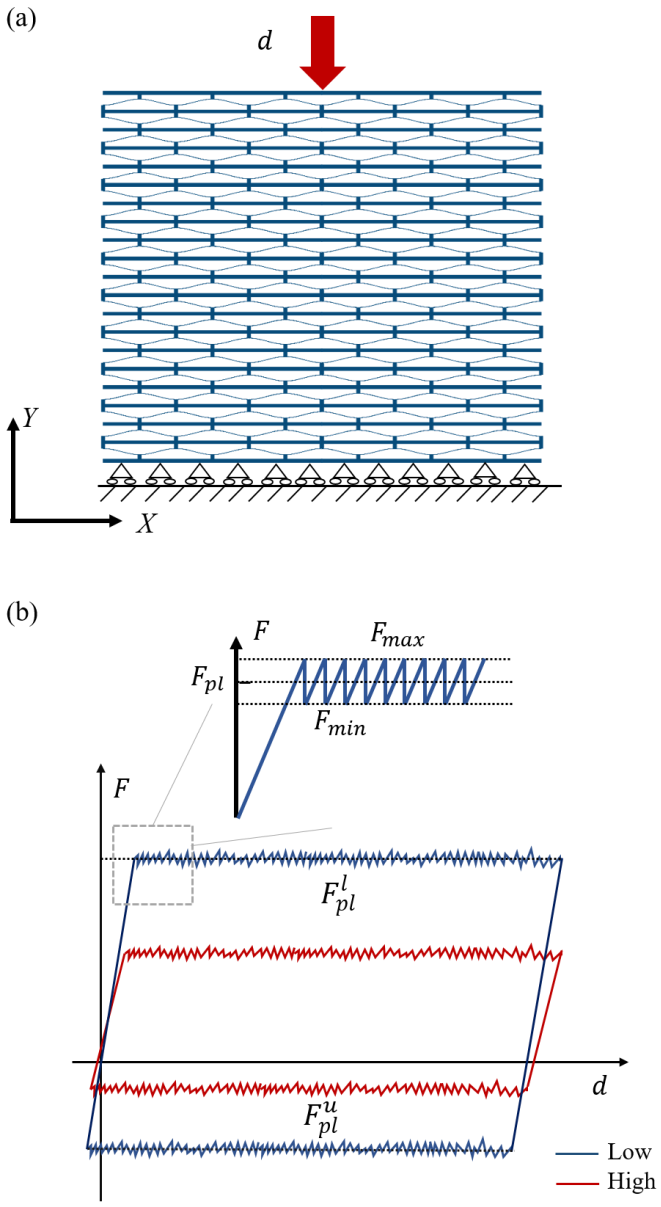

Figure 3.5: (a) A 1D PXCMs sample. (b) Schematically mechanical response of the 1D PXCMs sample.

The system is modeled consists of 20 PXCM building blocks connected in series and 3 PXCM building blocks connected in parallel. The geometric details of a unit cell are presented in Table 3.1 and Figure 3.6. Material properties for the PXCMs are based on Shore 95 material which has an elastic modulus that reduces with temperature as shown in Figure 3.7. The PXCMs are connected to *n* elastic springs (here *n*=2) with stiffness k_{sp} which does not vary with temperature.

Implicit dynamic finite element (FE) analyses were conducted in Abaqus 6.18. These FE simulations used a two-node, shear flexible beam element discretization of the PXCM samples.

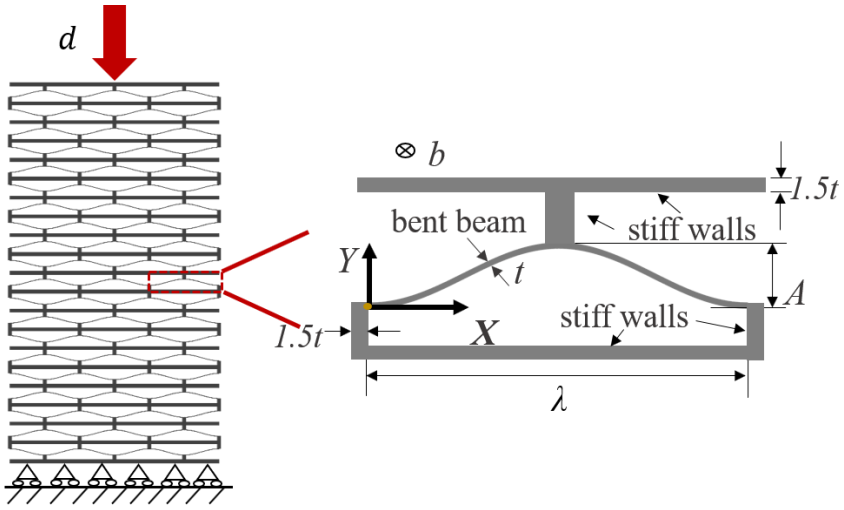

Figure 3.6: Geometry of the PXCM sample and the building block.

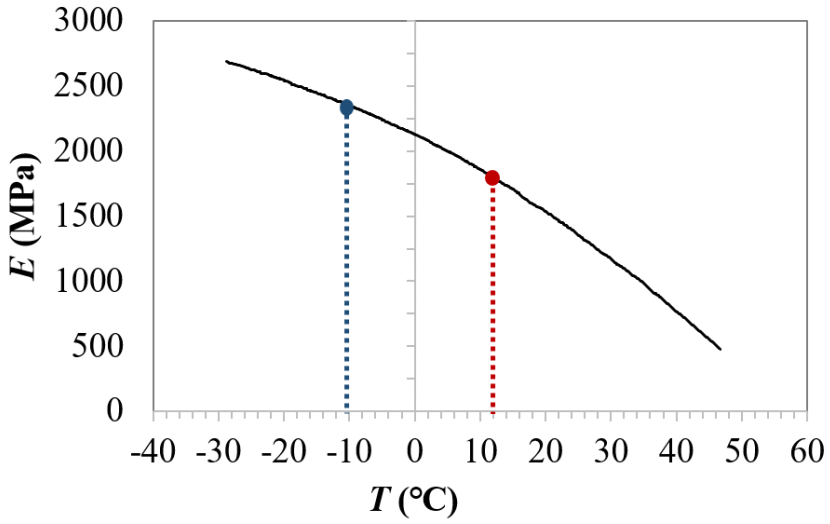

Figure 3.7: Elastic modulus of shore 95 varies with temperature.

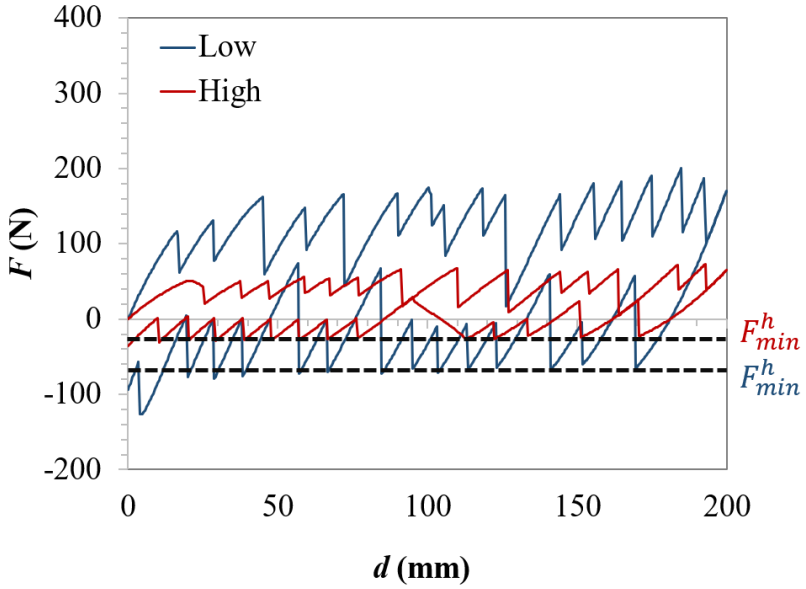

Figure 3.8: *F-d* relationship of the PXCMs sample at the low temperature *T*=-10℃ and the low temperature *T*=-10℃

Table 3.1: Geometric parameters of a PXCM building block in the system studied.

Parameter	Dimension, mm.
t	1.25
A	5
λ	60
b	25

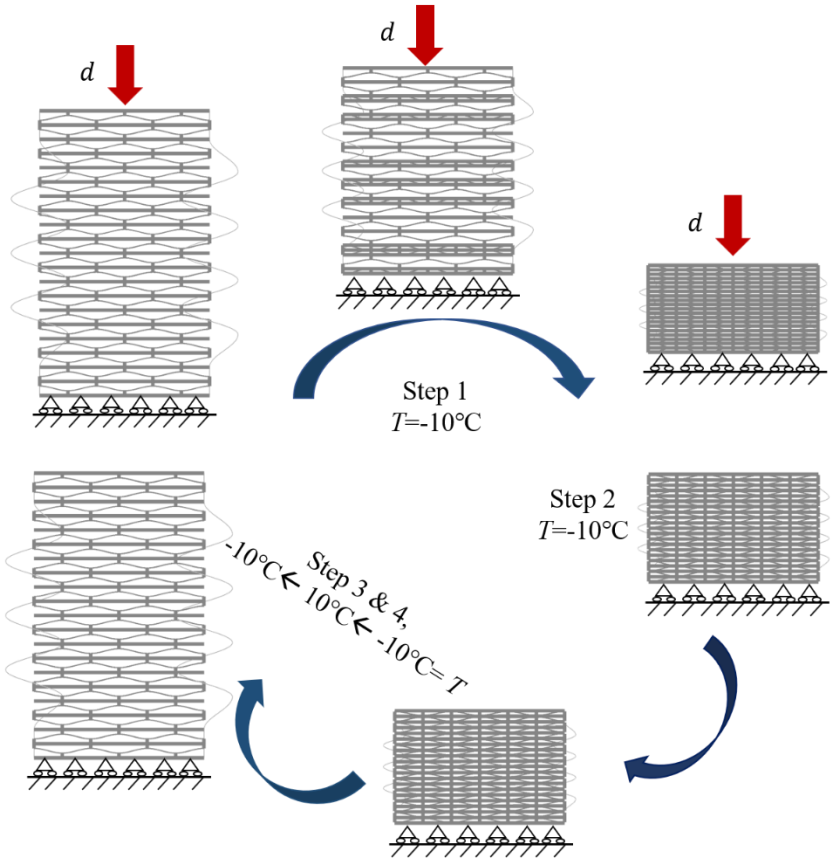

Figure 3.9: The FE simulation shows the PXCMs-spring system exhibits shape recovery effects by tuning temperature.

The recovery process of the PXCM-spring system is shown in Figure 3.9. In Step 1, at low temperatures (T=-10 ℃), a displacement was applied to the system at a rate of 1mm/sec. for 200 seconds. This load caused all unit cells to transform from phase 1 to phase 2. Both the springs and the PXCMs were under compression in this step.

In Step 2, the load was removed, and the system was kept at the same temperature for 100 seconds. After the external force was released, the system began to seek a new equilibrium with the spring in compression and the PXCMs in tension. The system can reach a new equilibrium position with PXCMs in phase 2 if F_{min} along the unloading path of the F-d curve (Figure 3.8) at the low temperature provides sufficient tension to balance the compression in the spring. In other words, the system can reach a new equilibrium position with PXCMs in phase 2 if the following equation is satisfied:

$$nk_{sp}d_2 \leq F_{min}^{l} \quad \text{Eq. 3.18}$$

In Step 3, the temperature was increased to a higher value of T=10 ℃, which led both the magnitude of the unloading plateau force F_{pl}^{u} and the corresponding minimum force F_{min}^{h} to decrease as shown in Figure 3.8. Recovery is triggered once the F_{min}^{l} is lower than the compressive force in the spring (Eq. 3.19).

$$nk_{sp}d_3 = F_{min}^{h} \quad \text{Eq. 3.19}$$

Here, the stiffness of the spring is set to k_{sp} =0.055 N/mm to ensure that during Step 2 shape recovery can take place around T=10 ℃.

Finally, in Step 3, the temperature is decreased to the original temperature T=-10 ℃. The recovery rate r is measured as follows:

$$r = \left(1 - \frac{d_4}{l_o}\right) \times \% \quad \text{Eq. 3.20}$$

The *F-d* relationship at each step is shown in Figure 3.10(a) and the values at the end of each step are summarized in Table 3.2. The PXCMs exhibited superelasticity which allowed them to show pseudo elastic-plastic behavior without permanent deformations. Therefore, unlike the matrix in feathers that can never recover completely due to plastic deformations, PXCMs can recover completely.

The time, displacement, and reaction force from these analyses are summarized in Table 3.2 and Figure 3.10 (b). As shown in Table 3.2 there is no residual displacement. Therefore, this new PXCMs-spring system can achieve shape recovery effects via tuning temperature.

The preliminary results show the feasibility to create this new PXCMs-spring system to achieve shape recovery. In the future, the system will be fabricated via additive manufacturing and tested via experiments.

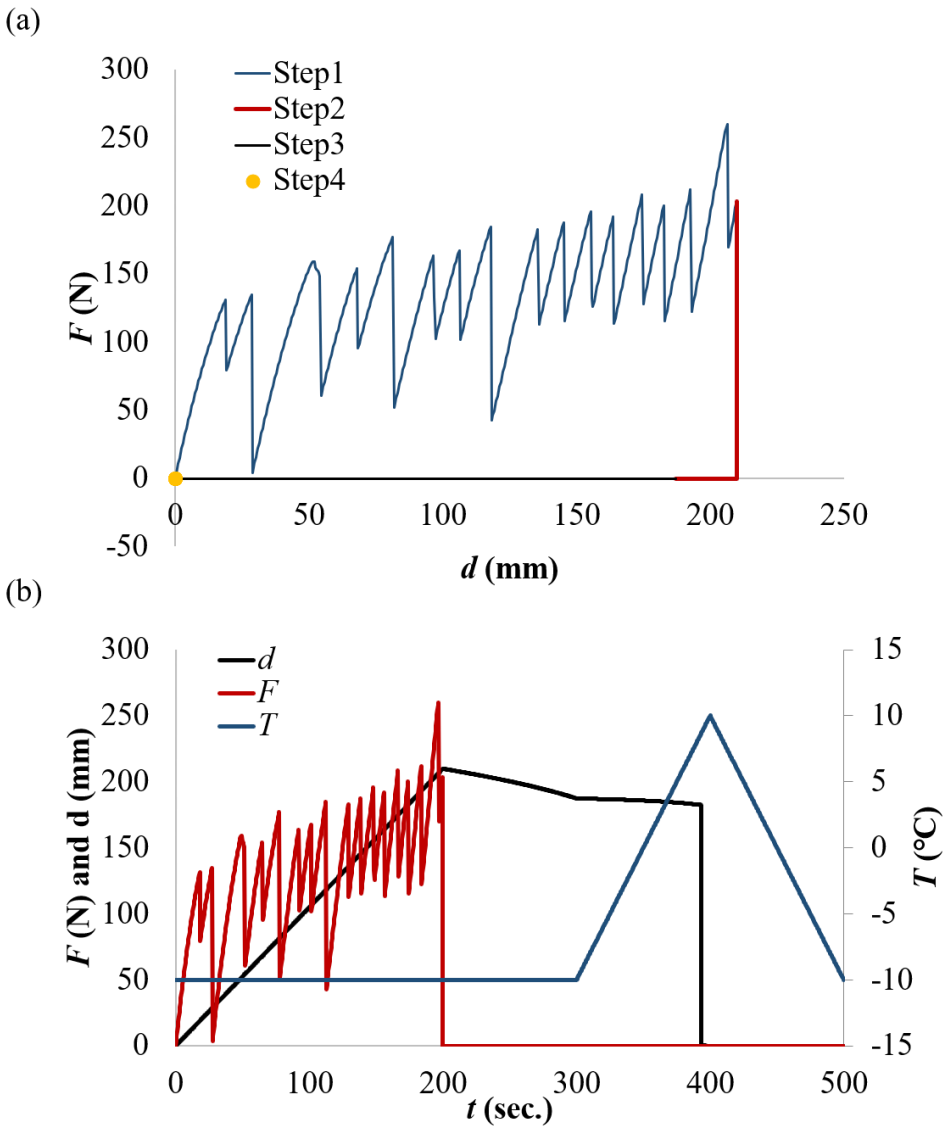

Figure 3.10: FE simulation results. (a) *F-d* relationship of the system at each step. (b) Displacement, force, and temperature vary with time.

Table 3.2: Force and displacement of the system at end of each step.

Step	Time, *t* (sec.)	Displacement, *d* (mm)	Force, *F* (N)
1	210	209.90	203.16
2	187	187.36	0
3	0	-0.04	0
4	0	0.00	0

4. RESPONSE OF A SDOF PXCM SYSTEM UNDER DYNAMIC LOADING CONDITIONS

The work in this chapter was done in collaboration with Prateek Shah and William Pollalis, and Prof. Santiago Pujol from Purdue University and Nilesh Mankame from General Motors.

4.1 Overview

Buildings exposed to earthquakes are designed for life safety. They exhibit nonlinear behavior and plastic deformation in structural components in the form of yielding of steel and cracking or crushing of concrete. This nonlinear deformation results in damage, even in buildings which perform as expected. And although buildings that survive earthquakes may be safe to use, they may still be demolished because repairs are too expensive or because of public perception of damage. Buildings that can undergo nonlinear deformation without damage would be ideal, because there would be no need to repair or demolish them after a major event. Existing materials are not capable of this behavior, but a new class of materials called phase transforming cellular materials (PXCMs) are capable of it. PXCMs can undergo large deformations without permanent damage, making them an ideal candidate for installation in buildings. Here, results are presented from a series of dynamic tests on an earthquake simulator of a single degree of freedom (SDOF) PXCMs system, and from accompanying FE simulation.

4.2 Design PXCMs

Phase transforming cellular materials (PXCMs) are periodic architected materials with bistable or metastable building blocks. In particular, a metastable building block exhibits one stable and one metastable configuration. The transitions between these configurations are defined as phase transformations[19,45,46]. If designed correctly, a metastable building block can transform between phases and return to the original stable configuration after unloading. The limited forces (plateau force/stress), accurate estimation of force-displacement (*F-d)* relation, and revisable large deformation of PXCMs make them suitable for seismic building design.

PXCMs consist of numerous metastable motifs connected in series and parallel. Each motif comprises two metastable elementary building blocks and each building block is composed of one sinusoidal beam and stiff walls as supports (Figure 4.1 a-c). The mechanical response for an elementary building block is shown schematically in Figure 4.1d. The *F-d* relationship (solid blue line) has two positive stiffness regimes (R1 and R3) that are separated by a negative stiffness regime (R2). The total internal energy *U* (red dashed line) has one stable and one metastable position. Tabel 4.1e schematically shows a stress-strain ($\sigma - \varepsilon$) relation of a PXCMs sample under a displacement controlled loading-unloading cycle. When there is sufficient number of building blocks connected in series, the snap-through instability can be observed as shown in grey dash line. Under displacement control, no reversal displacement can occur. Once a row of building blocks reach a limit stress point (σ_{max} or σ_{min}), it will snap to the other stable/metastable configuration via the solid vertical blue or red lines. Smaller the stiffness in R2 leads the instability path less stiff, therefore smoother the loading and unloading path PXCMs can exhibit.

The sinusoidal beam of a building block is shaped as the first buckling mode of a straight prismatic beam under axial loading, which is represented by $Y = (A/2)[1 - cos(2\pi X/\lambda)]$, where *A* is the amplitude and λ is the wavelength (Figure 4.1c). A dimensionless parameter $Q=A/t$ is defined as the mechanism of the PXCM building block which can be used to design the building blocks such that they are metastable. The *F-d* relation of a mechanism undergoes phase transformation is shown as equation below

$$F = \left(\frac{dbE\pi^4 t^3}{24\lambda^3}\right)[6Q^2 + 4 + 3Q^2\left(\frac{d}{A}\right)^2 - 9\left(\frac{d}{A}\right)Q^2] \qquad \text{Eq. 4.1}$$

The analytical equation indicates that a PXCM building block is metastable when $Q<2.31$. But the equation is derived under the assumption that each building block is under the clamped-clamped boundary condition. In the interval $Q\epsilon$ [2.3,2.41], the behavior of the mechanism is sensitive to the boundary conditions and small variations in the geometry parameters, therefore cannot be characterized in a robust manner. To ensure that the PXCMs exhibit metastable behavior, remain elastic, and plateau force is smooth, an iterative design process that requires computational

simulations, fabrication, and experiments of PXCMs under a uniaxial loading-unloading cycle was required.

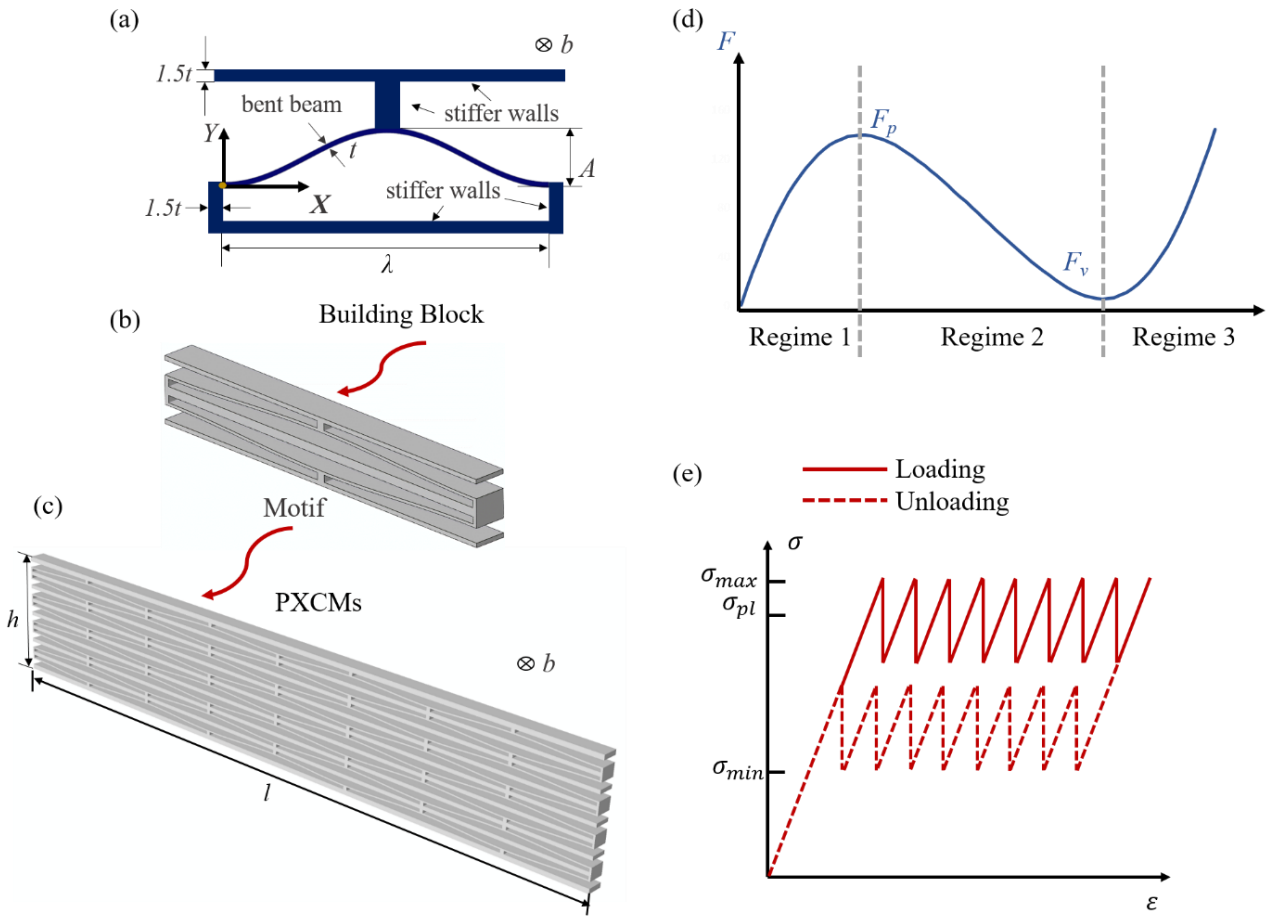

Figure 4.1: The hierarchy structure and mechanical response of PXCMs. (a) A PXCMs building block with corresponding geometric parameters. (b) A PXCMs motif. (c) A PXCMs sample. (d) Schematically mechanical response for an elementary building block. (e) Schematically mechanical response for a PXCMs sample.

4.3 Design and Fabrication

The PXCMs sample was made of aluminum Alloy 6061 and was machined on an OMAX 2652 waterjet with a Tilt-a-Jet cutting head using a garnet abrasive (no. 80) operating at 55k psi. The geometries parameters of the sample (Table 4.1) were chosen to ensure that each building block is metastable and PXCMs can remain elastic under the large deformation. The out-of-plane width of

the sample was chosen to be sufficiently high (b=1 in.) to prevent the sample to buckle out of the plane.

Before conducting dynamic tests on the SDOF PXCMs system, the PXCM sample was tested in cyclic uniaxial compression in a universal test machine (MTS Insight 10). The sample was subjected to three compressive loading-unloading cycles to check for repeatability and any evidence of irreversible deformation. The integral area enclosed by the loading and unloading branches of the *F-d* response corresponds to the energy dissipated by the sample in that cycle (Figure 4.2). The ignorable variation of *F-d* relation of the sample among different cycles indicates PXCMs remain elastic during the phase transformation.

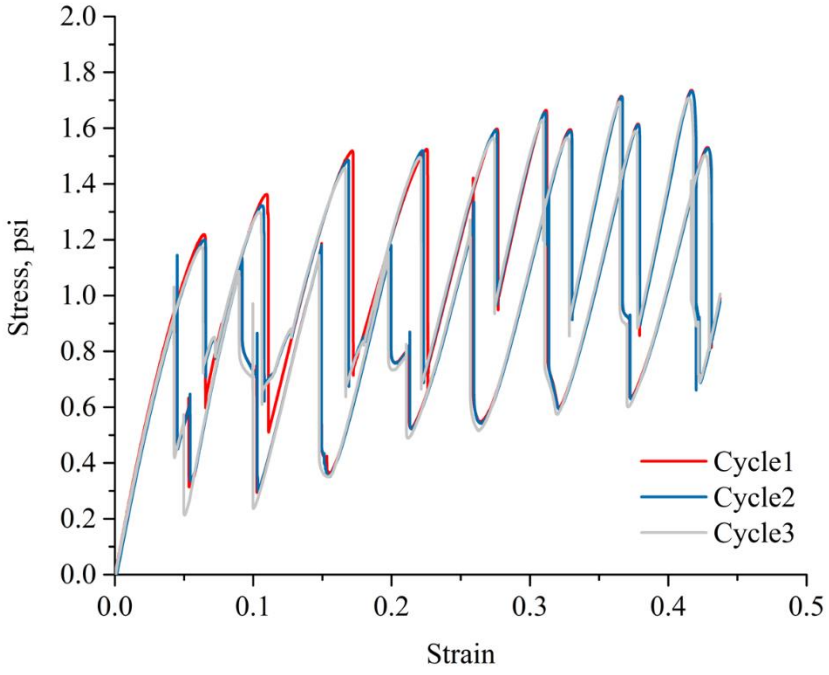

Figure 4.2: Cyclic loading test results indicate PXCMs undergo the reversible deformation.

4.4 FE simulations setup

FE simulations were created to study the response of SDOF PXCM system under several ground motions (Table 4.2 & Figure 4.3). Implicit dynamic finite element analyses in a finite element analysis software Abaqus 6.15 was used to simulate the complex behavior of the system. The FE simulations in this work used a two-node, shear flexible beam element discretization of the PXCM samples. Results from 2D, 3D solid and beam element discretizations were compared for accuracy of the solution as well as its computational cost. The element sizes were determined through a convergence study.

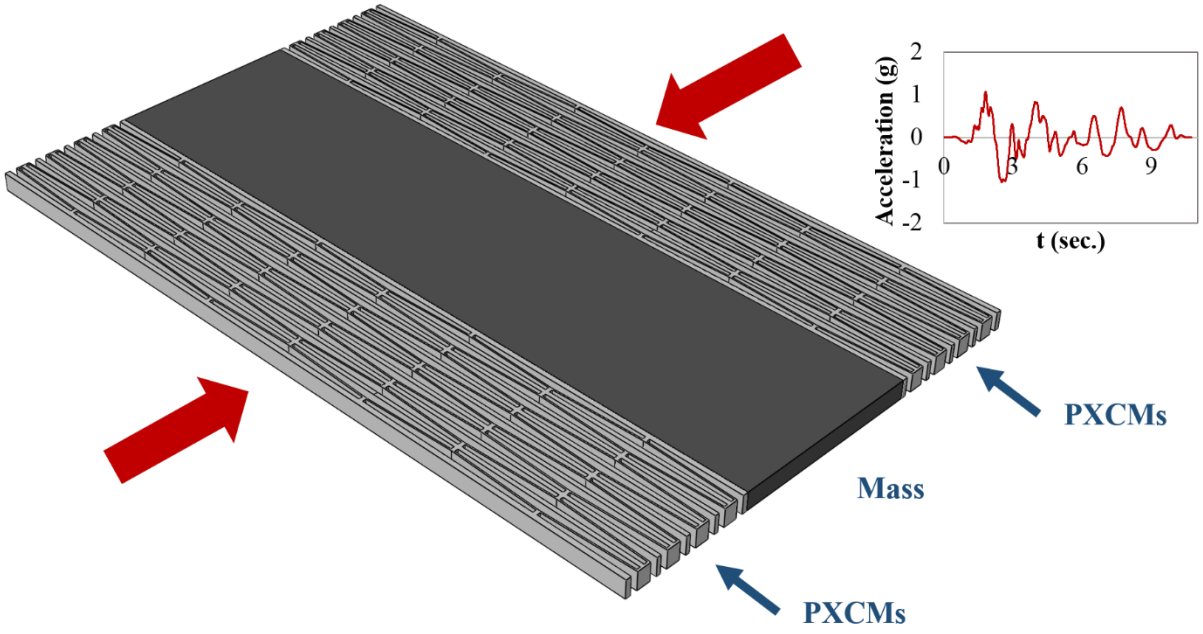

Figure 4.3: FE simulation set up for SDOF PXCMs system.

4.5 Experiments setup

The Single Degree of Freedom (SDOF) PXCMs system was assembled and tested on a unidirectional earthquake simulator*. The aluminum PXCMs sample described from the previous section was split into two samples which and installed to the system. This SDOF system requires two aluminum PXCMs samples, because this aluminum PXCMs sample were designed to resist compressive forces only. The two small samples were placed on either side of a mass and were allowed to separate from the mass to prevent tensile forces in the aluminum PXCMs sample. The aluminum PXCMs sample were attached to the simulator platform using 6"× 6" ×x3/4" steel angles (Figure 4.4). The mass was constructed of a C8×11.5 steel channel. Additional steel plates were attached to the channel to vary its mass. The channel was attached to the simulator platform using four linear motion guide carriages to reduce frictional forces as the mass moved along the surface of the earthquake simulator. The carriages allowed for ±3.5 inches of relative displacement and produced a total of approximately 3 lbf of frictional force as the mass moved, regardless of the amount of mass*. Elevation and plan views of the experimental setup are shown in Figure 4.5 and Figure 4.6.

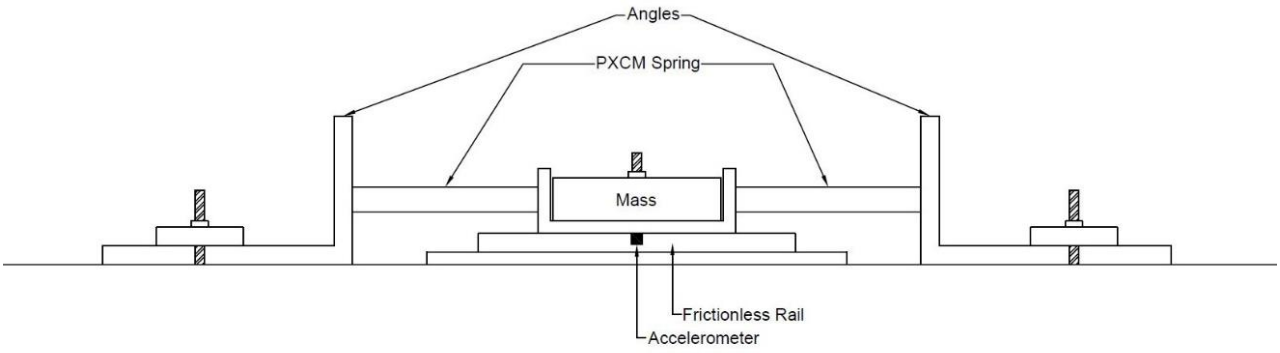

Figure 4.4: Schematic of the experimental setup.

* All the experiments in this section were conducted by William G Pollalis and Prateek P Shah from Santiago Pujol's research group

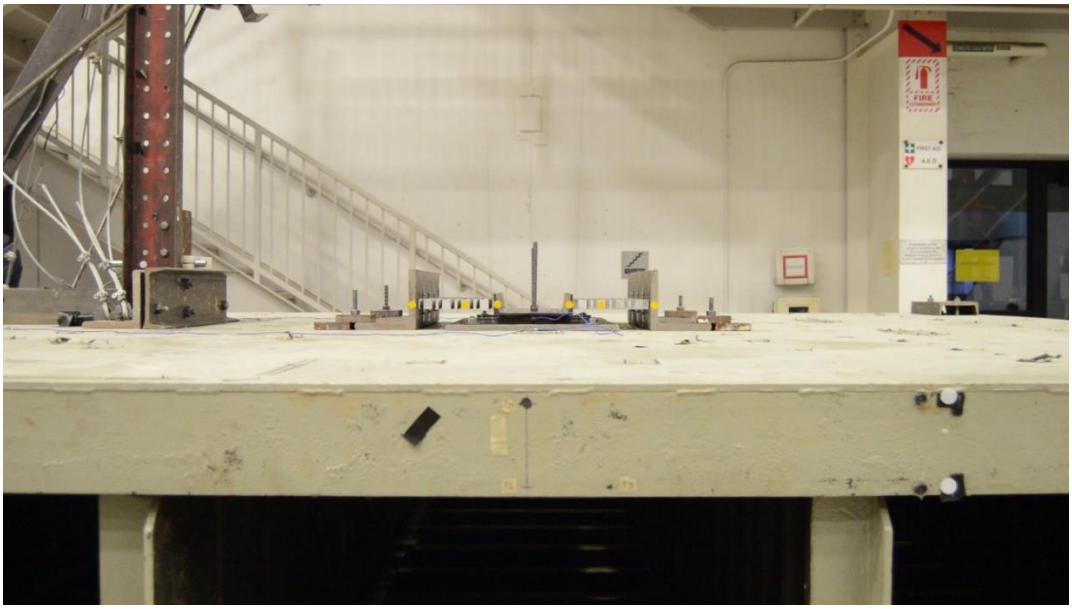

Figure 4.5: Elevation view of the experimental setup*.

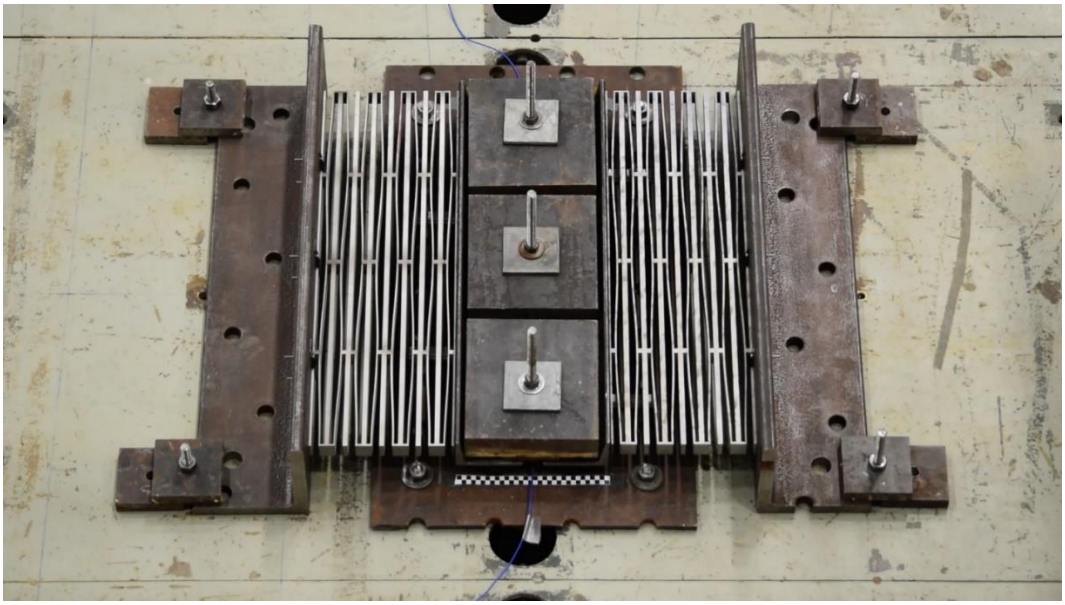

Figure 4.6: Plan view of the experimental setup*.

* All the experiments in this section were conducted by William G Pollalis and Prateek P Shah from Santiago Pujol's research group

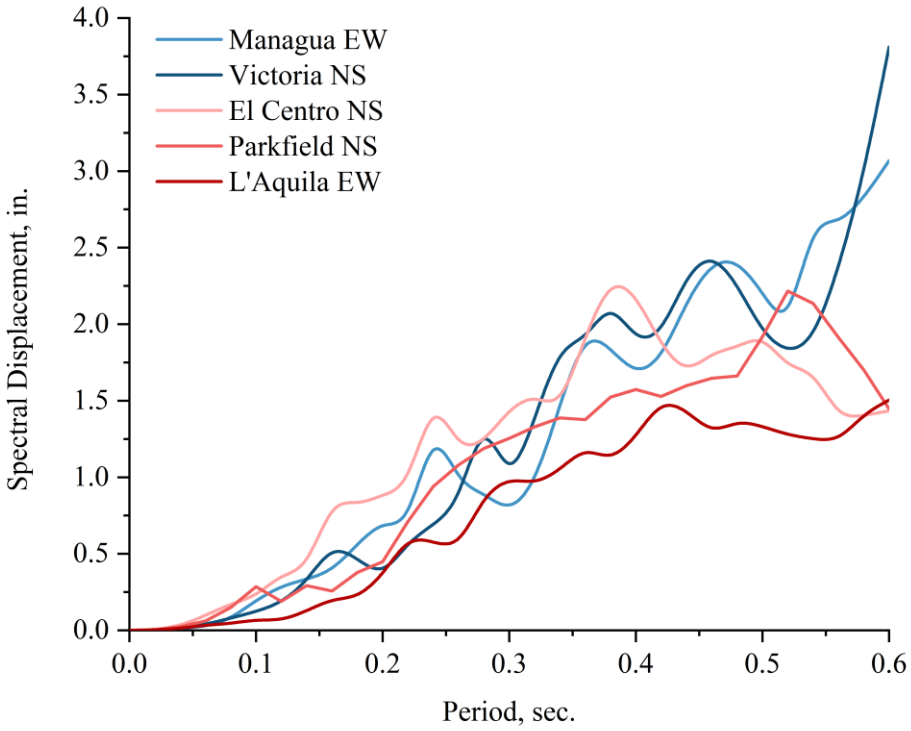

Figure 4.7: Plot of spectral displacement versus period for ground motions used in the experimental program.

Displacement history of the earthquake simulator platform, mass, and angles were measured using OptiTrack, an image-based displacement tracking sensor. A total of 12 optical targets were used. Four targets were attached to the simulator platform, two targets were attached to the flanges of the channel, and two targets were attached on the angles at the same height as the PXCMs samples to measure their slip relative to the simulator platform if any. The remaining four targets were used as reference targets to determine the orientation of the targets. Acceleration history of the earthquake simulator platform and mass were measured using unidirectional accelerometers oriented in the direction of motion of the simulator platform. A total of four accelerometers were used. Two accelerometers were mounted on two diagonally opposite corners of the simulator platform and two accelerometers were attached on the bottom edges of the channel used for the mass[*].

[*] All the experiments in this section were conducted by William G Pollalis and Prateek P Shah from Santiago Pujol's research group

Twelve representative experimental tests with five different ground motion records and five different masses are presented here (Table 4.2). Ground motions were selected such that the SDOF system would be subjected to a wide range of displacement demands for each value of mass. Displacement spectra of the ground motions used are shown in Figure 4.7. Measured values of Peak Displacement for each experimental run are listed in Table 4.2.

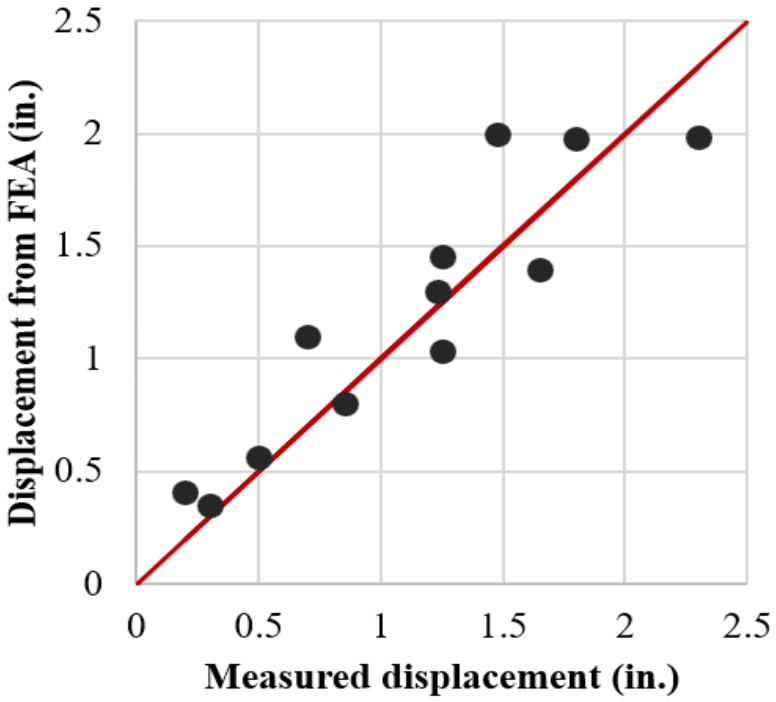

Figure 4.8: FE simulations overall overestimate the maximum relative displacement of the mass from the experiments.

Table 4.1: Geometry parameters of PXCMs building block.

Parameter	Dimension, in.
t	0.08
A	0.2
λ	11
b	1

Table 4.2: Summary of the maximum displacement of each case.

Ground Motion	Scale (%)	Mass (lbf)	Peak Displacement (in)				FEA / Avg
			FEA	Experiment			
				Run 1	Run 2	Avg	
El Centro NS	100	25.3	0.8	0.9	0.8	0.9	0.9
El Centro NS	100	55.1	1	1.3	1.2	1.3	0.8
El Centro NS	100	79.1	1.4	1.7	1.6	1.7	0.8
Managua EW	100	25.3	0.4	0.2	0.2	0.2	2.0
Managua EW	100	55.1	1.1	0.7	0.7	0.7	1.6
Managua EW	100	105.5	1.45	1.2	1.3	1.3	1.2
Managua EW	109	105.5	2	1.6	2	1.8	1.1
Victoria NS	100	25.3	0.35	0.3	0.3	0.3	1.2
Victoria NS	100	55.1	0.57	0.5	0.5	0.5	1.1
Victoria NS	100	105.5	1.98	2.4	2.2	2.3	0.9
Parkfield NS	100	199.9	1.3	1.3	1.2	1.2	1.1
L`Aquila EW	100	199.9	2	1.4	1.6	1.5	1.4
						Overall average =	1.17

4.6 Discussion and Conclusions

Dynamic tests of a SDOF with PXCMs system were conducted with five different ground motion records and eight different masses. It was observed that the SDOF with PXCMs system exhibited non-linear behavior without permanent deformation under seismic demands. Comparisons of the maximum displacement of the system from FE simulations with measured displacements from experiments are shown in Figure 4.8. FE simulations tended to overestimate the maximum displacement of the system, particularly for the 1940 El Centro ground motion. On average, the ratio of estimated peak displacement to measured peak displacement was 1.17 with a coefficient of variation (CoV) of 22%, indicating that FEA provides reasonable estimates of displacement demand for SDOF-PXCM systems. In summary, PXCMs are a suitable alternatives or supplements to traditional materials because they can undergo global nonlinearity and hence limit forces in buildings, without experiencing permanent deformations.

4.7 Contributions

The work in this chapter was done in collaboration with Prateek Shah and William Pollalis from Prof. Santiago Pujol's research group and Nilesh Mankame from General Motors. The concept was initially conceived by Santiago Pujol and Pablo Zavattieri. David Restrepo designed the PXCMs samples. Nilesh D. Mankame helped with designs and fabricated the sample at General Motors. All the experiments in this section were conducted by Prateek P. Shah and William G. Pollalis from Prof. Santiago Pujol's research group. Yunlan Zhang helped to design the experiments and conducted numerical analysis.

5. ENERGY DISSIPATION IN FUNCTIONALLY TWO-DIMENSIONAL PHASE TRANSFORMING CELLULAR MATERIALS

The work in this chapter was done in collaboration with Nilesh D. Mankame from General Motors, David Restrepo from The University of Texas at San Antonio, and Mirian Velay-Lizancos from Purdue University. A version of this chapter has been previously published in Scientific Reports https://doi.org/10.1038/s41598-019-48581-8

5.1 Overview

Plastic deformation of cellular materials such as metal foams and honeycombs is commonly used for absorbing and dissipating energy because these materials can absorb large amounts of energy per unit mass[47]. However, the deformation in these cases is irreversible and hence, the material can only be used for a single energy absorption event. Phase Transforming Cellular Materials (PXCMs) are a class of periodic cellular materials that exhibit reversible, solid state energy absorption and dissipation[19] and are comparable to honeycombs, especially at low plateau stresses. Moreover, PXCMs can be used multiple times as they do not rely on irreversible deformation of their base material for energy dissipation. The elementary building blocks of PXCMs exhibit multiple stable or meta-stable configurations[19,35,48]. Each stable or metastable configuration defines a phase at the building blocks level, and the transitions between these building block configurations can be interpreted as phase transformations. The ability of these materials to exhibit reversible solid state energy dissipation arises from the storage and subsequent non-equilibrium release of strain energy accompanying the limit point traversals underlying these transitions. The mechanical response of an ensemble of building blocks shows separate loading and unloading plateaus that are characteristic of solid state phase transformations in NiTi alloys[49] and configurational changes in biological shock absorbers like the protein titin in sarcomeres[50,51].

PXCMs have been proposed for applications such reusable, solid state energy absorption[19–21], shock or impact isolation[22,23], and reconfigurable structures[24,25]. PXCMs have also been used to create metamaterials whose mechanical properties (e.g. compressive modulus, wave propagation behavior) can be altered after the material has been fabricated[20,22,26]. Many of the PXCMs cited

above are structurally two or three-dimensional materials because they can resist loads applied along with arbitrary directions in the plane and space respectively. However, they are functionally one-dimensional materials because they exhibit significant solid state energy dissipation only for loads applied along a preferred loading direction. Some recent work addresses materials that exhibit solid state energy dissipation for loads applied along multiple directions. Straightforward extensions of the functionally one-dimensional PXCM design to two and three dimensions have been proposed by Shan et al. and Ren et al. [27,28]. Topology optimization based automatic synthesis techniques have been used to generate functionally two-dimensional PXCM unit cells[29]. A two-dimensional PXCM unit cell featuring a 5-bar planar truss and a three-dimensional tetrahedral PXCM unit cell have been proposed recently[30]. Some of the material designs proposed for auxetic materials[31] and shape reconfigurable materials [25] have the potential to be functionally two and three-dimensional PXCMs. The Miura-ori pattern based metamaterials[32], three-dimensional arrays of spherical shells with patterned holes or Bucklicrystals[33] and the tape based three dimensional multistable structures[34] are other examples of materials that might function as two or three-dimensional PXCMs. However, in most of the above works the emphasis has either been on the one-dimensional variant of the design or on the response of the higher dimensional material designs to uniaxial loads applied along one direction. In this paper, two designs for functionally two-dimensional PXCMs are studied. The first design is based on a square motif and exhibits four axes of reflectional symmetry (similar to [27–29]). The second design is based on a triangular motif and has six axes of symmetry.

5.2 Design considerations

This chapter first describes how multiple instances of the elementary bistable beam mechanism, considered as the basic building block, can be arranged to create several functionally two-dimensional PXCMs. The shape of the elementary beam is that of the first buckling mode of a straight prismatic beam under axial loading (Figure 5.1), represented by $Y = (A/2)[1 - cos(2\pi X/\lambda)]$, where A is the peak to valley amplitude and λ is the wavelength. A concentrated load F is applied to the beam at its apex, orthogonal to the line OP that joins the two ends of the beam, and the resulting displacement d at the apex of the beam is noted.

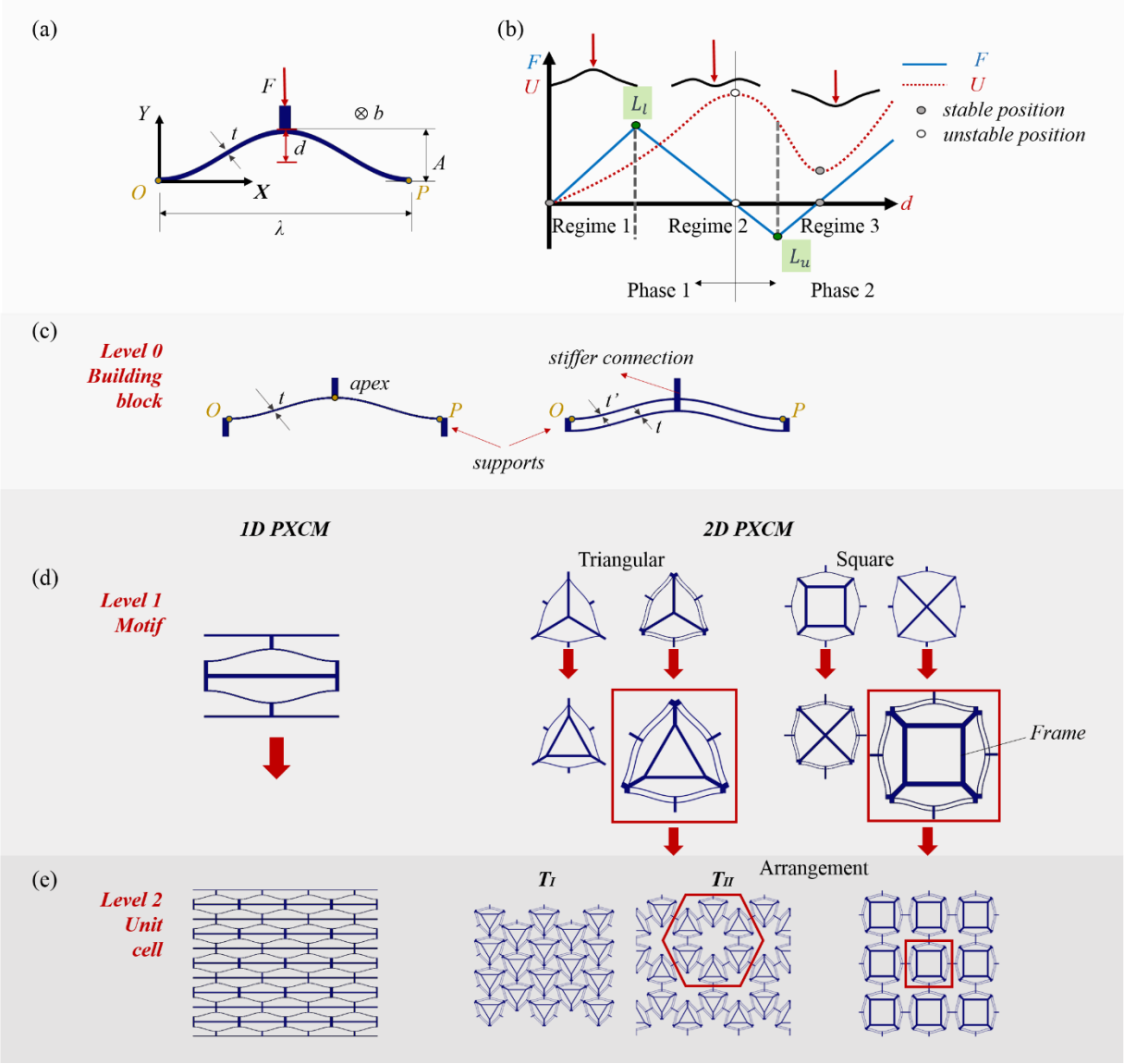

Figure 5.1: Hierarchical construction of functionally two-dimensional PXCMs. (a) The geometry of the elementary sinusoidal beam. (b) Schematic representation of the force-displacement (*F*-*d*) and energy-displacement (*U*-*d*) response of a bistable sinusoidal beam. (c – e) Levels 0 – 2 of the hierarchical structure of the 2D PXCMs studied in this work.

The mechanical response for this beam is shown schematically in Figure 5.1b. The total internal energy U (red dashed line) has three extremal points: 1) a stable global minimum in the undeformed configuration (d=0, F=0), 2) an unstable maximum at (d=A, F=0), and 3) a stable local minimum at (d>A, F=0). The force-displacement response (solid blue line) has two positive stiffness branches that are separated by a negative stiffness branch. Two elastic limit points (L_l for increasing loads and L_u for decreasing loads) mark the ends of the negative stiffness branch. They

also divide the *F-d* response into three regions as shown in Figure 5.1b. Strain energy is stored in the structure during the deformation from the undeformed configuration to L_l. If the structure is loaded beyond this point, it 'snaps-through' under force-control to the point on the second positive stiffness branch that can support the same load. This snap-through is associated with the non-equilibrium release of some of the stored strain energy which gives PXCMs their ability to dissipate energy without undergoing irreversible deformation. A similar behavior is observed during unloading when the structure snaps-through under force control from L_u to the point on the first positive stiffness branch that can support the same load.

The dimensionless parameter $Q=A/t$ governs the number of stable configurations for this structure as follows [38,39]:

1) Metastable: If $Q<2.31$, the mechanism has only one stable configuration at ($d=0$, $F=0$) as the configuration corresponding to the third extremal point ($d > A$) does not persist when the applied load is removed.

2) Bistable: If $Q\geq2.31$, the mechanism has two stable configurations as discussed earlier. The mechanism can persist indefinitely in either of the stable configurations when the external load is removed.

In the interval $Q\epsilon[2.3,2.41]$, the behavior of the mechanism is sensitive to small variations in the geometry parameters, and hence cannot be characterized in a robust manner [19].

Qiu et al. proposed an alternative design that uses two parallel sinusoidal beams (see Figure 5.1c) that can improve the range over which the sinusoidal beam mechanism exhibits bistable behavior [38,39]. The stiffer connection between the two beams at their apexes mitigates the tendency of the single beam to rotate at that location in the absence of an external rotational constraint. This suppresses an asymmetric mode that allows the single beam mechanism to revert back to its undeformed configuration when the external load is removed. This design adds two more geometry parameters: the thickness *t*' of the top sinusoidal beam and the spacing *s* between the two beams (see Figure B1; in Appendix B). The parallel sinusoidal beam mechanism can be used instead of, or in conjunction with the single sinusoidal beam mechanism discussed earlier.

Figure 5.1c-e show how 1D and 2D PXCMs can be constructed in a hierarchical manner beginning with the elementary beam structures shown in Figure 5.1a. At the *zeroth* level of hierarchy (Figure 5.1c), these building blocks comprising one or more elementary sinusoidal beam structures constitute the *first* level of hierarchy (Figure 5.1d). In addition to these sinusoidal beam structures, the building blocks also include supports which are much stiffer than the sinusoidal beams. These structural supports need to be sufficiently stiff so that the elementary beam structures can exhibit the limit point traversal behavior that is essential for energy dissipation, without adding too much mass into the system. Triangular and square motifs are natural candidates for building the *first* hieratical level of 2D PXCMs because of they can be tessellated to cover a plane[52,53]. However, the choice of the support structures for these building blocks is not straightforward. Two alternative support structure topologies are shown in Figure 5.1d (Figure B2). The bulk 2D PXCM material constitutes the *second* level of the hierarchy. The square motif can be tiled only in one way as shown in Figure 5.1e [29]. However, the triangular motif can be arranged in two different ways as shown in Figure 5.1e. The regular tiling (T_I) does not lead to a functionally two-dimensional PXCM (see Figure B3). The arrangement shown in (T_{II}) with triangular motifs located at the nodes of a regular hexagon is not a tiling as it includes some empty space at the center of the hexagon. However, this arrangement yields a functionally 2D PXCM. The *third* level of this hierarchy would comprise a structural member that is made of the 2D PXCM, but is not shown in Figure 5.1.

While several combinations of the above design choices are possible, only some of these lead to robust functionally two-dimensional PXCMs. If the rotation at the apex of the single sinusoidal beam mechanisms is not restrained, ensembles of such mechanisms may exhibit local 'wobble' modes that give rise to unpredictable and disorderly transformation behavior (see Figure B1). On the other hand, the 2D PXCMs with the parallel sinusoidal beam mechanisms do not suffer from this drawback. They exhibit higher energy dissipation and a more stable deformation behavior than the corresponding 2D PXCM comprising single sinusoidal beam mechanisms. For the same mass of the support structures, the designs with just spokes are much less stiff than the designs with a central frame and spoke construction (see Figure B2). The latter support topology also gives rise to higher energy dissipation and repeatable material behavior for the reasons discussed above. Hence, the frame and spoke support topology are used for the designs in this work (See Video 8). When every sinusoidal beam in an ensemble of sinusoidal beam mechanisms transition from the

first stable configuration (regime 1 of the mechanical response as shown in Figure 5.1b) to the second stable (or metastable) configuration (regime 3), the topology of the building blocks remains unchanged but there is a cooperative rearrangement of the elements of the block. This is reminiscent of the non-diffusive rearrangement of atoms in a solid state displacive phase transformations. Many phase changes in physical systems are associated with a discontinuous change in the first derivative of a state variable. In PXCMs, there is a step change in the specific volume of the ensemble because the beams are packed more closely together in the second (meta-)stable configuration than in the first stable configuration. This analogy leads to the following interpretation for PXCMs. When all sinusoidal beams in a part of a PXCM sample are in regimes 1 or 3, that part of the PXCM is said to be in phases 1 or 2 respectively (Figure 5.1b). Any intermediate stage when some beams in a part of a PXCM are in phase 1 and others are in phase 2, the part of the PXCM is deemed to be a mixture of phases. The transformation from phase 1 to phase 2 is referred to as the *forward phase transformation*, while that from phase 2 to phase 1 is called the *reverse phase transformation*.

The geometries of the two motifs – the square-shaped *S-type* and the triangular-shaped *T-type* – are shown in Figure 5.2. The values assigned to the various design parameters are summarized in Table B1. These parameter values are selected such that the base material remains in the elastic regime while undergoing phase transition over multiple loading cycles [38,39]. The axes of reflectional symmetry for the materials are overlaid in red dashed lines in Figure 5.2. In this paper, axes of symmetry refer to planes of symmetry in a three-dimensional setting. The *T-type* motif has three axes of symmetry, the 2D PXCMs unit cell comprising these motifs have six axes of symmetry (see Figure 5.2d). Three of these are derived from those of the motifs and the other three arise from the hexagonal arrangement of the motifs to form the PXCMs. The *S-type* PXCM and its motifs both have four axes of symmetry (see Figure 5.2e).

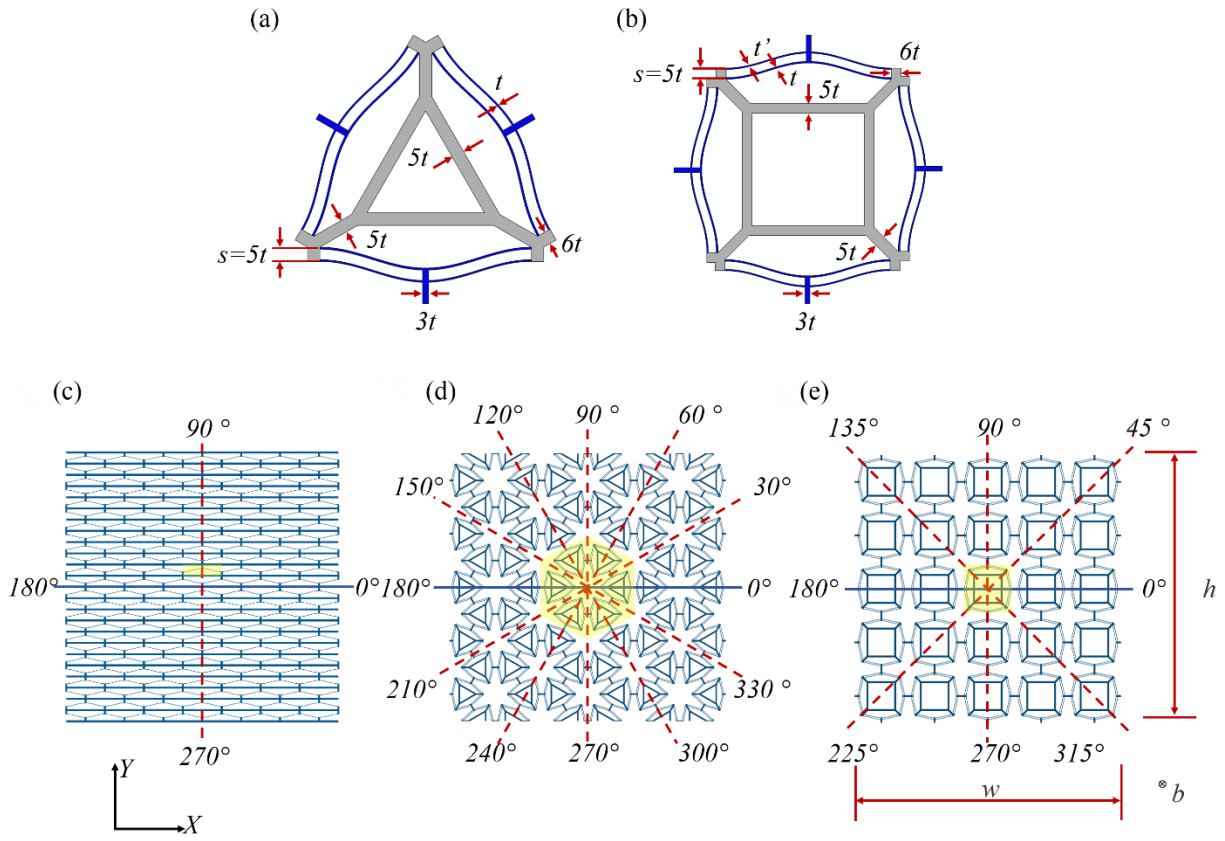

Figure 5.2: Geometry of the (a) *T-type* and (b) *S-type* PXCMs motifs. (c) 1D PXCM has two axes of symmetry at {0˚, 90˚}, (d) the *T-type* 2D PXCM have six axes of symmetry at {0˚, 30˚, 60˚, 90˚, 120˚, 150˚}, and (e) the *S-type* 2D PXCM has four axes of symmetry at {0˚, 45˚, 90˚, 135˚}.

5.3 Results

Uniaxial, quasi-static, compressive load-unload tests are used to characterize the response of the *S-* and *T-* type PXCMs along the various axes of symmetry for the materials. These load cases are then recreated using nonlinear finite element analyses. More complex two-dimensional load cases such as bi-axial loading, bending and indentation are outside the scope of this paper and will be addressed in a future publication. In the figures that follow, the coordinate system $\{a_1,a_2\}$ is embedded in the material sample. This rotates relative to the fixed global coordinate system {*X*, *Y*} as the samples are loaded along different axes. Material symmetries render loading along some of the axes of symmetry to be equivalent to loading along other axes. This reduces the number of load cases that need to be considered in this study.

Figure 5.3 summarizes the mechanical response of a functionally two-dimensional *S-type* PXCM. The schematic for this load case is shown in Figure 5.3a where the a_1 axis is aligned with (loading at 0°) or orthogonal to (loading at 90°) the *X*-axis. Figure 5.3b showed three characteristic states during the phase transformation process corresponding to three labeled points in Figure 5.3c. The *F-d* responses from the finite element simulation (solid red line) and the experiment (solid black line) are overlaid in Figure 5.3c. The experimental *F-d* curves for three cycles are presented in Figure B5 (a). The initial (undeformed) and final configurations from the experiment are shown in Figure 5.3d.

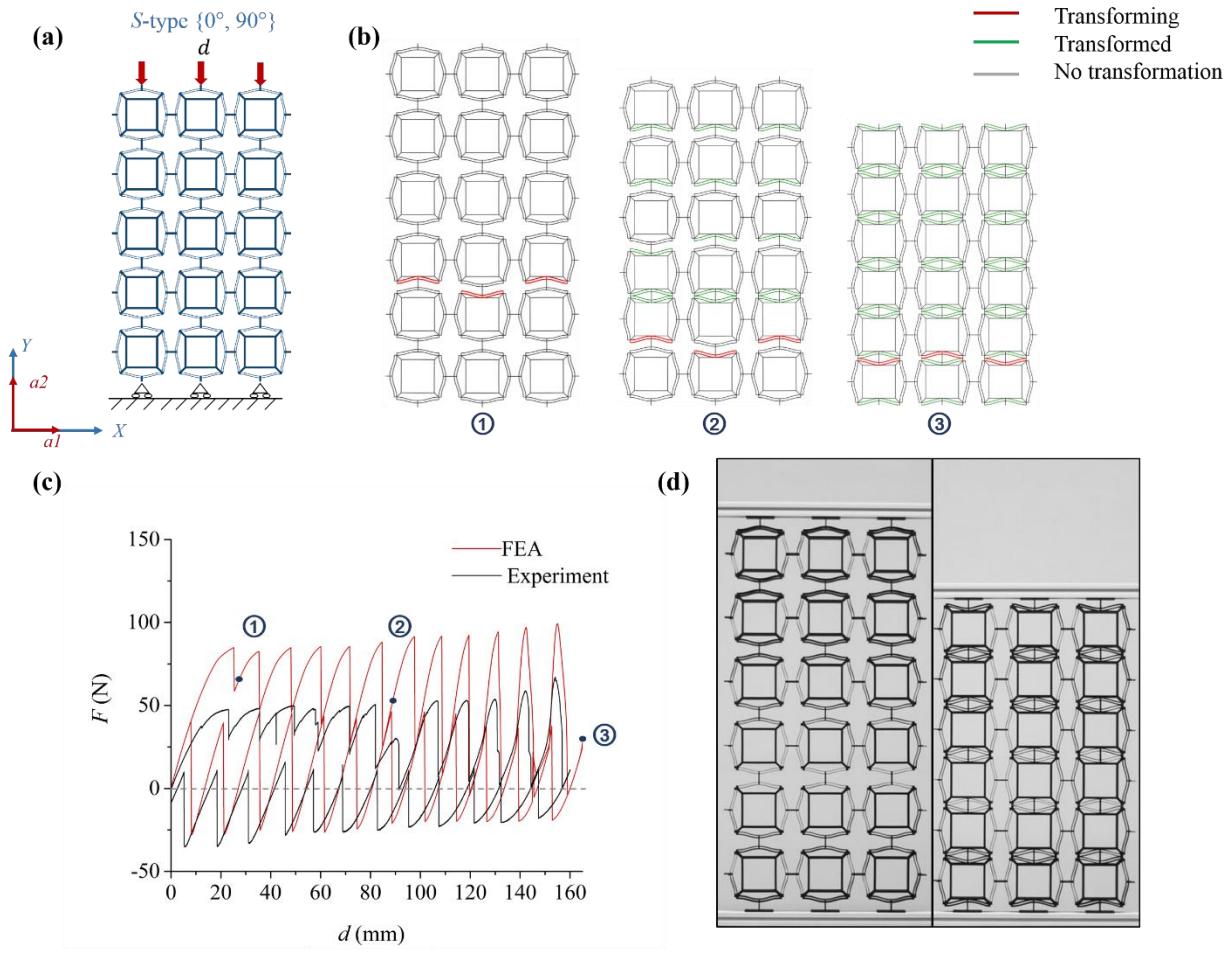

Figure 5.3: Performance of a *S-type* PXCM sample under one compressive load-unload cycle at {0°, 90°}. (a) The sample is under uniaxial loading condition and supported by rollers at bottom. (b) Phase transformation sequence of the three characteristic states from FE simulation. (c). *F-d* relation of the sample from FE simulation and Experiment. (d) The states of the sample at initial and final deformed configurations.

The *F-d* response obtained from the finite element simulations agrees qualitatively with the experimentally recorded one. The finite element and experimental responses show serrated loading and unloading plateaus as expected and shown in 1D PXCM [19]. There are 12 peaks in both branches which correspond to the number of sinusoidal beam elements in any column of motifs in the sample. Each peak marks the transformation of a sinusoidal beam element from phase 1 to phase 2. All cells in this sample exhibit bistable behavior as indicated by the negative compressive (i.e. tensile) force needed to revert the sample back to phase 1. The key quantitative differences between the FE simulations and experimental results are a) the experimental loading and unloading branches lie below the corresponding ones from the finite element simulations and b) one peak in the loading branch of the experimental response is lower than the others. Figure 5.3b shows the deformed configurations of the sample at three salient points during its compression as obtained from the finite element simulations. The corresponding points are labeled on the *F-d* response in Figure 5.3c. The sinusoidal beams are color coded according to their status at that point in the deformation. The beams rendered in gray are still in phase 1, those shaded green have already transformed into phase 2, and the red ones are undergoing phase transformation. Identification of the beams that are either in phase 1 or 2 is straightforward. However, determining which beams are in the process of phase transformation is challenging because the limit point traversal (or snap-through) is a non-equilibrium event that occurs quickly, and the finite element solution is unable to follow it consistently. This difficulty is circumvented by inspecting the states of the sample at the solution points just before and just after the salient point under consideration. Any beams that have changed phases between these two neighboring points are deemed to be undergoing phase transformation at this salient point, and are shaded red in Figure 5.3b.

The locations and distribution of the red beams in Figure 5.3b serve as indicators for the nucleation and propagation of the phase transformations. Note that the beams undergoing phase transformation at these salient points lie along a (horizontal) row in the sample. This indicates that even though the different rows may transform at different levels of global compressive strain, an entire row transforms together. This ensures that the loss of stability is restricted to one row of beams and the rest of the sample remains stable. In turn, this leads to an orderly progressive collapse of the different sinusoidal beam rows as is evident from the regular shapes of the serrations in the *F-d* response. It is observed that only the sinusoidal beams that are approximately parallel

to the a_1 (a_2 for the 90° loading case) axis of the material have undergone phase transformation at the end of the deformation process. Those that are approximately parallel to a_2 (a_1 for the 90° loading case) axis remain in phase 1. Thus, a fairly significant fraction of the sinusoidal beams in the PXCM did not contribute to the energy dissipation in this case.

Figure 5.4 summarizes the response of a *S-type* PXCM with the square-shaped motifs when the a_1 axis of the material is inclined at 45° or 135° to the global X-axis. The various sub-figures for Figure 5.4 are similar to those for Figure 5.3. Figure 5.4c shows qualitative agreement between the experimental and simulated responses. Both responses show loading and unloading plateaus that are separated from each other. However, neither of these responses show a serrated pattern that as distinct as in the previous ({0°, 90°}) case. Also, it is noted that the simulated response in Figure 5.4c shows a PXCM with some mechanisms exhibiting bistable behavior especially near the beginning of the load and unload branches. However, the experimental response is that of a metastable PXCM except at the end of the unloading branch. Recall that the same material behaved like a bistable PXCM for the {0°, 90°} load case. Both observations relate to the fact that the $a_1$axis of the material is now inclined to the applied displacement. As it will be discussed later, the resulting asymmetry reduces the snapping action of the mechanisms changing the nature of the individual transitions, leading to smoother serration in the *F-d* response. Unlike the previous case, all of the sinusoidal beams have transformed into phase 2 by the end of the deformation process. Thus, all of the sinusoidal beams in the PXCM sample contribute to the energy dissipation. Despite this, the energy dissipation capacity of this PXCM is slightly lower (approximately 12% for W_v and 18% for W_m) for the {45°, 135°} loading case than the {0°, 90°} loading case (see Table B4-S6). This is also due to the lower energy dissipation associated with the transition of each sinusoidal beam when the a_1 axis of the material is inclined to the applied displacement. The experimental *F-d* curves for three cycles are presented in Figure B5(b).

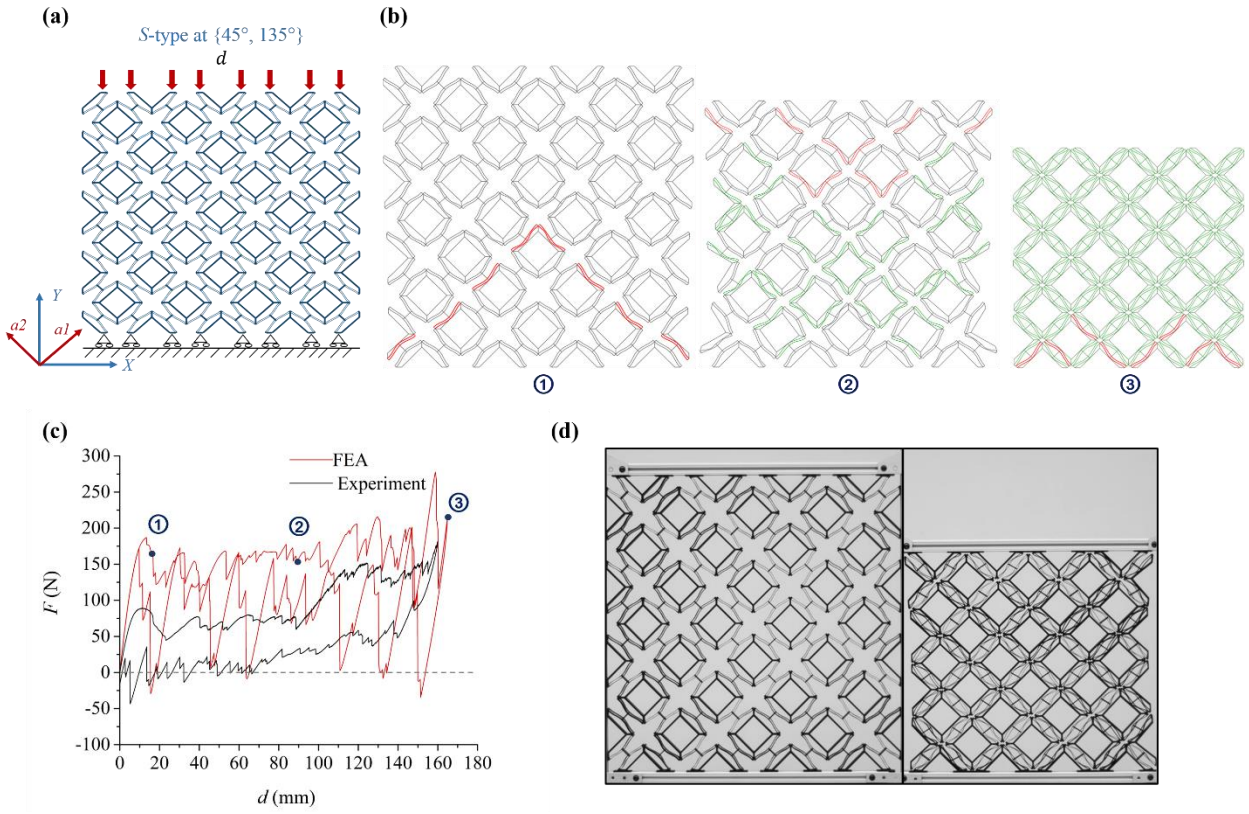

Figure 5.4: Performance of a *S-type* PXCM sample under one compressive load-unload cycle at {45°, 135°}. (a) The sample is under uniaxial loading condition and supported by rollers at bottom. (b) Phase transformation sequence of the three characteristic states from FE simulation. (c). *F-d* relation of the sample from FE simulation and Experiment. (d) The states of the sample at initial and final deformed configurations.

Figure 5.4 c also shows two somewhat different regions in the *F-d* responses. The material seems to respond differently in the applied displacement range of 0-90 mm than for displacements greater than 90 mm. In the experimental response, there is a lower force plateau that extends over the displacement range of 0-90 mm and a higher force plateau that spans the rest of the displacement range. The simulated response shows a smaller difference in the plateau force levels across these two displacement ranges, but it shows more prominent serrations in the higher displacement range than in the lower one. It is also observed that the phase nucleation regions and transformation fronts (see red colored beams in Figure 5.4b) no longer neatly follow motif rows or columns. Instead, zig-zag patterns is observed all the way until densification. Both of these observations suggest the existence of preferred phase transformation propagation bands. The lower energy transformation fronts seem to take the form of long wavelength triangular waves aligned with the

edges of motifs. The higher energy fronts also have the shape of a triangular wave, but these have a shorter wavelength. In a sample of relatively small size, as is the case here, the sinusoidal beams along the lower energy transformation propagation paths get exhausted when the sample is compressed through a displacement equal to 90 mm (60% of maximum displacement), and the material changes over to the sinusoidal beams along the less preferred transformation propagation paths for higher displacements. The small differences between various beams in a fabricated sample lead to an elevated plateau force level for displacements greater than 90 mm in the experimental case. However, as all of the sinusoidal beams are nominally identical in the FE simulations, groups of these beams transform together. This gives rise to the larger oscillations in stress in the simulated response for displacement above 90 mm.

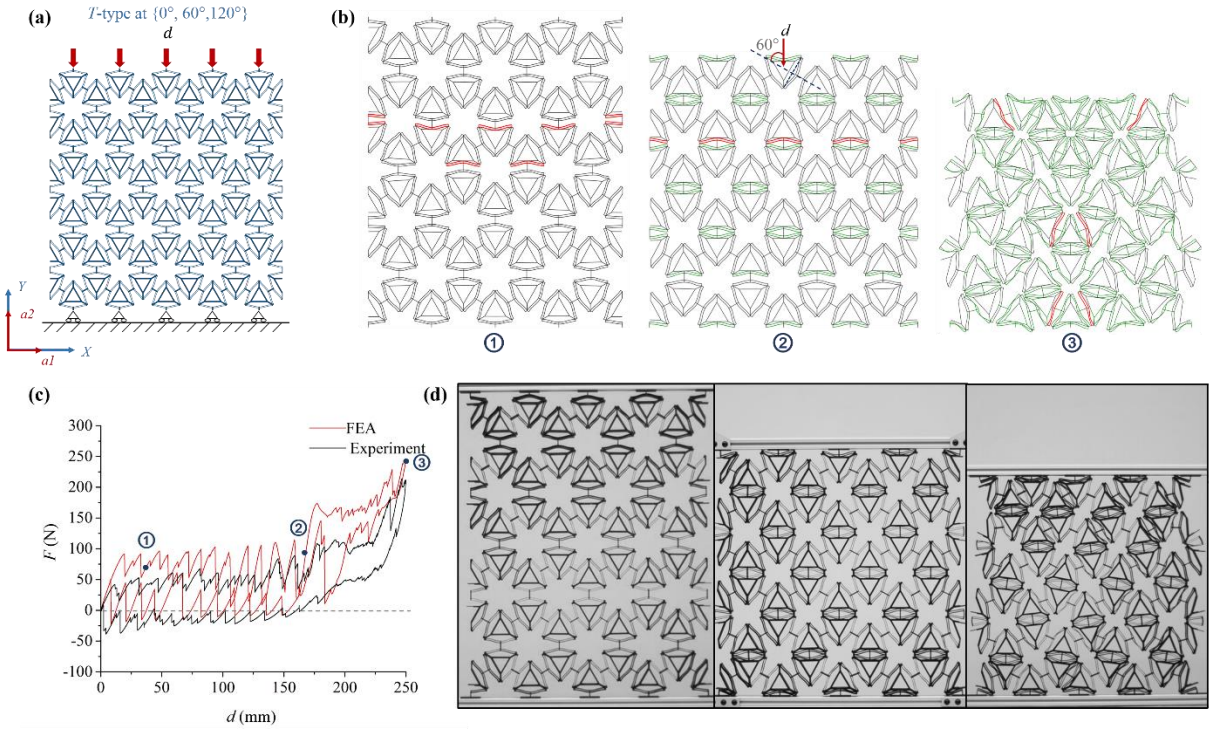

Figure 5.5: Performance of a *T-type* PXCM sample under one compressive load-unload cycle at {0°, 60°, 120°}. (a) The sample is under uniaxial loading condition and supported by rollers at bottom. (b) Phase transformation sequence of the three characteristic states from FE simulation. (c). *F-d* relation of the sample from FE simulation and Experiment. (d) Three states of the sample from initial to final deformed configurations.

The mechanical response (see Figure 5.5) of the *T-type* PXCM under uniaxial loads applied along {0°, 60°, 120°} shares features of the mechanical responses seen in the *S-type* PXCMs under both

{0°,90°} and {45°, 135°} loadings, but is more similar to the latter case. The simulated and experimental *F-d* responses are qualitatively similar. Both responses show some common features but the serrations in the experimental response are much less distinct than those in the simulated response. Both responses show two distinct regions. The experimental and simulated *F-d* responses show serrated loading and unloading plateaus over the displacement range 0-170mm. There is a jump in the plateau force levels associated with both branches for displacements above 170mm. The latter region is also characterized by barely discernable serrations. It is observed that the material behaves like a metastable PXCM for displacement above 170 mm and as a bistable PXCM for lower displacements. The experimental *F-d* curves for three cycles are presented in Figure B5 (c).

As in the case of the PXCM with square-shaped motifs when it is loaded along {45°, 135°} degrees, this dichotomy in the responses can be traced back to the inclination of the applied displacement to the a_1 axis of the material. Approximately a third of the sinusoidal beams in this case are orthogonal to the loading direction. These sinusoidal beams require lower transformation force and transform first and in an orderly progressive manner as suggested by the phase transformation front shown in Figure 5.5b. The loading direction makes a fairly steep angle (60°) with the axis of symmetry of the remaining two- thirds of the sinusoidal beams in the sample (Figure 5.5b). This reduces the tendency of the mechanisms to snap-through, but they still need a sizable displacement component that is normal to line joining the ends of the beams to complete the forward transformation. This results in less distinct serrations as well as a higher plateau force for the transformations in these cells. The compression in simulation and experiment of this sample was stopped before it reached the theoretically determined maximum displacement because of the extreme distortion of the motifs that is seen in the last pane of Figure 5.5d.

The mechanical response of the *T-type* PXCM under uniaxial loads applied along {30°, 90°, 150°} degrees (see Figure 5.6a) shares features of the mechanical responses seen in the *S-type* PXCMs under both {0°,90°} and {45°, 135°} loadings, but is more similar to the former loading case (shown in Figure 5.6b-c). The *F-d* response in Figure 5.6c shows a qualitative agreement between the simulated and experimental responses. Both show serrated loading and unloading plateaus that are sufficiently separated for the material to exhibit energy dissipation. The serrations are not as

regular or distinct as in the {0°, 90°} loading case for the *S-type* PXCM, but they are sufficiently regular and distinct to allow us to identify individual peaks in the loading (or unloading) branches with the forward (or reverse) transformation of one sinusoidal beam structure in a column of motifs. This can be explained by the larger inclination angle (30°) between the loading direction and axis of symmetry of two-thirds of the sinusoidal beam mechanisms in the sample (Figure 5.6b). The phase transforming band fronts in Figure 5.6b follows a slight zig-zag path that mostly hews to horizontal rows of motifs. Thus, it is observed that a mostly orderly progressive transformation of rows of sinusoidal beams until the sample is fully compressed. This is also reflected in the uniformity of the serrations in the *F-d* response.

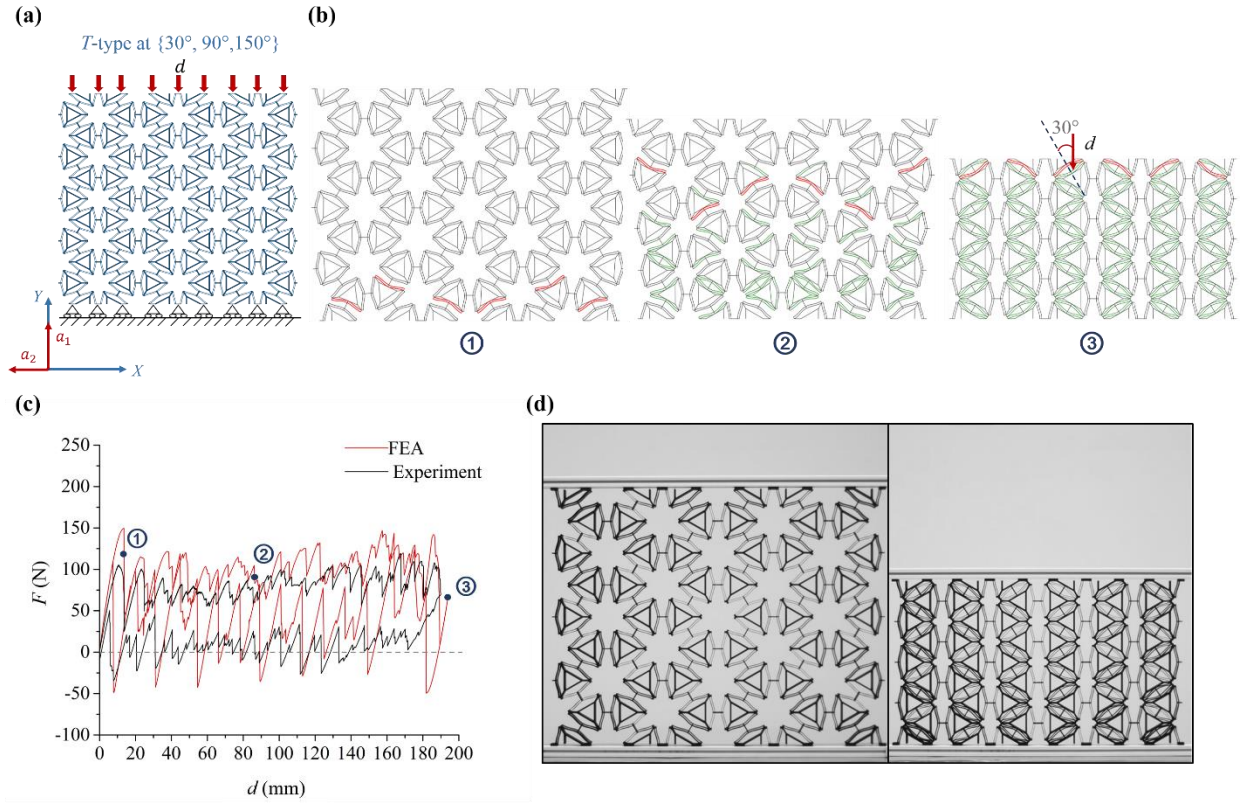

Figure 5.6: Performance of a *T-type* PXCM sample under one compressive load-unload cycle at {30°, 90°, 150°}. (a) The sample is under uniaxial loading condition and supported by rollers at bottom. (b) Phase transformation sequence of the three characteristic states from FE simulation. (c). *F-d* relation of the sample from FE simulation and Experiment. (d) The states of the sample at initial and final deformed configurations.

The experimental response indicates a PXCM whose behavior is right at the boundary between bistable and metastable (Figure 5.6c). The experimental *F-d* curves for three cycles are presented in Figure B5d. The material behaves mostly like a metastable PXCM during the compression of the sample (loading branch), but the sample retains the compacted configuration reached at the end of the loading branch without the need for an external force to hold that configuration. A small tensile force is needed to initiate and subsequently nudge the reverse transformation to completion. The simulated response is similar to the previous two loading cases showing more pronounced serrations in the unloading branch than those observed in the experiments. It is also noted that approximately two-thirds of all sinusoidal beam mechanisms in this PXCM sample undergo phase transformation in this case (see Figure 5.6d). The remaining mechanisms that are approximately parallel to loading direction remain in phase 1 at the end of the compression process (b, d). Recall that almost all the mechanisms in the *T-type* PXCM loaded along {0°, 60°, 120°} underwent phase transformation. As in the case of the *S-type* PXCM, we observe that, because there are more sinusoidal beams in a *T-type* PXCM that undergo phase transformation in for loading along {0°, 60°, 120°} than for loading along {30°, 90°, 150°}, the energy dissipation associated with each of the transitions is lower in the latter case. The results indicate that the *S-type* and *T-type* PXCMs are similar in terms of energy dissipation performance (approximately 12% difference for both load cases).

5.4 Materials and Methods

A Fortus 450MC fused deposition modeling machine from Stratasys is used to fabricate the PXCM samples using an ABS-based proprietary material called ABS-M30 (E=2.28 GPa, σ_y=45 MPa). The thickness of a sinusoidal beam is a critical dimension that drives the size of the sample. Very thin beams lead to small overall sample sizes but these designs are susceptible to significant variations in beam thicknesses across the sample. Here, t= 0.7 mm is selected to balance the need to keep the overall sample size small with the desire to ensure fairly consistent beam thicknesses across the sample. Each sample is made by assembling multiple 3D printed parts, because the complete samples have a bigger footprint than the building envelope of the 3D printer. These parts are then adhesively bonded to create the test samples. The samples are conditioned at room temperature and humidity for at least 48 hours before testing them. Further examination revealed that the adhesive and assembly method does not affect the mechanical response of the specimen.

The samples are tested in uniaxial compression in a universal test machine (MTS Insight 10). Horizontal bars comprising cruciform Aluminum extrusions are used to secure the test samples in the test frame. The test samples are designed such that their top and bottom ends have 'T' shaped features that slide in the T-slots of the horizontal bars. The ends of the sample cannot move vertically nor can they rotate about any axes relative to the horizontal bars. A thin coating of a lubricant is applied to the slots to reduce friction between the samples and the horizontal bars, so that the sample ends can slide freely in the horizontal direction. The out-of-plane width of the sample is chosen to be sufficiently high (25 mm) to mitigate the tendency of the sample to buckle out of plane. However, as a precaution, diagonal bars spanning the entire sample (see Figure B4a) are mounted behind the sample to brace it against deforming out of the plane of the sample. The edges of the samples are free from any boundary conditions.

Four samples that represent the two 2D PXCMs designs, each in two different material orientations, are compressed under displacement control at the quasi-static rate of 1 mm/min. The displacement is applied to ensure the maximum amount of mechanisms collapse (see Figure B4 c). The total force acting on the sample is measured by a load cell (MTS 661.19F-02, 10 kN capacity) and the cross-head travel is recorded as the displacement of the top end of the sample. Each sample is subjected to three back-to-back load-unload cycles to check for repeatability and any evidence of irreversible deformation (see Figure B5). The area enclosed by the loading and unloading branches of the *F-d* response is the energy dissipated by the sample in that cycle. The average energy dissipation from the second and third cycles is used to represent the energy dissipation capacity of the material for that load case.

Although the PXCM samples are loaded in displacement controlled at a quasi-static global deformation rate of 1 mm/min, the limit point traversals in the various beams are dynamic events with fairly short characteristic times (Q(1 ms)). Moreover, contact between adjacent structural elements in the PXCM and the non-equilibrium jumps associated with the snap-throughs introduce significant nonlinearity in the response of the PXCM. Displacement controlled, direct integration, implicit dynamic finite element analyses in a finite element analysis software Abaqus 6.15 provides a robust way to simulate the complex behavior of these materials. The FE simulations in

this work use a two-node, shear flexible beam element discretization of the PXCM samples. Results from beam, 2D and 3D solid element discretizations were compared for accuracy of the solution as well as its computational cost (Figure B13). The element sizes were determined through a convergence study (Figure B14).

The mechanical properties employed in the FE simulations are those corresponding to ABS-M30 (which are reported in Section B4.4, Tables B9 & B10). Considering the experimental and material variability (i.e., lower and upper bound of these properties) the simulated *F-d* curves are reported in Figure B17. In order to properly simulate the experimental boundary conditions shown in Figures 5.3-5.6a, the corresponding FE simulations had a frictionless roller boundary at the interface with the ground, the sides were free from any displacement constraints or tractions and a uniform velocity of 1 mm/min was applied to all nodes on the top edge of the sample. Contact between adjacent beams was modeled using the small sliding formulation in Abaqus. Coulomb friction with a friction coefficient of $\mu = 0.1$ was assumed to be active at all contact interfaces (See discussion in section B4.3 and Figure B15).

5.5 Discussion

The variation in the energy dissipation performance of the two 2D PXCMs with the axis of loading is an important functional attribute of the 2D PXCMs. In this section we compare the performance of the two 2D PXCM designs based on two metrics: W_m (energy dissipated per unit mass) and W_v (energy dissipated per unit volume) for loads applied along various axes of symmetry of the materials. We also estimate the fraction of the total dissipated energy that is dissipated via pathways other than the snapping action of the beams in the samples. Panes (a) and (b) in Figure 5.7 summarize respectively the volume-specific (W_v) and mass-specific (W_m) energy dissipation capacity as a function of the loading angle for the two 2D PXCM designs presented earlier. The average energy dissipated by a sample in cycles 2 and 3 in the experiments and the FE simulation can either be normalized by the volume of the undeformed bounding box that encloses the sample (see Figure 5.2 and Table B2) or by the mass of the sample to get its W_v and W_m performance respectively. Energy dissipation in PXCMs occurs in a discontinuous way through discrete steps corresponding to snap-through transitions in individual building blocks. Therefore, energy dissipation per unit displacement cannot be defined in the traditional way involving ratios of

infinitesimal changes in energy dissipation and displacements. However, an average energy dissipation rate can be defined in the following way: the material is loaded up to a snap-through at a displacement d_1, and then unload it completely. As such the average energy dissipation rate at d_1 can be defined as the ratio between the energy dissipated in this complete load-unload cycle, W_m (d_1) and the applied displacement d_1. This is repeated for all snap-through events to get the average energy dissipation, $W_m(d)$, for different displacement values through its loading history. Figure 5.7(c) shows W_m a function of d calculated from the FE models. With the exception of the *S-type* PXCM for {0°, 90°}, that exhibits a higher energy dissipation rate, the rest of the samples show similar performance. More discussion can be found in Appendix B Section B5 (Table B12).

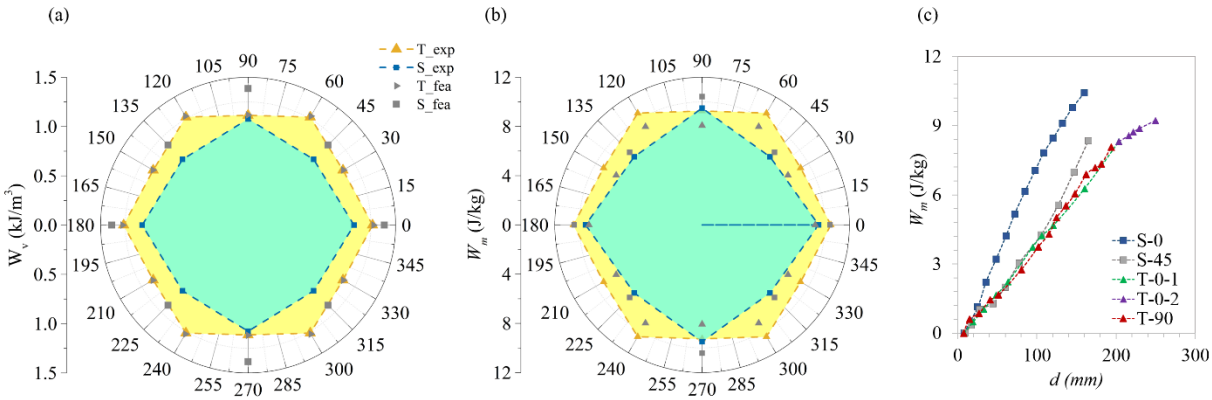

Figure 5.7: (a) W_v – energy dissipation per unit volume, (b) W_m – energy dissipation per unit mass, as a function of the loading angle for the two 2D PXCMs presented here. Gold triangular and blue square symbols represent experimental results of *T-type* and *S-type* PXCMs. Gray triangular and square symbols represent simulation results of *T-type* and *S-type* PXCMs. (c) Energy dissipation W_m varies with applied displacement.

A couple of observations are noteworthy: (1) W_v and W_m for both 2D PXCM designs do not vary significantly with the loading direction for loads applied along the various axes of symmetry for the materials. (2) The *T-type* PXCM has a small performance advantage over the *S-type* PXCM in terms of both - W_v and W_m. These observations are not readily apparent when we recall (see Figures 5.3-5.6) that the mechanical responses of the two 2D PXCM designs were quite different under loads applied along the various axes of symmetry for the materials (shown in Figure B6). Furthermore, those results do not shed any light on how the material might respond when it is subjected to loads that are applied along a more general direction in the plane i.e. not along an axis

of symmetry for the material. We carried out ancillary analysis done on a single mechanism comprising two parallel sinusoidal beams to understand the role of the loading directions on its bistable behavior (see Section B3.2). We found that the ability of this mechanism to exhibit bistability decreases with the angle between the loading direction and the axis of symmetry of the sinusoidal beam to the extent that the mechanisms ceases to exhibit negative stiffness when the such angle is higher than 15^{o} (see Figure 5.7). In principle, this effect would degrade the capability of the material to dissipate energy. However, a closer examination at the PXCMs analyzed in Figs. 5.4-6 reveals that the individual cells in a larger ensemble reorient themselves during the deformation of the material, such that they reduce the inclination of the force deforming a mechanism with respect to the axis of symmetry of the mechanism undergoing transformation improving their bistability and therefore their capability to energy dissipation (see Figs. B8-10 in Section B3.2).

The variation in energy dissipation across successive cycles for all four load cases is less than 8% (Table B3*)*. The highest variations for the different load cases occur at the transition from cycle 1 to cycle 2 and are likely due to initial inelastic behavior of the sample and stress concertation. There is a very little variation from cycle to cycle across subsequent cycles (Table B4). The overall highest variation is reported for the *S-type* PXCM sample with the square-based motif when it is loaded at {0°, 90°}. In addition to the snapping action of the mechanisms, other energy dissipation pathways may also contribute to the observed energy dissipation in the experiments e.g. a) plastic dissipation within the polymeric base material, b) viscous dissipation within the base material, c) frictional dissipation due to rubbing between the sample and its boundaries, d) friction between the sample and the guards that limit out of plane deformation, e) friction between adjacent beams that come into contact during the deformation of individual mechanisms in the sample, and f). internal friction between the various layers that are deposited by the rapid prototyping process. The energy dissipation due to the snapping action of the beams is considered to be the primary dissipation pathway for PXCMs. The total energy dissipated by PXCM sample can be attributed to the primary and secondary pathways is estimated (see B3.3, Table B7-8).

In conclusion, this chapter presents the study of functionally 2D *S*- and *T-type* PXCMs that exhibit significant energy dissipation when they are loaded along multiple directions. Experiments on 3D

printed prototypes, together with nonlinear finite element simulations, were employed to examine and understand the mechanical behavior of these materials. The experimental results show that the energy dissipation capacity of both PXCM designs did not vary substantially with the direction of loading. It is also noted that the results reported in this work are for samples with a relatively small number of motifs. Replicating these experiments for samples with a significantly larger number of motifs is critical for understanding the true material response. The analysis of their response to more complex load cases such as bi-axial, bending and indentation is the focus of ongoing work that will be reported in the future. However, these materials offer a myriad of opportunities for developing applications such as those mentioned in the introduction. Moreover, it is also observed that both designs exhibited auxetic behavior. *S-type* samples exhibited a Poisson's ratio in the range of -1 to 0, whereas *T-type* samples exhibited Poisson's ratio in the range -1.1 to -0.29 (See Figure B12). Having these auxetic behavior indicates that 2D PXCMs might have additional mechanical advantages, such as high indentation resistance, shear modulus, fracture toughness, and synclasticity [54,55] , which extend the application of 2D PXCMs into medical stent [56], and self-adaptive attire [57].

5.6 Future works

5.6.1 Response of PXCMs under concentrated loading conditions

Chapters 5.1-5.5 discussed PXCMs subjected to uniform distributed loading conditions during which a tradeoff between localized deformation in the material and the energy dissipation capacity of the material was observed in 2D PXCMs. To further investigate this tradeoff, a study of both 1D PXCMs and 2D PXCMs under a concentrated cyclic loading condition will be conducted. Understanding the response of PXCMs under concentrated loading conditions can also allow us to access the feasibility of more applications of PXCMs such as Non-pneumatic tires, armors, and protection gear, such as football helmets and car bumpers.

5.6.2 FE simulations

To evaluate the performance of PXCMs under concentrated loading conditions, the mechanical response of 1D and 2D PXCMs undergo the indentation will be studied. FE simulations were created to evaluate the performance of 1D PXCM and 2D PXCMs. As Figure 5.8-Figure 5.10 show below, the coordinate system $\{a_1, a_2\}$ is embedded in the material sample, which rotates

relative to the fixed global coordinate system {*X*, *Y*} as the samples are loaded along different axes. Material symmetries render loading along some of the material axes of symmetry to be equivalent to loading along other axes. This reduces the number of load cases that need to be considered in this study. Here only 1D PXCMs loaded along 0°, *S-type* PXCMs loaded along 0° and 45°, *S-type* PXCMs loaded along 0° and 90° are studied. All the samples were modeled using implicit dynamic finite element analysis in a commercial software, Abaqus 6.18. Two-node, shear flexible beam element, B21, were used to create the models. In each model, a sample was loaded by a rigid cylindrical indenter with a constant radius 326 mm. A same sized indentator was applied on each sample under the same loading rate of 1mm/sec. The boundary conditions are consistent among models, which is rollers applied on the bottom of each sample to prevent the displacement in *Y* direction, and one point along the middle line was constrained in *X* direction (Figure 5.8-Figure 5.10). The samples share similar dimensions and mass as that which was presented in Table 5.1.

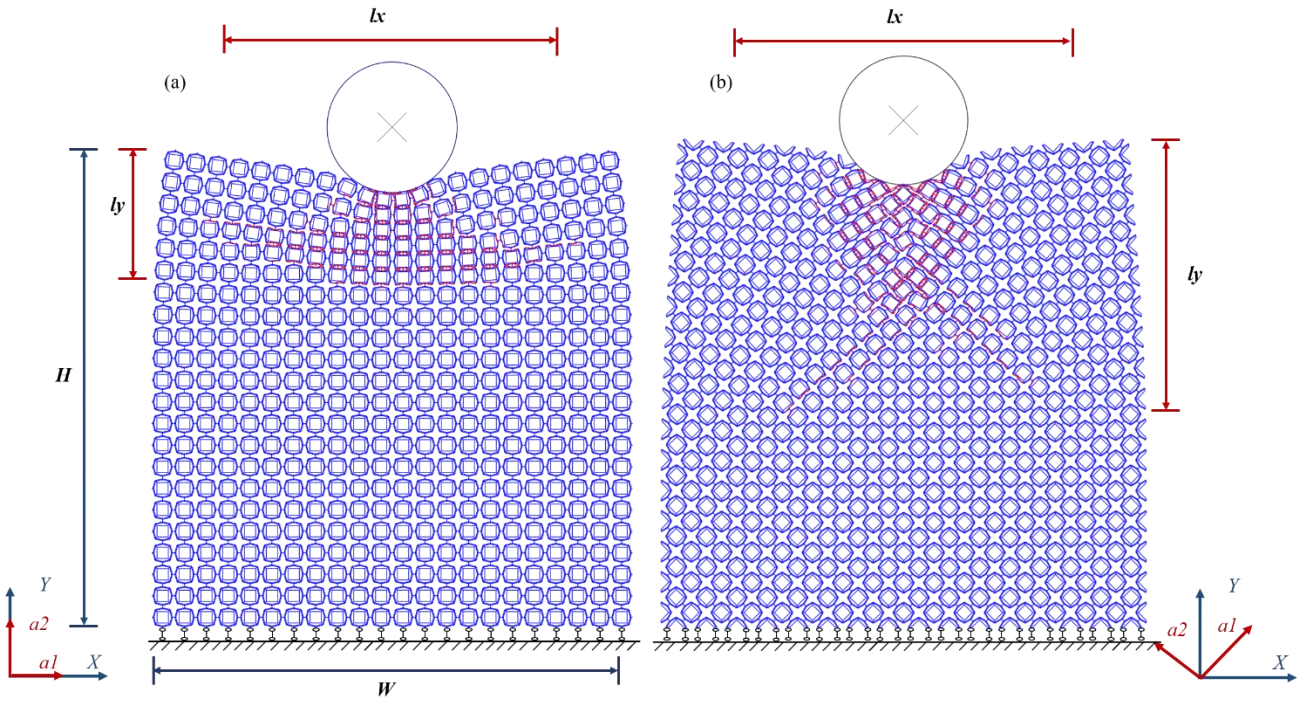

Figure 5.8: Deformed of *S-type* PXCMs samples indented along 0° and 45°.

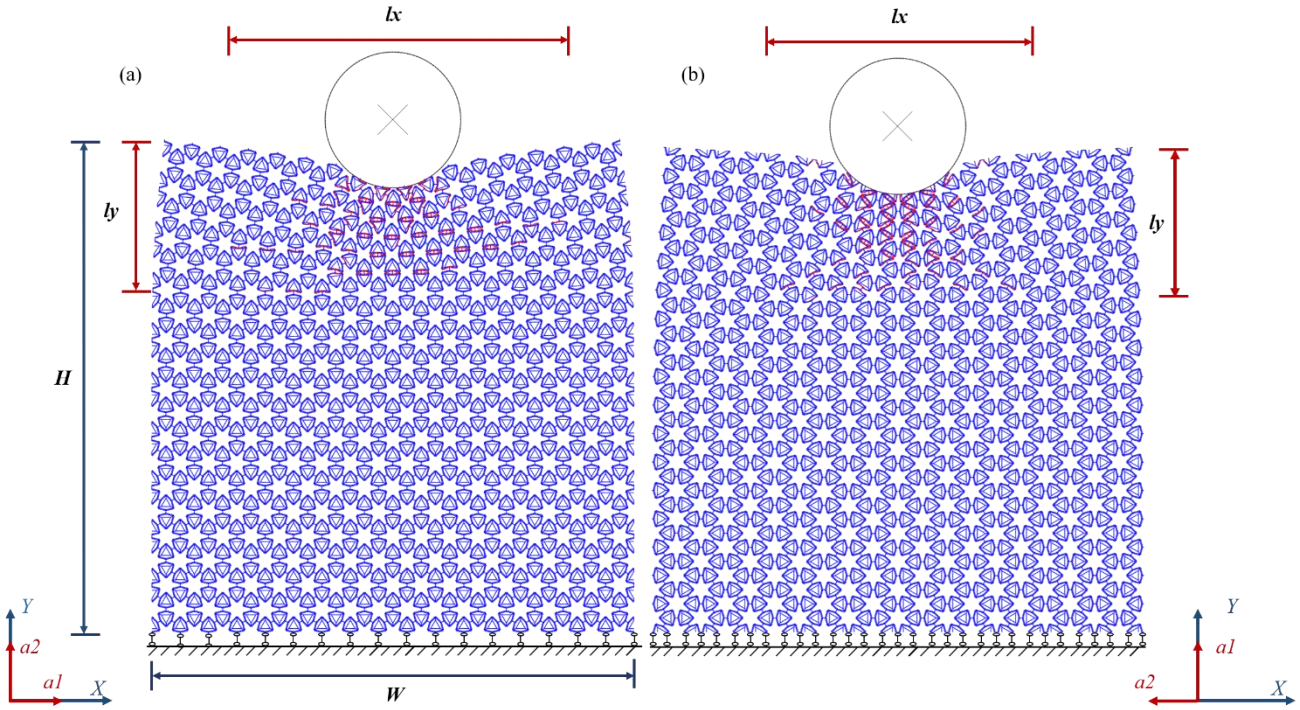

Figure 5.9: Deformed of *T-type* PXCMs samples indented along 0° and 90°.

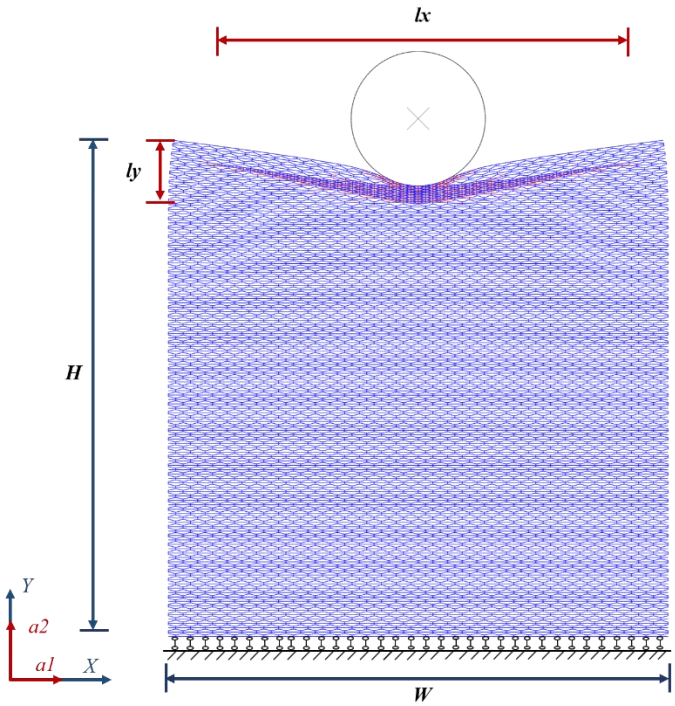

Figure 5.10: Deformed 1D PXCMs sample indented along 0°.

Under concentrated loading test, the 2D PXCMs samples exhibit asymmetric phase transformation regions. On the contrary, the building blocks composing the 1D PXCMs exhibit phase transformation which are symmetric to the loading direction (see Figure 5.8 and Figure 5.10). When the 1D PXCMs, *S-type* and *T-type* 2D PXCMs samples undergo the load along 0° (parallel to a_2), the sinusoidal beams that are approximately parallel to the a_1 (a_2 for the 90° loading case) axis of the material have undergone phase transformation. The sinusoidal beams that are approximately parallel to a_2 (a_1 for the 90° loading case) axis remain in phase 1. The phase transformation band spread widely in *X* direction (perpendicular to the loading direction) and spread to a shallow depth in *Y* direction (parallel to the loading direction). When the *S-type* and *T-type* 2D PXCMs samples underwent the concentrated loading along 45° and 90° respectively, the phase transformation occurred in the sinusoidal beams are inclined to the loading direction. When the *T-type* 2D PXCMs sample underwent the concentrated loading along 90°, those sinusoidal beams that were approximately parallel to the a_2 hardly exhibited phase transformation. In contrast to these *S-type* and *T-type* 2D PXCMs samples undergo concentrated loading along 0° exhibit phase transformation band spread widely in the *Y* direction (parallel to the loading direction) and spread to a shallow depth in the *X* direction (perpendicular to the loading direction). The spreading distance was measured by the distance between the edges of the region -l_X and l_Y - as shown in Figure 5.8 and Figure 5.10. The length of the phase transformation band caused by the indenter (spreading distance in *Y* by *X* direction) are normalized by the corresponding dimensions and are summarized in Table 5.2. Poisson's effects were also studied to capture the auxetic behavior of each PXCM simulation. The average deformation along the four edges (*W* and *H*) were used to approximate the Poisson's ratio and the results are also displayed in Table 5.2. To show the correlation between auxetics and phase transformation path, the normalized phase transformation range are plotted against the approximated Poisson's ratio as shown in Figure 5.17. The figure shows, larger magnitude of the negative Poisson's ratio corresponds to a larger spread of phase transformation in composing building blocks along the loading direction, whilst less spread is occurred in the direction perpendicular to the loading direction.

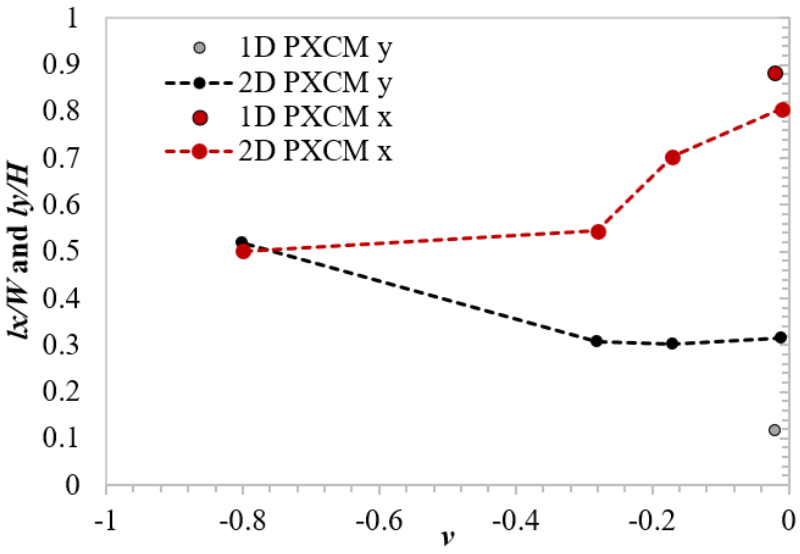

Figure 5.11: Phase transformation spread in x and y direction.

The energy dissipation caused by concentrated load is also studied. The *F-d* relationship of five samples which have undergone the indentation are presented in Figure 5.12-Figure 5.15. In these figures, the applied force increases progressively with the applied displacement because the width of the transformation band increases proportionally. *S-type* 2D PXCMs exhibit higher reaction force compared with *T-type* 2D PXCMs and 1D PXCMs. Energy dissipation is quantified by the area between the hysteresis curve. The energy dissipation per unit volume and per unit mass by these PXCM models under concentrated loading are plotted in Figure 5.16. Similar to the observation from the study of 2D PXCMs undergoing the uniform loading condition, *S-type* 2D PXCMs exhibit more uniform energy dissipation capacity when the indentation loading angles vary. It was observed that the energy dissipation capacity of the *S-type* 2D PXCMs was higher than the *T-type* 2D PXCMs. Compare with the energy dissipation capacity of 1D PXCMs, under the indentation loading condition, 2D PXCMs show much higher energy dissipation capacity (Table 5.3). This observation is in coherence with the auxetic behavior of PXCMs. To demonstrate this correlation, the energy dissipation per unit volume and per unit mass were plotted against the approximated Poisson's ratio in Figure 5.17. It shows increasing the magnitude of negative Poisson's ratio leads to decreasing energy dissipation. This phenomenon can be explained by quantifying the number of building blocks which achieve phase transformation through a rotational mode.

Further study will be conducted in the future to understand this phenomenon. Understanding the advantages and disadvantages of the 1D and 2D PXCMs under different loading conditions can help discover further fields of application for these materials. Eventually, the advantages of both the 1D and 2D PXCMs could be considered for the design of new materials that could potentially harness the unique properties exhibited by both of these PXCMs.

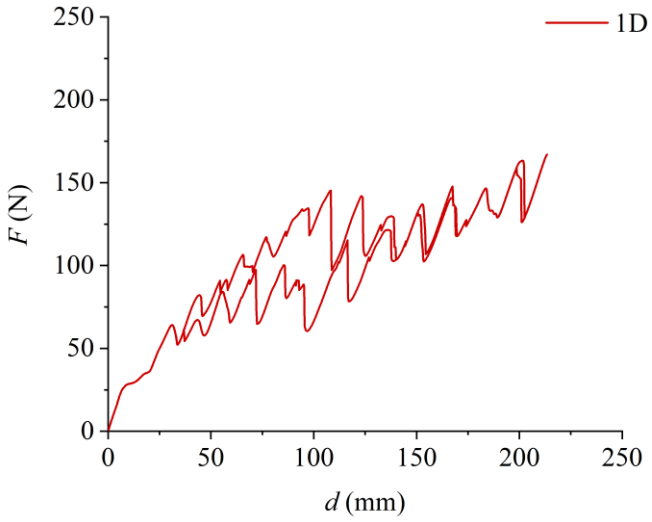

Figure 5.12: *F-d* relationship of 1D PXCM sample undergo indentation load along 0°.

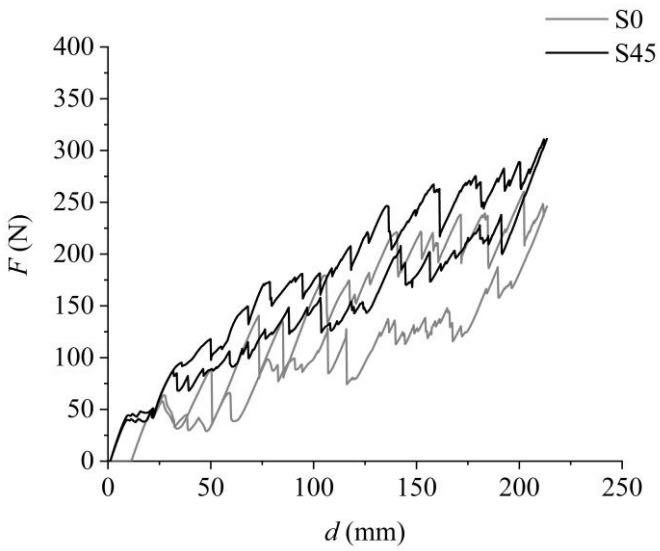

Figure 5.13: *F-d* relationship of *S-type* 2D PXCM samples undergo indentation load along 0° and 45°.

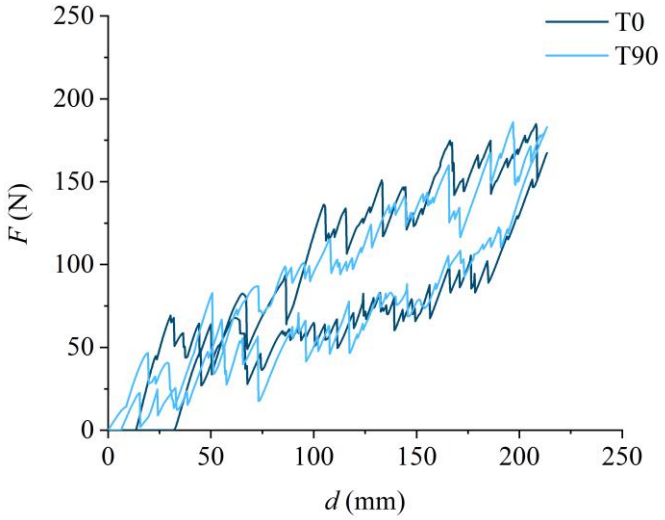

Figure 5.14: *F-d* relationship of *T-type* 2D PXCM samples undergo indentation load along 0° and 90°.

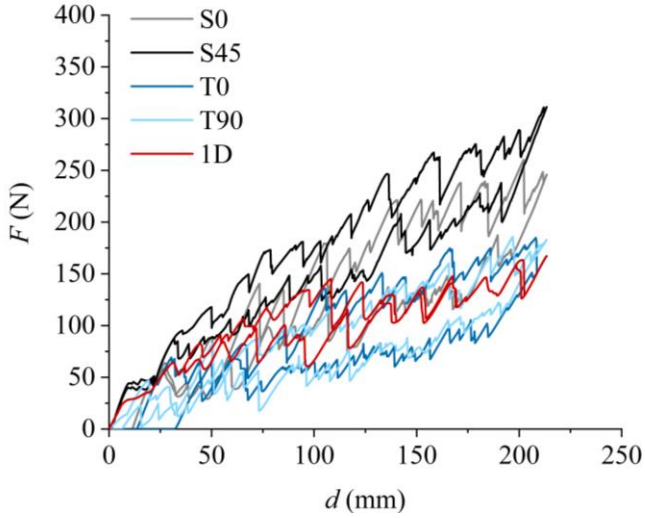

Figure 5.15: *F-d* relationship of 5 PXCM samples undergo the indentation.

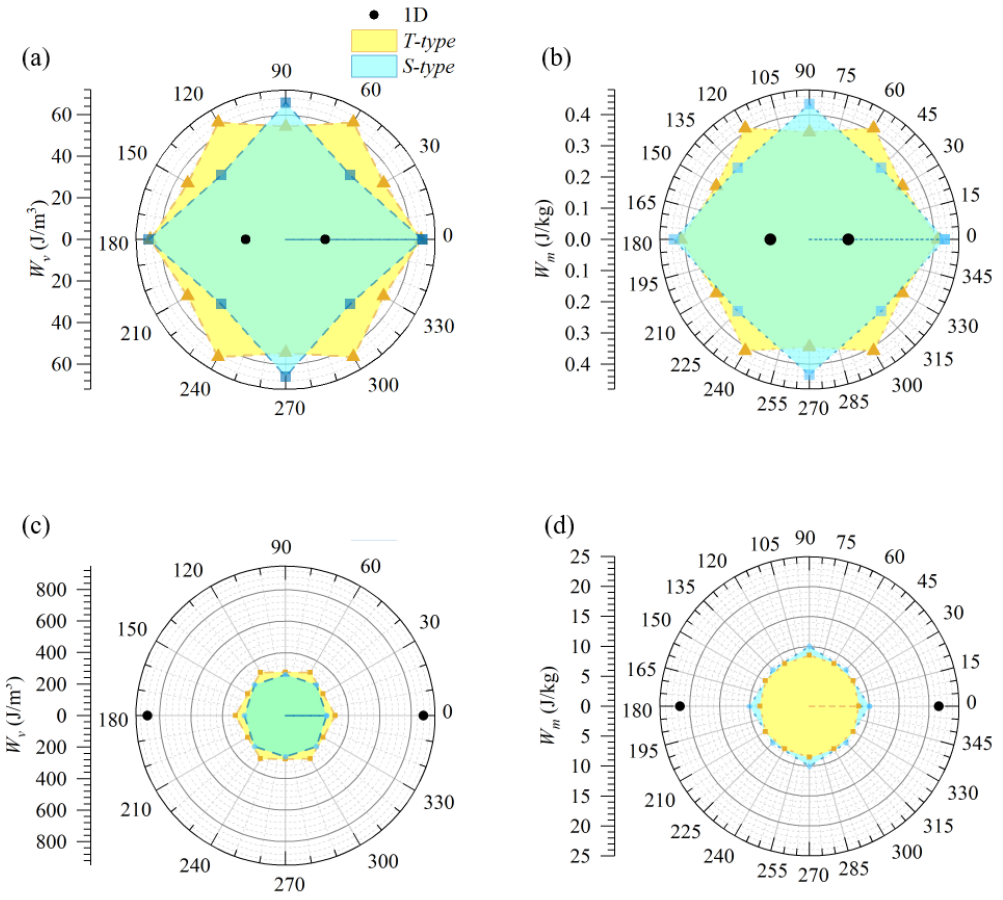

Figure 5.16: Energy dissipation per unit volume (W_v) and per unit mass (W_m) of 1D and 2D PXCMs undergo the concentrated and uniform loading conditions. (a) W_v under concentrated loading conditions. (b) W_m under concentrated loading conditions. (c) W_v under uniform loading conditions. (d) W_m per unit mass under uniform loading conditions.

Table 5.1: Specimen size for the indentation models.

Specimen Name	*W*	*H*	*b*	*V* (mm^3)	m (kg)
1D PXCM	2414	2386	25	143970960	22
S-type 0°	2376	2376	25	141134400	21
S-type 45°	2444	2444	25	149299073	20
T-type 0°	2296	2340	25	134329131	21
T-type 90°	2340	2296	25	134329131	21

Table 5.2: Phase transformation band spread in X and Y direction.

Specimen	*v*	***lx/W***	***ly/H***	***ly/lx***
1D PXCM	-0.02	0.88	0.12	0.13
S-type 0°	-0.01	0.81	0.32	0.39
S-type 45°	-0.8	0.50	0.52	1.03
T-type 0°	-0.17	0.70	0.30	0.43
T-type 90°	-0.28	0.54	0.31	0.57

Table 5.3: Energy dissipation per unit volume and per unit mass of each sample.

Specimen Name	W_v (J/m^3)	W_m (J/kg)
1D PXCM	19.2	0.13
S-type 0°	65.8	0.43
S-type 45°	43.9	0.41
T-type 0°	65.1	0.34
T-type 90°	54.3	0.33

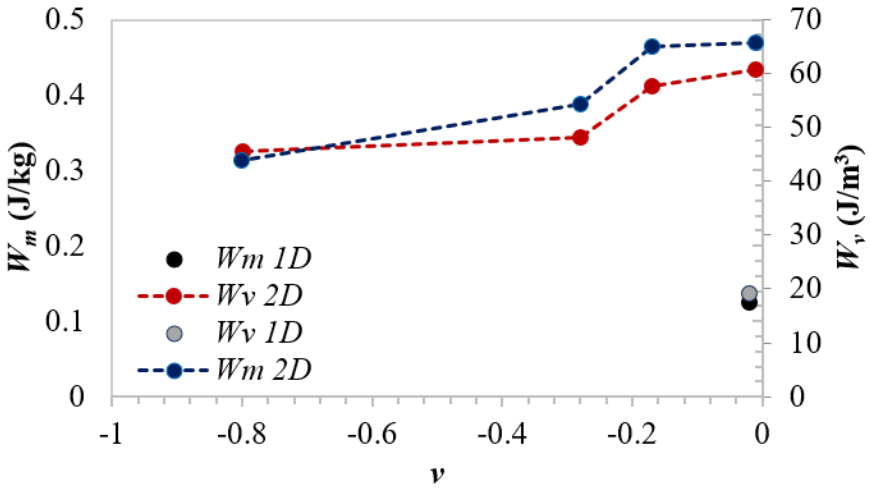

Figure 5.17: Energy dissipation varies with approximated Poisson's ratio.

6. SUMMARY AND CONCLUSIONS

This study presents a family of architected, phase-transforming cellular materials that can enable the properties of active and natural materials. The special properties of the materials were demonstrated using analytical, numerical, and experimental methods. The investigation began with 1D Phase Transforming Cellular Materials (PXCMs) and efforts to achieve shape-memory effect using temperature variation. A methodology was developed for controlling phase transformations by tailoring the geometry of a unit cell and by assigning multiple base materials with different thermomechanical properties to that cell. The next phase of the study involved coupling 1D PXCMs with linear elastic springs to create a system that can mimic shape- and strength-recovery similar to feathers. Having achieved shape-memory and shape-recovery effects, the next focus of this study was to use the superelasticity of 1D PXCMs to resist simulated seismic demands without sustaining damage. In collaboration with Prateek Shah and William Pollalis from Santiago Pujol's research group, a single-degree-of-freedom (SDOF) 1D PXCM system was tested in a dynamic environment on a unidirectional earthquake simulator. Lastly, the concept was extended into two dimensions through the creation of two types of 2D PXCMs.

The unit cells studied here consist of a sinusoidal beam with stiff walls at each end. The strain energy of a unit cell during the phase transformation is composed of the monotonic bending energy (SE_b) and the nonmonotonic axial energy (SE_a) due to the changing length of the sinusoidal beam. This combination of monotonic and nonmonotonic strain energy creates the second stable position of strain energy, resulting in a bistable unit cell. A bistable condition is one in which the unit cell remains in its second stable configuration after having undergone a phase transformation, whereas a metastable condition is one in which the unit cell snaps back to its original stable configuration. Here, the concepts of axial strain energy and bending energy were used to create a unit cell capable of transforming phases under temperature variations. This was done by increasing the compliance of a unit cell such that the impact of the nonmonotonic axial component, SE_a, decreases to the extent that the second stable position of strain energy disappears and an otherwise bistable mechanism becomes metastable. By altering its compliance, a PXCM unit cell can transform from its second stable configuration to its first stable configuration, as a result exhibiting the shape-memory effect. One way to tune the compliance of a unit cell is by inducing a temperature change.

To demonstrate this shape-memory effect, a procedure was developed which shows how to tune the phase transformation of 1D PXCMs by controlling the geometry and thermomechanical relationship between the stiff walls and the sinusoidal beams. By fabricating the sinusoidal beam with a material which is relatively insensitive to temperature change, and the stiff walls with a material which softens with increasing temperature, it was possible to achieve the shape-memory effect by temperature variation. Using this shape-memory effect, it was also shown that PXCMs can also be designed to do work through temperature variation. By increasing temperature, a PXCM unit cell can lift a weight which was applied at a colder temperature, provided the weight does not exceed the local minimum force (valley force) of its force-displacement relationship at the designed recovery temperature. To facilitate the creation of other PXCMs capable of these behaviors, a design guide was developed in Chapter 2 that demonstrates how to tailor the transformation stress and temperature of PXCMs. Most commercially-available additive materials used to fabricate PXCMs are polyjet materials. These materials show a decrease in elastic moduli with increasing temperature, a limitation which means the local minimum force a unit cell can exert at a high temperature cannot exceed the peak force at a low temperature. As a result of this limitation, PXCMs cannot conduct a complete working cycle like Shape Memory Alloys (SMAs). One proposed area of research in the future would be on eliminating this constraint using new materials.

By controlling the geometry of unit cells, PXCMs can reproduce the superelasticity of SMAs. This property creates the opportunity to enable the shape and strength recovery behavior of feathers. A feather shaft exhibits shape and strength recovery effects though the interplay between approximately elastic fibers which are insensitive to the moisture content variation and an elastic-plastic matrix which exhibits strength and stiffness reductions when the moisture content increases. Inspired by this coupling in nature, 1D PXCMs made from materials that are sensitive to temperature changes were coupled with linear springs which are insensitive to temperature, mimicking the matrix and fibers in feathers. This new system reproduced shape- and strength-recovery effects via changing temperature using finite element simulations.

Typical structures are designed to undergo material nonlinearity and to sustain damage during earthquakes. The superelasticity of PXCMs means that they have high potential for resisting

seismic demands without sustaining damage. Towards that, the behavior of PXCMs in a dynamic environment was studied through dynamic testing of a single-degree-of-freedom (SDOF) system with 1D PXCMs as the source of stiffness. This SDOF system was tested under five different ground motion records with eight different masses. The system exhibited global non-linear behavior without permanent deformation under seismic demands. Finite element simulations were also made for the most extreme cases (e.g., weakest and strongest ground motions for each mass). On average, the ratio of estimated peak displacement using finite element simulations to measured peak displacement was 1.17 with a coefficient of variation (CoV) of 22%. These values indicate that finite element analysis (FEA) can provide reasonable and conservative estimates of displacement demand for SDOF-PXCM systems. In summary, a PXCM is a suitable alternative or supplement to traditional materials because they can undergo global nonlinearity without experiencing permanent deformations.

The concept of a 1D PXCM was next extended to two-dimensions through the creation of square and triangular 2D PXCMs (*S*- and *T-type*). In contrast to 1D PXCMs, 2D PXCMs transformed phases under two or more loading directions. When loaded along multiple axes of symmetry, 2D PXCMs exhibited superelasticity, dissipating energy while remaining elastic. Experiments on 3D-printed prototypes, together with nonlinear finite element simulations, were used to examine and understand the mechanical behavior of these PXCMs. The results from experiments and finite element simulations showed that the energy dissipation capacity of both 2D PXCM designs did not vary by more than 12% with the direction of loading, even though the energy dissipation of a single bistable mechanism typically reduces rapidly when the loading angle moves away from its axis of symmetry. This behavior can be attributed to the unit cells reorientating to align their primary axes of symmetry with the loading directions. This new class of PXCM offers a myriad of opportunities for developing applications such as reusable solid state energy absorption, shock or impact isolation, and reconfigurable structures. Finite element simulations and experiments on these 2D PXCMs revealed that both designs exhibited auxetic behavior (i.e., a negative Poisson's ratio in which the material contracts under compression). *S-type* samples had a Poisson's ratio in the range of -1 to 0, whereas *T-type* samples had Poisson's ratio in the range -1.1 to -0.29. This auxetic behavior indicates that 2D PXCMs may have additional mechanical advantages, such as high indentation resistance, shear modulus, fracture toughness, and synclasticity. The analysis of

the response of this new class of PXCMs to more complex loading conditions such as bi-axial loading, bending, and indentation is the focus of ongoing work.

This investigation shows how architected materials with PXCMs as the unit cell can be tailored to achieve the advantageous properties of active and natural materials, including superelasticity, shape-memory, and shape recovery. The underlying approach for mimicking the constitutive response of active materials by controlling the geometry, topology, and constituent materials at smaller-scale is demonstrated via two cases. In the first case, the complex thermo-mechanical response of a type of active materials – metallic alloy (Ni-Ti) – is reproduced. In the second case, an organic material with a complex chemo-mechanical response is studied and then mimicked using a system including architected materials. These cases demonstrate the usefulness of PXCMs in achieving special behavior, as well as the potential for coupling them with conventional materials to realize a broader range of special and useful behaviors. These examples also demonstrate that it is possible to engineer an architected material that can mimic a natural material, and by extension, improve on these materials based on specific applications.

APPENDIX A

A1. Analytical model for *Type I* PXCM

PXCMs consist of numerous periodically arranged bistable or metastable building blocks. Each building block comprises a sinusoidal beam and stiff walls as supports. PXCMs made of a single material (1D PXCMs), have adjacent building blocks provide each other translational and rotational constraints. As a result, the bistability of a building block is controlled by the geometry of the sinusoidal beams[19,38,39]. With sufficient constraints, each building block can be modeled as a sinusoidal beam under the clamped-clamped boundary condition and with a load applied to its apex (Figure A1). For the PXCMs made of two materials, the bistability not only depends on the geometry of the building blocks but also the material combination. When $T>T_t$, the stiff walls cannot provide sufficient constraint to keep a building block bistable, even if the geometry of a sinusoidal beam satisfies the condition (Q>2.31). Here, we develop *Type I* PXCMs can exhibit phase transformation by changing the stiffness of the stiff walls. The current analytical models can predict the force-displacement relationship of the PXCMs made of a single material but not the *Type I* PXCMs made of dual materials.

A1.1 PXCMs-Spring model

Analytical models are the critical tools to design P- PXCMs to achieve shape recovery effect at a certain temperature. The analytical models Qiu's derived[38,39] describes the snap-through behavior of a sinusoidal beam under the clamped-clamped boundary condition (Figure A1) has been widely used to predict the mechanical behaviors of snapping metamaterials[19,58,59]. But this model cannot capture the mechanical response of *Type I* PXCMs, because the boundary conditions of a building block vary with temperature. In a PXCMs building block, the stiffness of stiff walls reduces when the temperature increases, but the stiffness of the sinusoidal beam does not change as much. Here, a new analytical model is created to predict the mechanical behavior of PXCMs. This new model simplifies a building block into a sinusoidal beam series connected to a spring under the clamped-clamped boundary conditions as shown in Figure A1b.

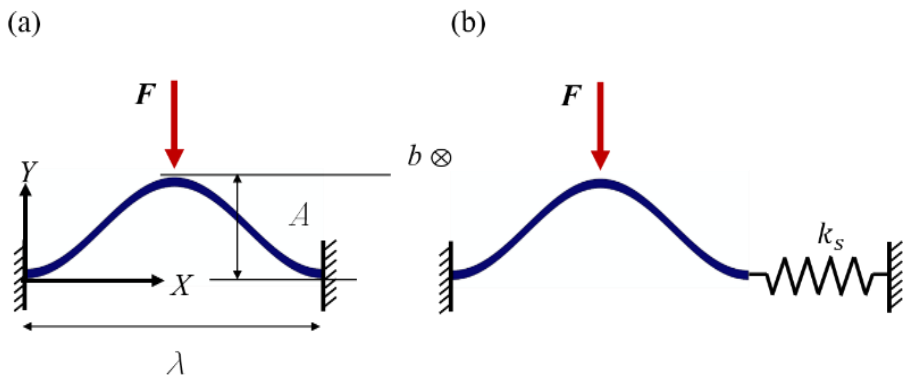

Figure A1:PXCMs building block

The sinusoidal beam is designed in shape of the first buckling mode shape as A.1 shown below. The wavelength of the sinusoidal beam is λ, the thickness of the beam is t, the out of the plane thickness of bam is b, and the amplitude is A.

$$\overline{w}(x) = \frac{A}{2}[1 - cos(2\pi\frac{x}{\lambda})] \quad \text{(A. 1)}$$

A critical nondimensional parameter Q is defined as below to describe the bistability of the building block.

$$Q = A/t \quad \text{(A. 2)}$$

When a force F applies to the midpoint of the sinusoidal beam, the deflection at loading point ($X=\lambda/2$) can be described as,

$$d = \overline{w}(\frac{\lambda}{2}) - w(\frac{\lambda}{2}) \quad \text{(A. 3)}$$

During the process of a building block transforms from phase 1 (P_1) into phase 2 (P_2), three types of energy, bending energy u_b, compression energy u_s, and actuation energy u_f involve in the system. The variation of the bending energy inside the sinusoidal beam is shown below.

$$\partial(u_b) = \partial[\frac{EI}{2}\int_0^{\lambda}(\frac{d^2\bar{w}}{dx^2} - \frac{d^2w}{dx^2})^2 dx] \quad \text{(A. 4)}$$

The variation of the compression energy which comes from beam and spring is shown in A.3, where p represents the axial force caused by the deformation of both sinusoidal beam and spring

along the axial of the beam, s_o and s represent the initial and final length of the beam. Here k_a and k_s represent the axial stiffness provided by sinusoidal beam and spring correspondingly.

$$\partial(u_s) = -p\partial(s) \tag{A. 5}$$

$$p = \left(\frac{k_a k_s}{k_a + k_s}\right)(s_o - s) = \left(\frac{k_a}{\frac{k_a}{k_s} + 1}\right)(s_o - s)$$

$$= ck_a(s_o - s)$$

Where (A. 6)

$$s = \int_0^{\lambda} \sqrt{1 + (\frac{dw}{dx})^2}\, d \approx \int_0^{\lambda} [1 + \frac{1}{2}(\frac{dw}{dx})^2] dx$$

$$k_a = \frac{Ebt}{\lambda}$$

$$c = \frac{1}{k_a/k_s + 1}$$

A dimensionless parameter *c* is defined to describe the stiffness of spring relative to the stiffness of the sinusoidal beam. Stiffer the spring, larger the value of k_s. When $k_s \to \infty, c \to 1$, and the system is equivalent to a sinusoidal beam under the clamped-clamped boundary condition. When $k_s \to 0, c \to 0$, the system equivalent to the sinusoidal beam under the free boundary condition (Figure A2). The value *c* of a PXCM unit cell varies with the stiffness of stiff walls is shown in section A6.

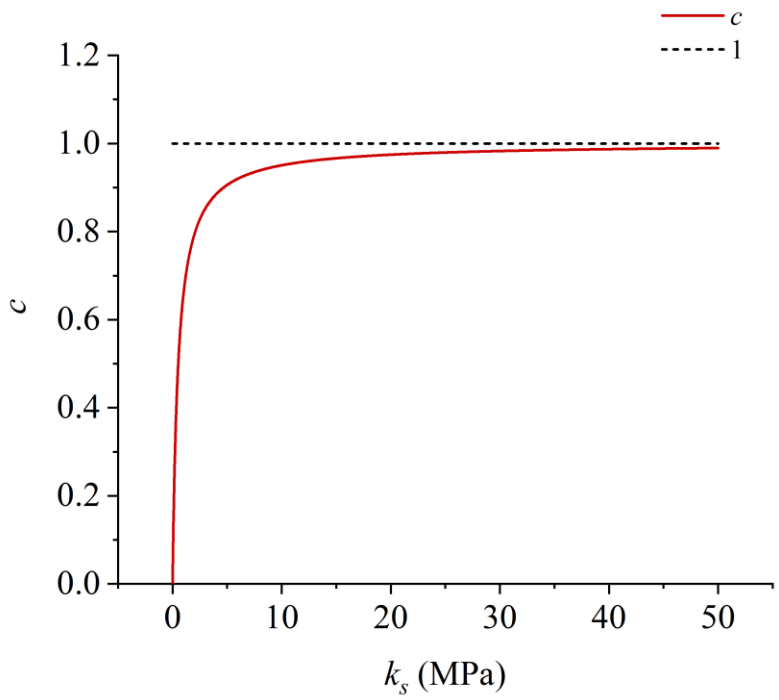

Figure A2: $c \rightarrow 1$ when k_s increases.

The variation of actuation energy is shown in where F and d represent actuation force and displacement.

$$\partial(u_f) = -F\partial(d) \tag{A. 7}$$

During the phase transformation, the deflection of a sinusoidal beam can be assumed as a superposition result of the buckling modes. We normalize the parameters as follow:

$$X = \frac{x}{\lambda} \tag{A. 8}$$

$$W(X) = \frac{w(X\lambda)}{A} = \sum_{j=1}^{\infty} A_j W_j(X) \tag{A. 9}$$

Where,

$$\begin{aligned} W_j(X) &= 1 - cos(N_j X) \\ N_j &= (j+1)\pi \\ j &= 1,3,5 \end{aligned} \tag{A. 10}$$

$$W_j(x) = 1 - 2X - cos(N_jX) + \frac{2\,sin(N_jX)}{N_j}]$$

$$N_j = 2.86\pi, 4.92\pi \ldots \quad \text{(A. 11)}$$

$$j = 2,4,6$$

The normalized beam shape is

$$\overline{W}(X) = \frac{1}{2}W_1(X) \quad \text{(A. 12)}$$

Normalize other parameters as A.13 shown below.

$$f = \frac{F\lambda^3}{EIA}, \delta = \frac{d}{A}, S = \frac{s\lambda}{A^2}, N^2 = \frac{pl^2}{EI}$$

$$U_b = \frac{u_b\lambda^3}{EIA^2}, U_s = \frac{u_s\lambda^3}{EIA^2}, U_f = \frac{u_f\lambda^3}{EIA^2} \quad \text{(A. 13)}$$

Express all the parameters through these dimensionless parameters, Equations A3-A7 can be expressed as below:

$$\delta = 1 - 2\sum_{j=1,5,9,13\ldots}^{n} A_j \quad \text{(A. 14)}$$

$$S = 1 + 2\sum_{j=1,5,9,13\ldots}^{n} \frac{{A_j}^2 {N_j}^2}{4} \quad \text{(A. 15)}$$

$$\frac{N^2}{12Q^2c} = (S)_{w=\bar{w}} - S = \frac{N_1^2}{16} - \sum_{j=1}^{\infty} \frac{{A_j}^2 {N_j}^4}{4} \quad \text{(A. 16)}$$

$$\partial(U_b) = \partial[\frac{(\frac{1}{2} - A_1)^2 {N_1}^4}{4} + \sum_{j=2}^{\infty} \frac{{A_j}^2 {N_j}^4}{4}] \quad \text{(A. 17)}$$

$$\partial(U_s) = -N^2\partial[\sum_{j=2}^{\infty} \frac{{A_j}^2 {N_j}^4}{4}] \quad \text{(A. 18)}$$

$$\partial(U_f) = 2F\sum_{j=1,5,9,`3}^{\infty} A_j \quad \text{(A. 19)}$$

$$\partial(U_t) = \partial[(\frac{N_1^4(A_1^2 - A_1)}{4} - \frac{cN^2A_1^2N_1^2}{4} + 2FA_1) + (\sum_{j=2}^{\infty}\frac{A_j^2N_j^4}{4} - \sum_{j=2}^{\infty}\frac{cN^2A_j^2N_j^4}{4} + 2F\sum_{j=5,9,13\ldots}^{\infty}A_j)] \quad \text{(A. 20)}$$

To satisfy the condition $\partial(U_t) \geq 0$, eventually there are three types of solutions of the applied force can induce phase transformation which are expressed as below.

$$f_1 = \sum_{j=1,5,9,13\ldots}^{\infty}\frac{4(N^2 - N_1^2)}{N_j^2(N^2 - N_j^2)^2}{F_1}^2 - N_1^2F_1 + \frac{N^2(N^2 - N_1^2)^2}{12Q^2c} - \frac{N_1^2N^2(N^2 - 2N_1^2)}{16} = 0$$

$$f_2 = \frac{1}{\sum_{j=1,5,9,13\ldots}^{\infty}\frac{8}{N_j^2({N_2}^2 - N_j^2)^2}}(\frac{N_2^2}{N_2^2 - N_1^2} - \delta) \quad \text{(A. 21)}$$

$$f_3 = \frac{1}{\sum_{j=1,5,9,13\ldots}^{\infty}\frac{8}{N_j^2({N_3}^2 - N_j^2)^2}}(\frac{N_3^2}{N_3^2 - N_1^2} - \delta)$$

f_1, f_2, and f_3 represent the normalized applied force while a building block going through the three primary modes, *mode 1*, *mode 2*, and *mode 3* (Figure A3).

Here, we illustrate the analytical model on a building block with the geometry details: t=0.7mm, A=7 mm, Q=7, and $E = 2\ GPa$. The relationship of F_1, F_2, and F_3- δ of this building block transforms from P_1 to P_2 are plotted in Figure A3. During the phase transformation, this building block goes through three primary buckling modes, *mode 1, mode 2, and mode 3* (Figure A3). At the beginning and end of phase transformation, the axial force *p* is small, and the building block transforms through *mode 1*. Once *p* increases to the threshold of *mode 2* or *mode 3*, the building block switches to *mode 2* or *mode 3* which depends on whether the rotational motion at the middle of the sinusoidal beam is constrained. Toward the end of phase transformation, *p* reduces to the threshold of *mode 1* again. As a result, the building block switches back to *mode 1*. The F-δ relationship of this sinusoidal beam going through these three modes is denoted by F_1-δ, F_2-δ and F_3-δ. Here, F_1 intersects with F_2 and F_3 twice. The intersection between F_1- δ, F_2- δ and F_3- δ is

where the sinusoidal beam switches from *mode 1* to *mode 2* or *mode 3*. The F- δ relationship is the combination of f_1-d outside two points of intersection and F_2- δ or F_3- δ between the two points of intersection.

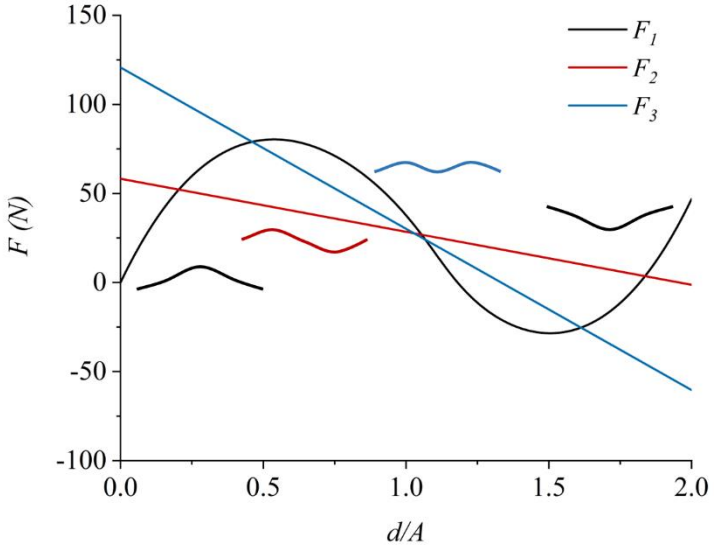

Figure A3: *F*-*d* relation of three primary modes.

A1.2 Results and Conclusions of Analytical Equations

To evaluate the accuracy of the analytical equations, the FE simulations of a PXCMs building block and its simplified sinusoidal beam and spring model undergo the stress-induced phase transformation are created for comparison. The spring of this simplified model has equivalent stiffness of the stiff walls from the building block provide to the sinusoidal beam. This study was conducted on various building blocks which have λ=0.7mm, A=7 mm, but different geometric parameter Q, where Q=2,3,7, and 8. All of the FE simulations were created in Abaqus 6.15, using Timoshenko beam elements with linear interpolation, B21. The base material properties assigned to the simulations come from a polymer material known as ABS-M30 ($E \approx 2\ GPa$, $\sigma_y \approx 40\ MPa$).

The comparison of *F*-*d* relationships obtained from FE and analytical models (Figure A4). The minor differences between the results obtained from FE-simulations and analytical models are

observed. It indicates that the analytical equations are reasonable tools to predict the mechanical response of the 1D PXCM building block.

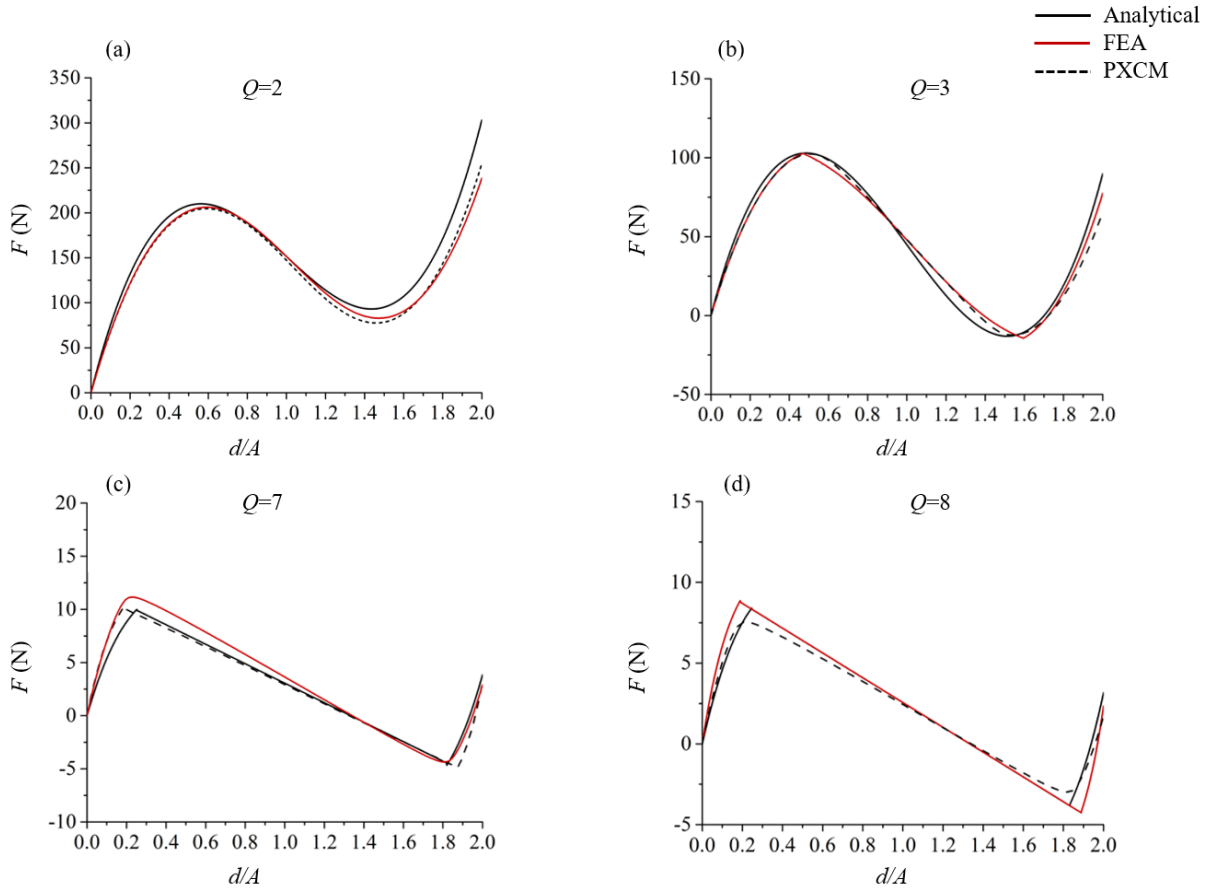

Figure A4: Comparison between analytical equation and simulation.

A2. Dimensional analysis

For the PXCMs, we assume two base materials -m_1 and m_2-, temperature, and geometry of an elementary building block determining the bistability of the PXCMs. Dimensional analysis was conducted to find the choice of appropriate dimensional groups.

Firstly, we are looking at the input variables, and then defining the output variables that can capture the overall response of a PXCMs building block.

The input variables were selected from the variables in A 21. Then, the geometrical variables of interest are: { $t, A, \lambda, b, t, E_1, E_2$ }. They all have dimensions of length [l]. The material properties variables of interest are: { E_1, E_2 }. They all have dimensions of force per length square [Fl^{-2}].

The model is of the form

$$f(L, F) = 0 \tag{A. 22}$$

In this analysis, there two fundamental physical units ($k = 2$): Force [F], and length [l], and there are 7 dimensional variables { $t, A, \lambda, b, t_s, E_1, E_2$ }. Therefore, the equation relates to all the variables which have 7-2=5 dimensionless parameter denoted π.

$$f(\pi) = 0 \tag{A. 23}$$

Where π is given by

$$\pi = t^{m1}, A^{m2}, \lambda^{m3}, b^{m4}, {t_s}^{m5}, {E_1}^{m6}, {E_2}^{m7} \tag{A. 24}$$

$$\pi = [L^{m1}][L^{m2}][L^{m3}][L^{m4}][L^{m5}][F^{m6}][L^{-2m6}][F^{m7}][L^{-2m7}] \tag{A. 25}$$

To ensure π to be dimensionless, then the following should be satisfied.

$$[L]^{m1+m2+m3+m4+m5-2m6-2m7} = 1 \tag{A. 26}$$

$$[F]^{m6+m7} = 1 \tag{A. 27}$$

Or

$$m1 + m2 + m3 + m4 + m5 - 2m6 - 2m7 = 0 \tag{A. 28}$$

$$m7 + m8 = 0 \tag{A. 29}$$

The dimensional matrix is

$$\begin{bmatrix} 1 & 1 & 1 & 1 & 1 & -2 & -2 \\ 0 & 0 & 0 & 0 & 0 & 1 & 1 \end{bmatrix} \tag{A. 30}$$

The nondimensional π groups presented as shown below. These π groups are independent to each other and no group is the combination of the other groups.

$$\pi_1 = \frac{t}{\lambda} = [1\ 0 - 1\ 0\ 0\ 0\ 0]$$

$$\pi_2 = \frac{A}{\lambda} = [0\ 1\ -1\ 0\ 0\ 0\ 0]$$

$$\pi_3 = \frac{t_s}{\lambda} = [0\ 0\ -1\ 0\ 1\ 0\ 0] \quad \text{(A. 31)}$$

$$\pi_4 = \frac{E_2}{E_1} = [0\ 0\ 0\ 0\ 0\ -1\ 1]$$

$$\pi_5 = \frac{b}{t} = [-1\ 0\ 0\ 1\ 0\ 0\ 0]$$

In this study, *b* always set up to be 25 mm, therefore, only four nondimensional parameters, $\pi_1, \pi_2, \pi_3, and\ \pi_4$ are studied for the design process. In summary, $\pi_1 = \frac{t}{\lambda}$, $\pi_2 = \frac{A}{\lambda}$, $\pi_3 = \frac{t_s}{\lambda}$, and $\pi_4 = \frac{E_2}{E_1}$ are considered as the non-dimensional design parameters to tailor the bistability of the materials.

A3. Phase Transformation Diagram

In this section, we use FE simulations to demonstrate how to trigger the temperature-induced phase transformation on a building block. The geometry of this building block is shown in Table A.1. Here m_1 is DM_8530, which is assigned on the sinusoidal beam and m_2 is DM_9895, which is assigned on the stiff walls. Figure A5 shows how Elastic modulus of m_1 and m_2 varies with temperature. The building block was modeled using nonlinear finite element analysis in commercial finite element package ABAQUS 6.18. It was modeled by four-node bilinear quadrilateral plane-strain element with reduced integration (CPE4R). This building block underwent the stress-induced phase transformation at different temperatures. Rollers were used to constrain the bottom of the stiff wall to prevent the displacement in *Y* direction. The two sides of the stiff walls were constrained to move in *X* direction. A force *F* applies on top of the building block. It transformed the building block from phase 1 (P_1) to phase 2 (P_2) at different temperatures. The stress and strain ($\sigma - \varepsilon$) relationship were obtained to study the bistability of the building block at different temperatures (see Figure 2a). Here, σ is *F* divided by gross cross-section area and ε is *d* divided by the original height of the building block. The bistability of a building block

is described by $r_b = -F_v / F_p = -\sigma_v / \sigma_p$. Knowing these relationships, σ_v, σ_p, and r_b can be obtained. The parameter c corresponding to different temperatures was calculated through Equation A.6. σ_v, σ_p, r_b, and c varies with temperature and are summarized in Table A 2 and plotted in Figure A6 and Figure A7.

In a PXCMs building block, the stiffness that stiff walls provide to the sinusoidal beam is determined by the parameter c. A bistable building block can become metastable if c decreases below a critical value. As A.6 shown, for a PXCMs building block with known geometry, c depends on the materials combination which is controlled by the nondimensional parameter $\pi_4 = \frac{E_2}{E_1}$. Bistability of this building block decreases with c, which depends on temperature. Hotter temperatures decrease c and r_b, therefore decreasing bistability (see Figure A6 -Figure A7). When the temperature decreases to 25℃, c=0.14 and r_b<0, the building block switches from bistable to metastable ($\sigma_v \geq 0$ and $r_b \leq 0$). Therefore, the transition temperature T_t of the building block is 25℃ and c_{cr} is 0.14. Subsequently, without any external mechanical loading, the building block can transform from BP_2 to MP_1 simply by heating to T_h such that c>0.14.

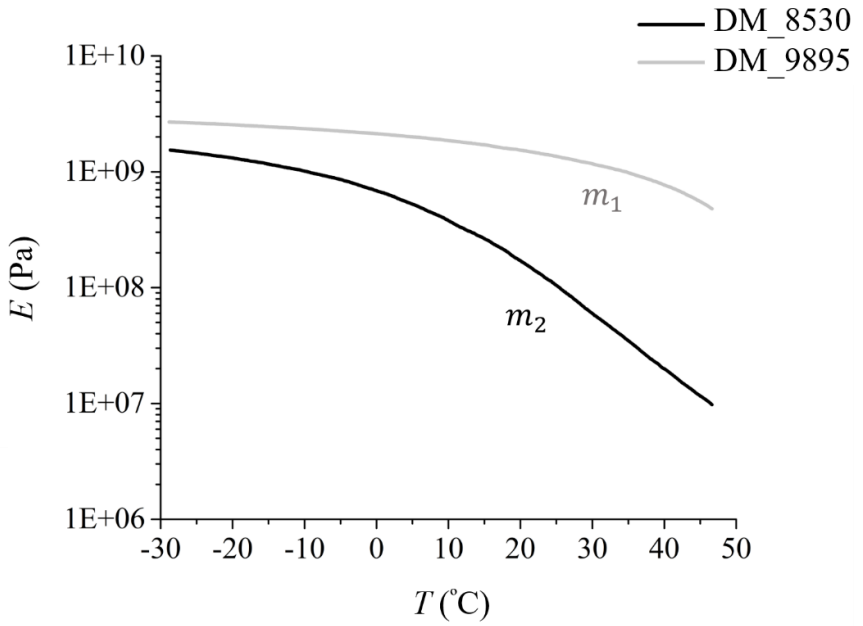

Figure A5: Elastic modulus of m1 and m2 varies with temperature.

Table A 1: Geometry details of the building blocks

Parameter	Dimension (mm)
t	0.7
A	4.5
λ	60
b	25
t_s	22

Table A 2: Peak stress, valley stress, the elastic modulus of m_1 and m_2, c, and r_b varies with temperature.

Temperature	5 ºC	10 ºC	15 ºC	20 ºC	25 ºC	30 ºC	35 ºC	40 ºC	45 ºC
σ_p *(MPa)*	0.007	0.006	0.005	0.004	0.003	0.002	0.001	0.001	0.001
σ_v *(MPa)*	0.0018	0.0011	0.0005	0.00014	0.00058	0.00085	0.00089	0.00078	0.00059
E_1 *(MPa)*	2002	1859	1710	1538	1358	1174	983	769	350
E_2 *(MPa)*	526	378	264	171	105	60	35	20	6
c	0.24	0.19	0.15	0.12	0.08	0.06	0.04	0.03	0.02
r_b	0.25	0.18	0.10	-0.04	-0.23	-0.47	-0.66	-0.73	-0.76

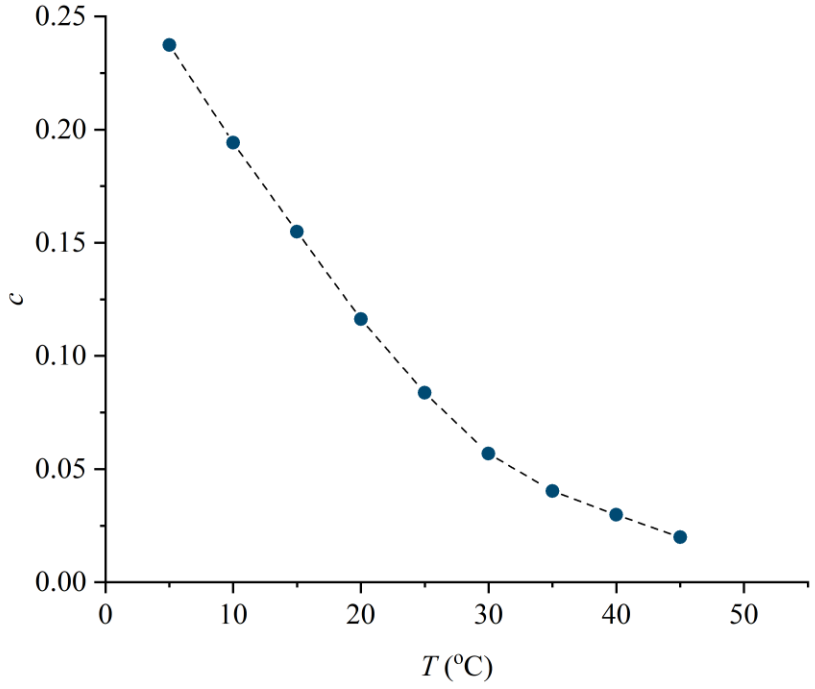

Figure A6: When the temperature increases, the stiffness provided by stiff walls decreases, therefore c decreases.

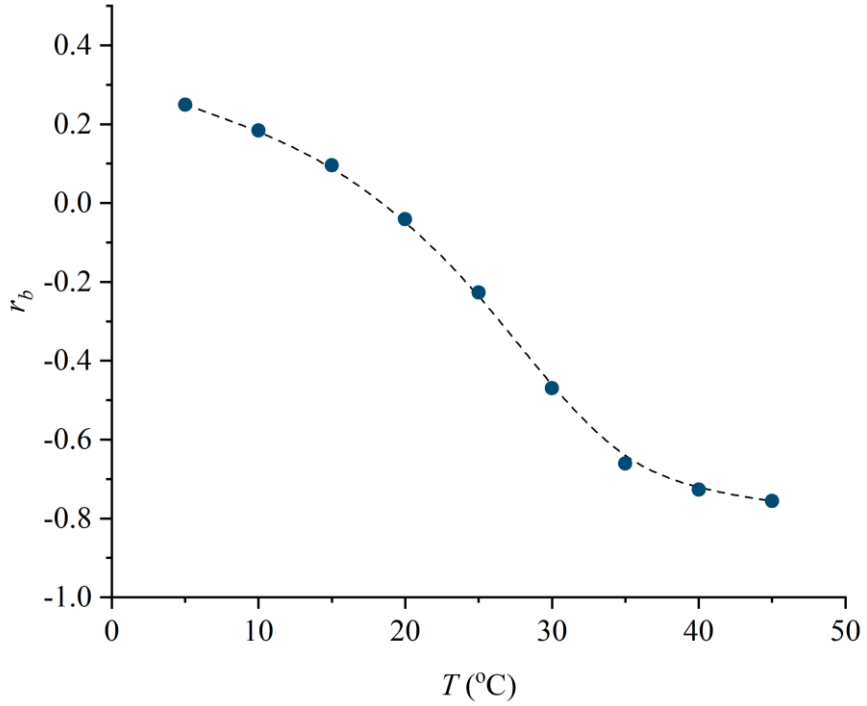

Figure A7: Bistability (r_b) of the building block decreases when the temperature increases.

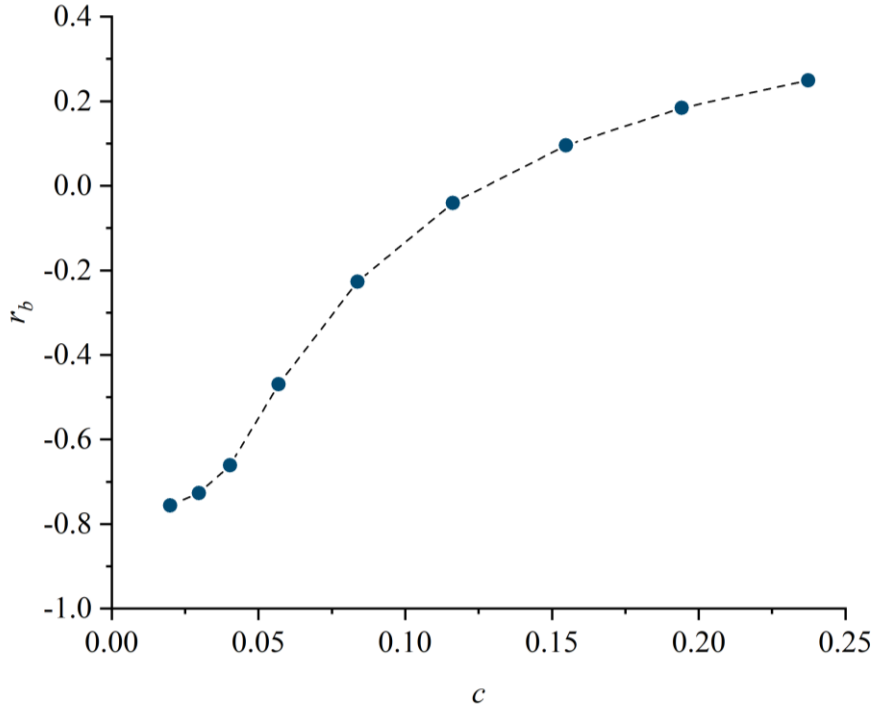

Figure A8: Bistability r_b varies with c.

There is a limitation on T_h. If temperature continues to increase, eventually $\sigma_v \approx \sigma_p$ and $r_b \rightarrow -1$. As a result, the negative stiffness regime 2 starts to disappear along with distinct phases. Figure 2.2b, a phase diagram, illustrates this phenomenon. Each point represents σ_v or σ_p of the building block shown in Figure 2.2b and Table A 2 at the corresponding temperatures. At low temperatures, the building block is bistable and it can transform from BP_1 to BP_2 via an external force which causes stress to exceed σ_p (Figure A9). The building block can also return to BP_2 when the external force causes stress lower than σ_v. At high temperatures, the building block is metastable. When stress reaches σ_p, it transforms from MP_1 to MP_2. Once the stress decreases below σ_v, the block can return to metastable state MP_1 (Figure A10). If the temperature is too high, σ_p and σ_v become too close to distinguish. As a result, phase transformation cannot occur.

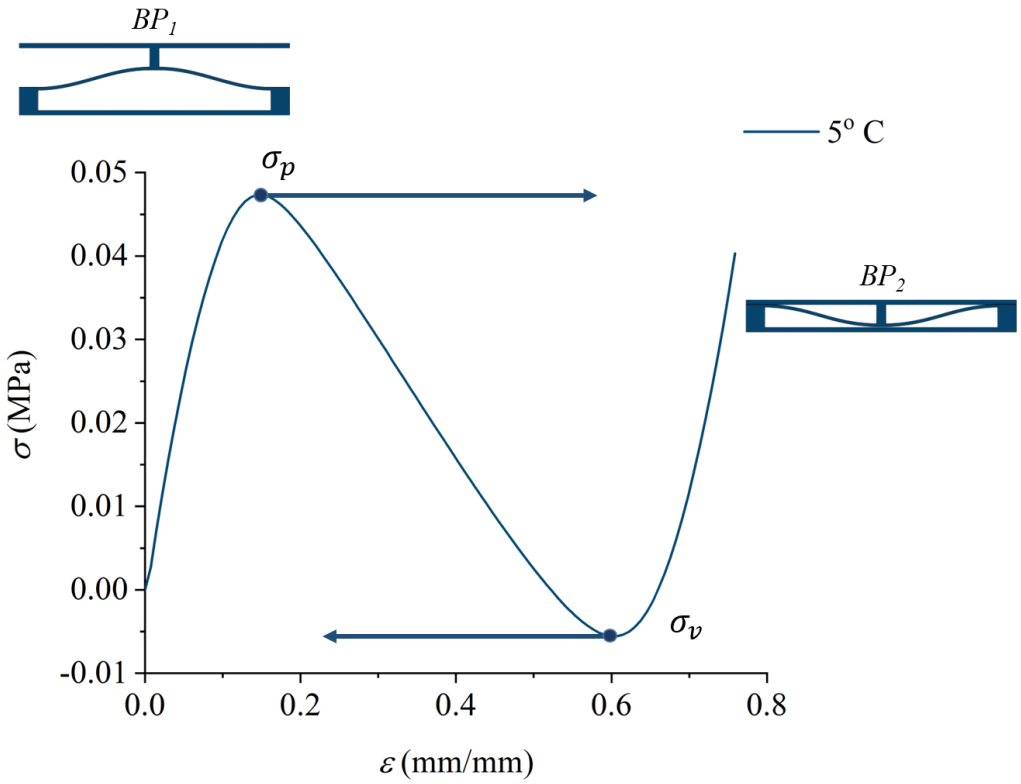

Figure A9: Phase transformation of a bistable building block.

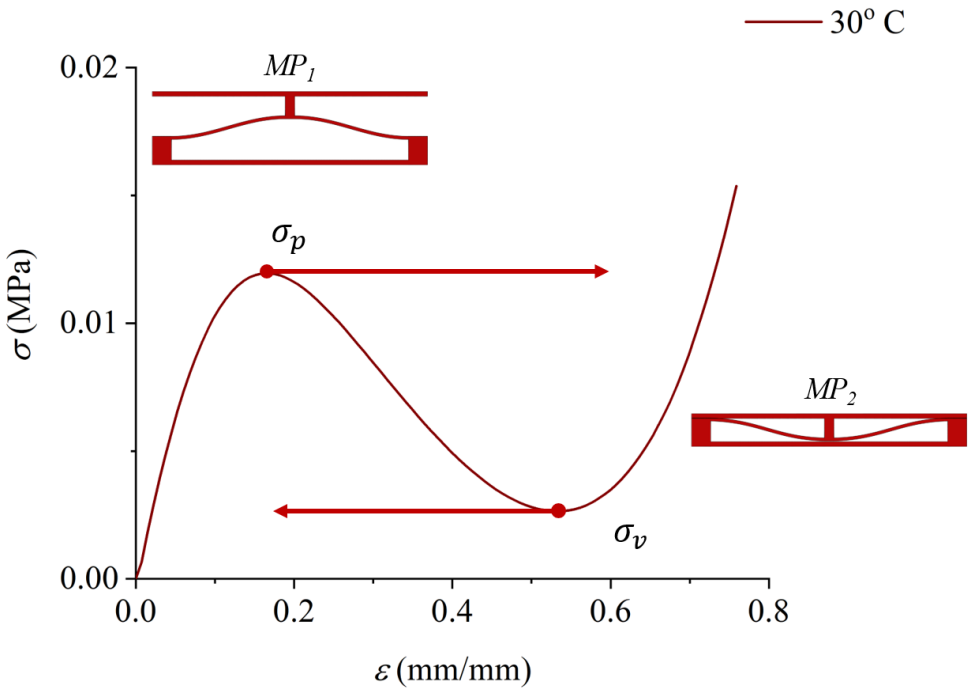

Figure A10: Phase transformation of a metastable building block.

A4. Design Concept

The bistability of a PXCM building block is determined by the nondimensional parameters Q and c. When $T \ll T_t$, $c \rightarrow 1$, therefore, Q is the parameter determining the bistability of the building block. When the temperature is not low enough, c becomes the key factor to determine the bistability of the building block. In this scenario, a bistable building block can switch from bistable into metastable when c reaches a critical value. Here we define this critical value of c as the parameter c_{cr}. When a building block with the geometry and material conditions satisfy $c = c_{cr}$, the F-d relationship of this building block also satisfies the condition $F_v=0$. When $c > c_{cr}$, $F_v < 0$, a building block is bistable, when $c < c_{cr}$, $F_v > 0$, a building block is metastable.

Regardless of the geometry or base materials of a building block, once the parameter Q of a building block is determined, there is a unique c_{cr} correspondingly. Any PXCMs building blocks with the same Q has the same c_{cr} value which captures the transition from bistable to metastable. There are infinite types of combination of materials and geometry can share the same c_{cr}

corresponding to the same Q. The c_{cr} corresponding to different Q is calculated based on A.21. Using this equation, c value corresponding to the F-d relationship shows F_v =0 can be found and defined as c_{cr}. A series of FEA models were created to support this concept. Figure A11 illustrates the F-d relationships of PXCMs building blocks have Q=*4* and c_{cr}=0.33 but different wavelength and amplitude combinations. It's observed that the F_v values of all the curves are approximately zero. It indicates that although these building blocks have these different geometric parameters combination if parameters Q are identical, c_{cr} are also identical.

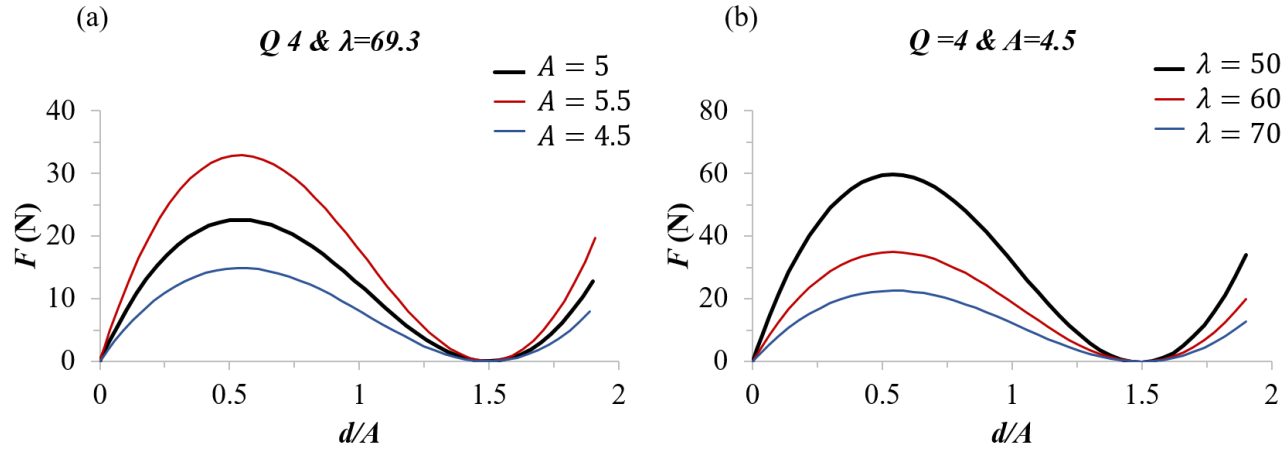

Figure A11: F-d relationships of PXCMs building block with same Q and c_{cr}. (a) Q=4, $\boldsymbol{\lambda}$=69.3mm, and A varies form 4.5 mm to 5 mm. (b) Q=4, $\boldsymbol{A}$=4.5 mm, and $\boldsymbol{\lambda}$ varies form 50 mm to 70 mm.

To evaluate the analytical equations for c_{cr}, A series of FE models were also created to evaluate the analytical models. FEA and analytical models are used to obtain the c_{cr} corresponding to different Q. They are plotted together in Figure A12 and show agreement. The comparison between FE simulations and analytical equations are summarized in Figure A12 and Table A3. c_{cr} obtained from two methods exhibit minor differences.

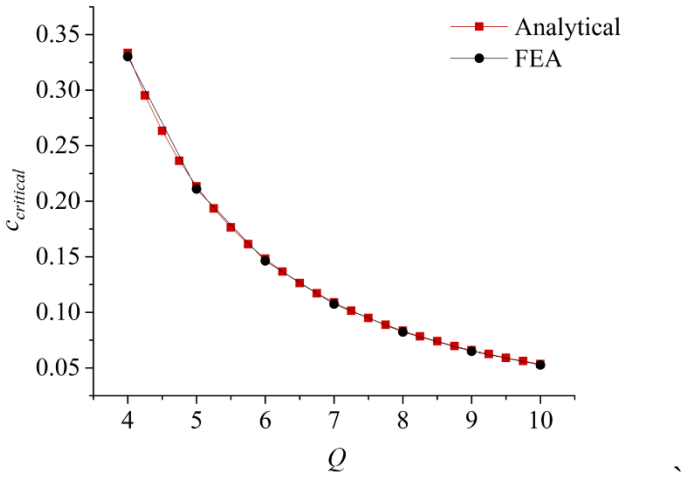

Figure A12: c_{cr} corresponding to various Q obtained by analytical equations and FE models.

Table A 3: c_{cr} corresponding to different Q.

Q	$c_{Analytical}$	c_{fea}	Error
4	0.3334	0.3302	0.9%
5	0.2134	0.2109	1.1%
6	0.1482	0.1463	1.2%
7	0.1089	0.1074	1.3%
8	0.0834	0.0822	1.4%
9	0.0659	0.0640	1.4%
10	0.0534	0.0526	1.5%

Design a building block with the geometric combination satisfies c=c_{cr} at a certain temperature is the key to trigger the phase transformation of PXCMs at the desired temperature. Here, we provide methods to create design maps for PXCMs. In this design map, all the building blocks are made of DM_8530 as m_1, and DM_9895 as m_2, whose elastic modulus varies with temperature as shown in Figure A5. The design map is shown in Figure A13, where $\pi_3 = 0.02$ is fixed and A=3 mm has been selected because they are the important factors determining the size of PXCMs. Each curve illustrates the transition temperature, T_t, of building blocks with a constant $\pi_2 = \frac{A}{\lambda}$ but different Q. For smaller values of π_2, higher temperatures are required to achieve phase

transformation. When π_2 is constant and Q is large, the PXCM becomes more bistable, and higher temperatures are required to transform it from BP_2 to MP_1. Compare with the design map where $\boldsymbol{\pi_2}$ varies via fixing $\boldsymbol{\lambda}$ and changing A, T_t is more sensitive to the to $\boldsymbol{\pi_2}$ via changing A and fixing $\boldsymbol{\lambda}$.

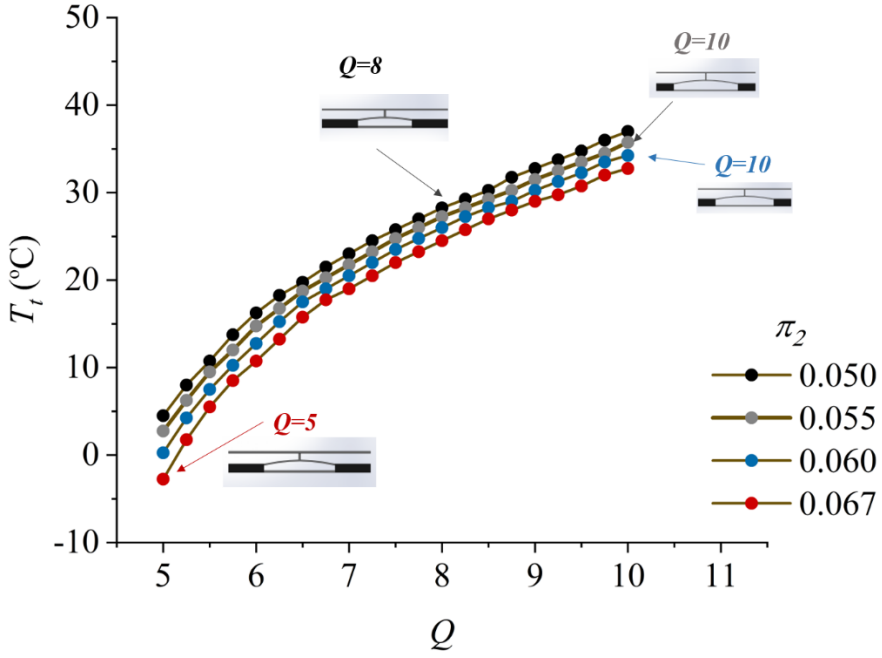

Figure A13: Design diagram illustrates the T_t of different PXCM building block with different geometry parameters.

A5. FEA validation

To show how to design PXCMs to exhibit shape-memory effect (SME), a PXCM sample is designed and tested in FE simulation. This sample consists of three building blocks made of DM_8530 (m_1) and DM_9895 (m_2), programmed to transform from BP_2 to MP_1 at T_t=18 °C. FE model is shown in Figure 2f. We design the recovery temperature of this specimen is 18 °C. The thickness of the stiff walls is designed to ensure $c = c_{cr}$ at this recovery temperature 18 °C. The analysis was performed in ABAQUS 6.18, and four-node plane strain elements (CPE4R) was used to discretize the model. The test procedure was as follows:

(1) From t=0 to 10 seconds, T=T_l=8°C, the sample was compressed to transform from BP_1 to BP_2.

(2) The sample kept in BP_2 at T_l for 5 seconds.

(3) From t=15 to 25 seconds, the temperature gradually increases to T_h=22°C and recorded the T_t.

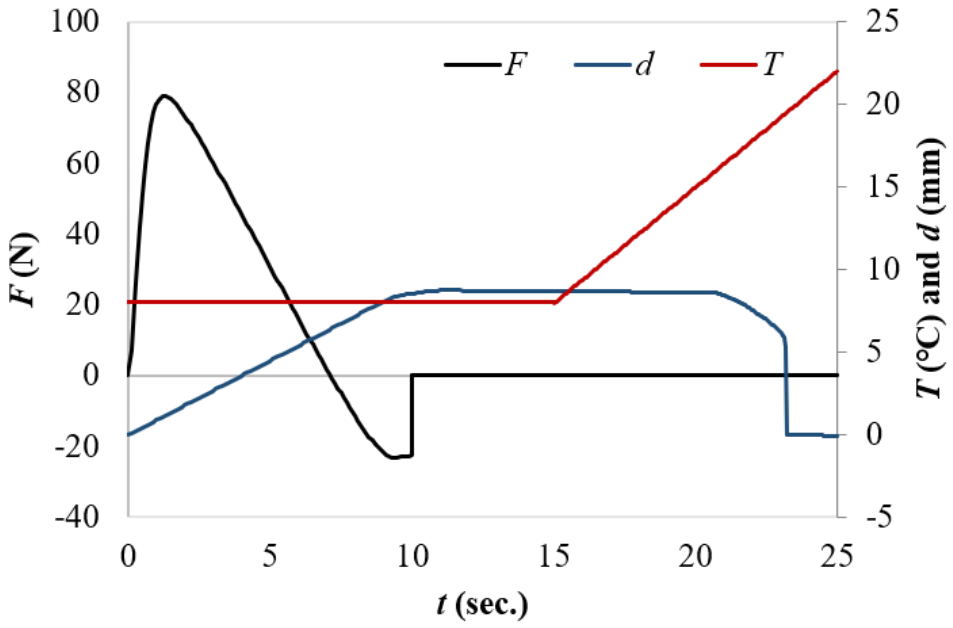

Figure A14: Reaction force, displacement, and temperature of the PXCMs sample vary with time during the recovery process.

Figure A14 shows how the reaction force, displacement on top of the sample, and temperature changes with time. As expected, the sample remains in state BP_2 for 10 minutes at 8°C. As the temperature increased, there was no observable change until the temperature reached 18°C. At 18°C, the PXCM began to transform to MP_1. The transformation was completed by 19°C. The transition temperature T_t, obtained from both FE simulation was close to the design value.

A6. PXCMs Design

To evaluate and show to the feasibility of *Type II* and *Type III* PXCMs, FE simulations, are created to here. All the simulations in this section were modeled using nonlinear finite element analysis in the finite element commercial package Abaqus 6.15. Element CPE4R, 4-node bilinear, reduced integration with hourglass control, are used to model the building blocks.

In *Type II* PXCMs, the center stiff wall is made of m_2 and the remainder is made of m_1. When temperature increases, the center bar softens and allows the sinusoidal beam to transform back to its original configuration through an asymmetric rotational mode. Figure A15 shows the shape-memory effect of a *Type II* PXCMs building block. At T_l=1℃ the building block transformed from BP_1 to BP_2 at via an applied force. The force released at t=9 sec. and the temperature remains the same. The temperature started to increase at t=10 second. The building block transformed from BP_2 to MP_2 through a rotational mode.

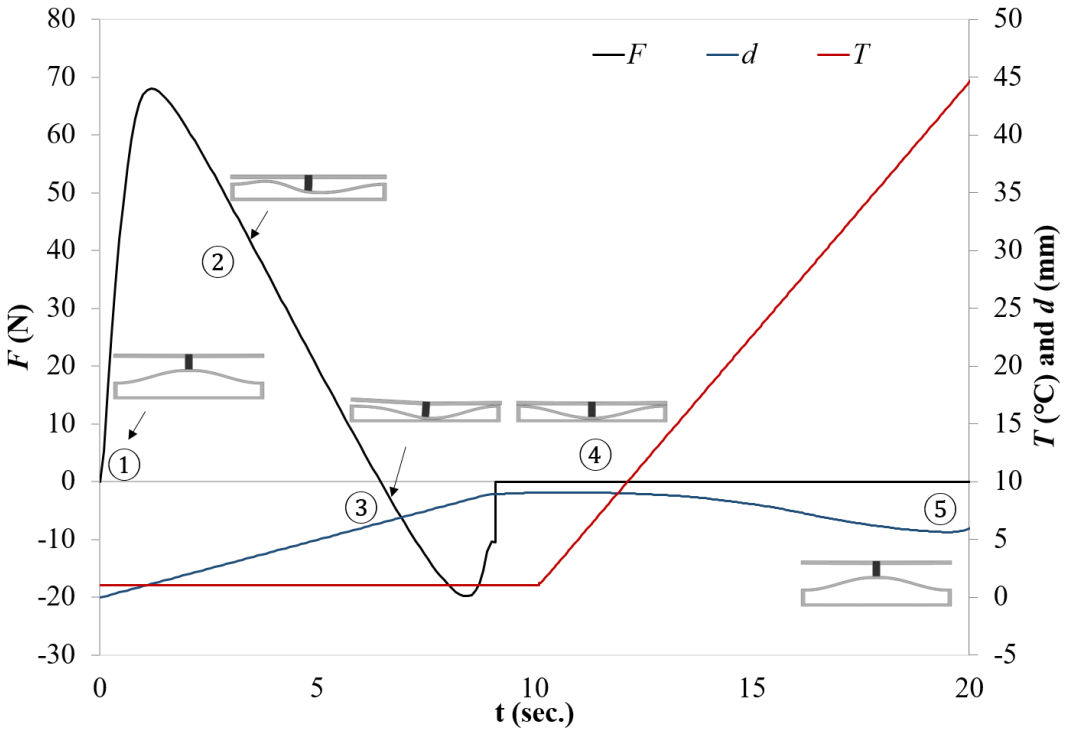

Figure A15: Recovery process of the *Type II* design. Force, displacement, and

In *Type III* PXCMs, a small portion of the sinusoidal beams around their inflection points is made of m_2 and the remainder is made of m_1. Under low temperatures, each unit cell is similar to a single isotropic, homogeneous material 1D PXCM building block. When $Q=A/t$ is sufficiently high, the building block can remain at BP_2 under stress-free condition. Under high temperatures, the building block performs like a sinusoidal beam missing two parts which is metastable. To demonstrate this design, the FE simulation of this design FE simulations of a *Type III* PXCMs building block and a building blocks missing the same portion of the sinusoidal beams around their inflection points were created to demonstrate the design concept. The *Type III* PXCMs building block underwent the phase transformation at T_l=1℃ and T_h=40℃ are shown in Figure A16 a and b respectively. The building block missing the part of materials at where *Type III* PXCMs building block assigned with m_2 perform the phase transformation at T_h=40℃ are presented in Figure A16 c. The *F-d* relationships of these three cases are plotted in Figure A17. As expected, *Type III* PXCMs building block underwent the phase transformation at T_l=1℃ exhibit bistable behavior. At T_h=40℃, *Type III* PXCMs building block and the building block missing two parts show the similar metastable behavior. Under high temperatures, the building block performs like a sinusoidal beam missing two parts which is metastable. Therefore, it can transform from BP_2 to MP_1 via temperature control. All these designs were evaluated and shown to be feasible alternatives using FE simulations, the details of which can be found in the supplementary materials.

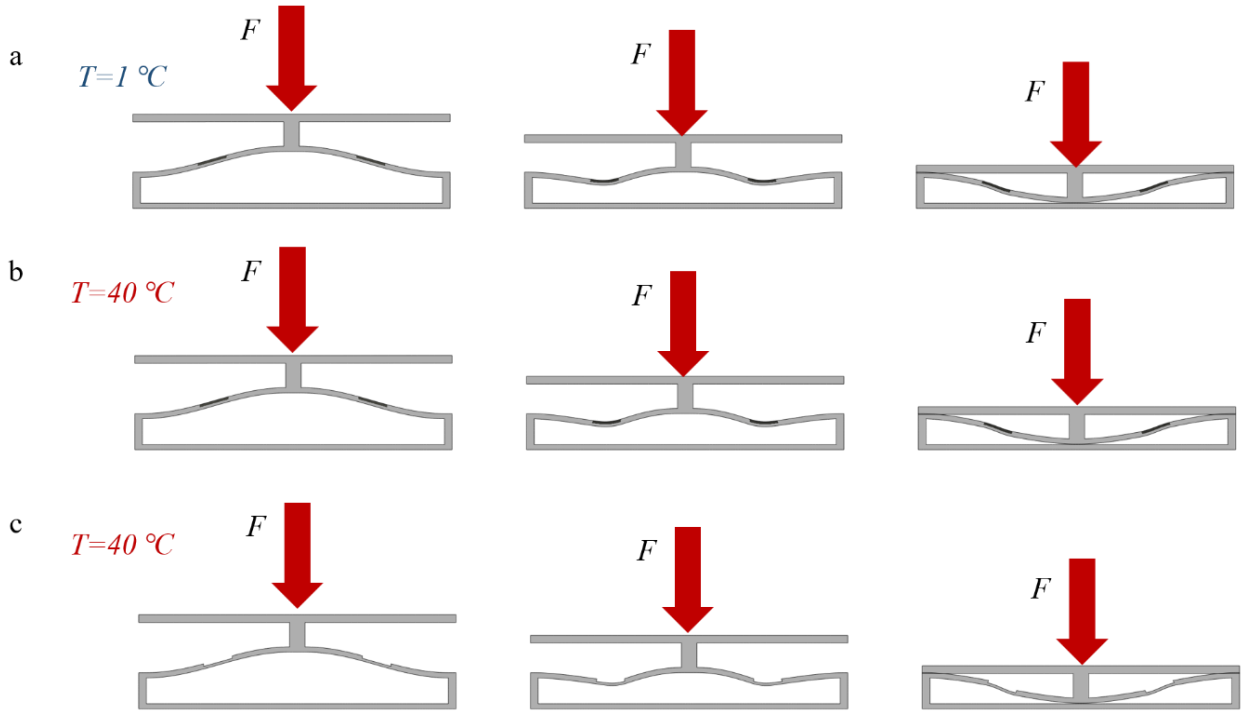

Figure A16: Load *Type III* PXCMs at low and high temperature.

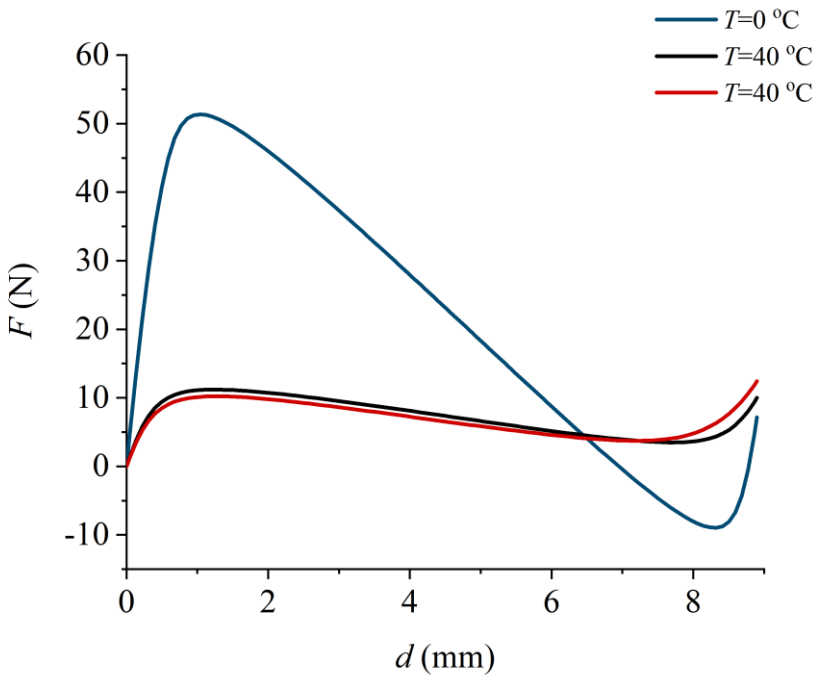

Figure A17: *F-d* relationship of the building block corresponding to Figure 16.

Figure A18 shows the shape-memory effect of a *Type III* PXCMs building block. At T_l=1℃ the building block transformed from BP_1 to BP_2 at via an applied force. The force released at t=9 sec. and the temperature remains the same. The temperature started to increase at t=10 second. The building block transformed from BP_2 to MP_2.

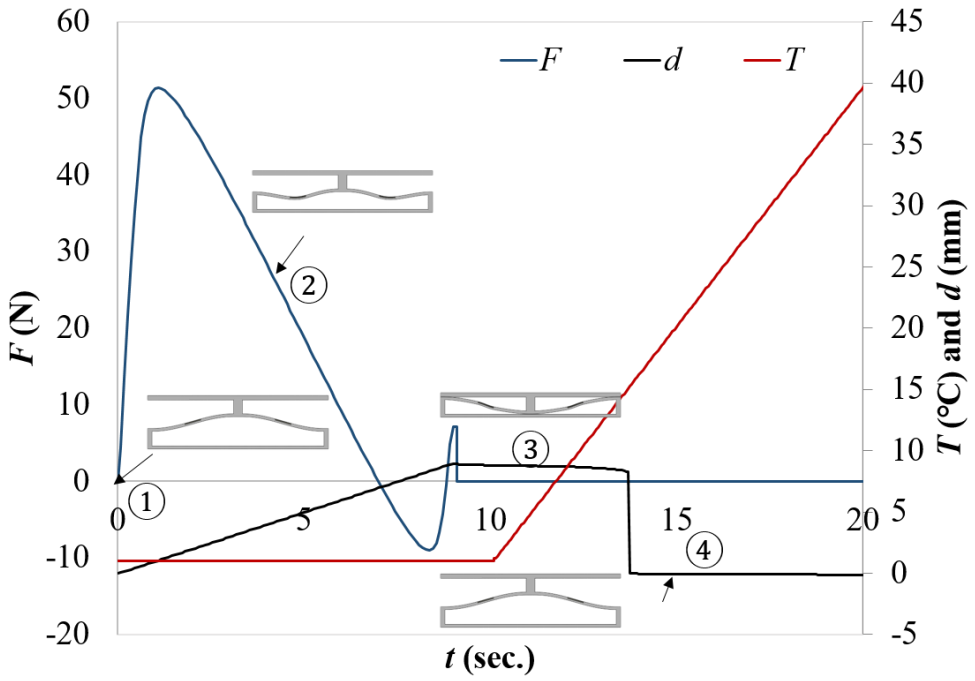

Figure A18: Recovery process of the *Type III* design. Force, displacement, and t

APPENDIX B.

B1. Design of 2D PXCMs

In this paper, we present a systematic study to design and study the mechanical performance of functional two-dimensional phase transforming cellular materials (PXCMs) that are capable of dissipating energy along various axes of symmetry. We created a series of designs and then we evaluated them through FE simulations (Figure B1 and Figure B2). While the extension to 2D PXCMs may seem easy by follow the schematics shown in Figure B1, the process requires a careful examination of the performance of the different types of designs. As mentioned in section 2.2, 2D PXCMs have three levels of hierarchy structures from level zero to level two. The *zeroth* level of the hierarchy structure is the elementary building block of the PXCMs which are composed of either single (Figure B1 a) or a pair of parallel-connected sinusoidal beams (Figure B1 b). To evaluate both designs, the FE simulations of two *S-type* PXCMs samples with these two types of building blocks under a uniaxial load-unload cycle are created.

We observe that the sample with single sinusoidal beams as elementary building blocks shows local wobbling behavior (Figure B1 a), which causes unpredictable and disorderly transformation behavior of materials. This local “wobble” mode is caused by the rotation at the apex of the single sinusoidal beam mechanisms. On the other hand, when the elementary building blocks are parallel-connected sinusoidal beams, materials transform steadily and progressively (Figure B1 b). This is mainly caused by the fact that rotation at the apex is restricted with parallel beams.

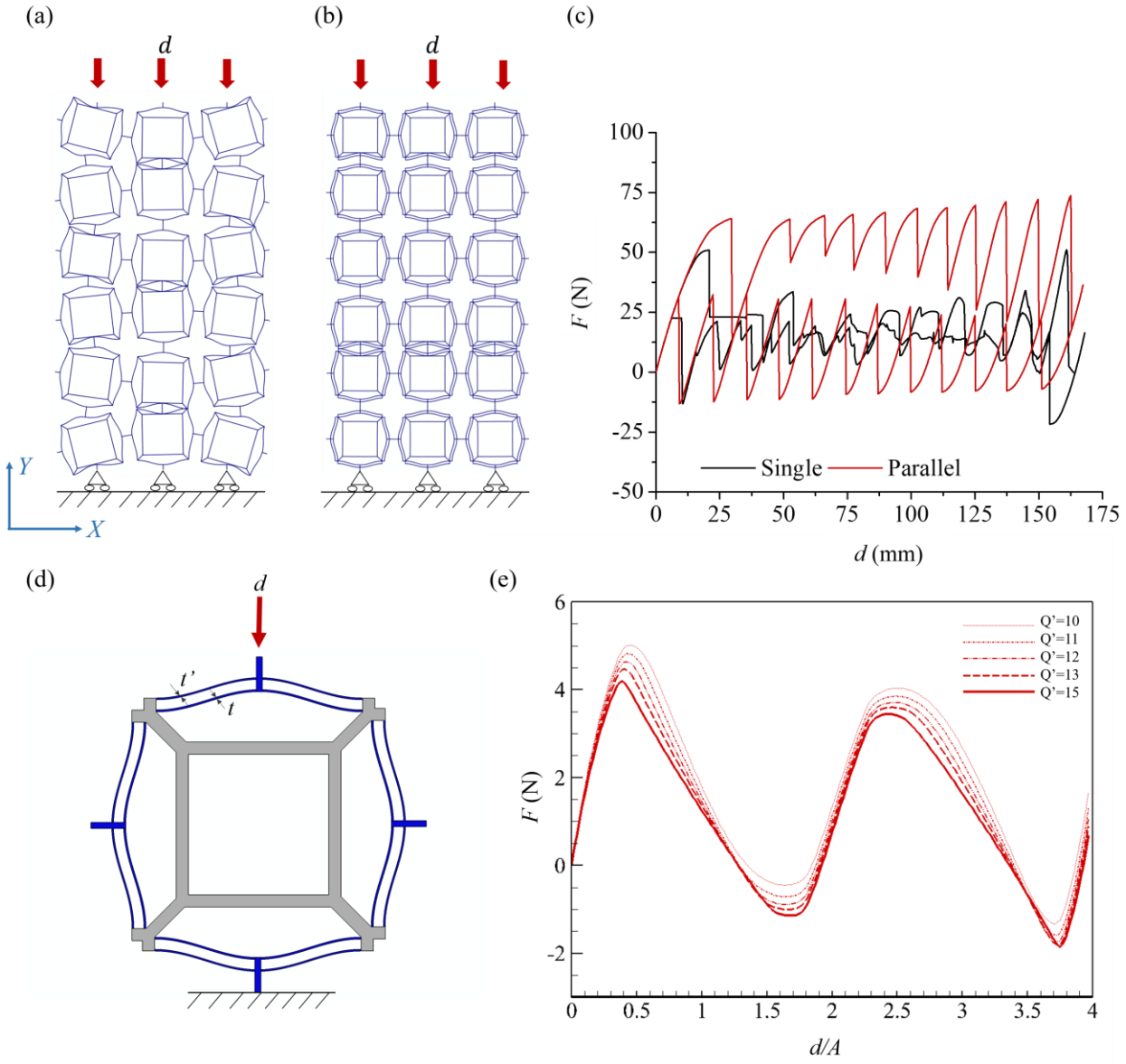

Figure B1: Performance of *S-type* 2D PXCMs with the zeroth level hierarchy structure are comprised of (a) single and (b) parallel connected sinusoidal beams under a compressive load-unload cycle. (a) Unit cells with single sinusoidal beam exhibited strong rotation. (b) Unit cells with parallel-connected sinusoidal beams did not rotate. (c) *F-d* relation of two samples indicates that *S-type* 2D PXCM with parallel-connected sinusoidal beams as elementary building blocks dissipates more energy. (d) *S-type* 2D PXCM motif under a uniaxial load. (e) Motif exhibits higher bistability but lower peak and valley forces when the top sinusoidal beam thinner.

Figure B1 c shows the result of the simulations (Load-Displacement, *F-d* curves) of the both cases (single beam and pair of parallel-connected beams). These results indicate that materials with parallel-connected sinusoidal beams as *zeroth* level of the hierarchy structure can have higher

better bistability behavior (e.g., larger peak to valley force ratios) which leads to better energy dissipation capacity. Additionally, the thickness of each individual beam in the two parallel-connected sinusoidal beams can be tailored independently to influence the performance of the material. To understand the effect of having different values of thickness in the top and the bottom sinusoidal beams, we performed FE simulations of a group of *S-type* 2D PXCMs under the displacement-controlled uniaxial compression. For each building block, the amplitude A and wavelength λ of both sinusoidal beams, the thickness t of the bottom sinusoidal beam, and supports thickness $t_{stiffer}$ are identical among the simulations. The only variation among different simulations is the thickness t' of the top sinusoidal beam (Figure B1 d). We define a parameter $Q' = A/t'$ as an indicator of the value t' *(since A remained constant)*. The parameter Q' varies from 10 to 15 among our simulations (Figure B1 e). The rest of the dimensions follow those indicated in Table S1. The relation between force and normalized displacement *(d/A)* of all the simulations are displayed in Figure B1e. These *F-d* curves indicate that, when all the other geometry parameters remain constant, the thinner the top sinusoidal beam is, the lower the peak and valley forces are, and the mechanism is said to become "more bistable". This means that the bottom part of the force-displacement curve crosses the $F = 0$ line (e.g., the valleys remain negative while the peaks are positive), and the distance between peaks and valleys increases. Another interesting observation is that, during phase transformation, the top sinusoidal beam transforms first because the only lateral constraints are provided by the vertical stiffening walls. However, these top beams push the stiffening walls apart, reducing the constraints on the bottom sinusoidal beam. This competing mechanism can be tailored with additional analysis by finding the right combination of Q' and Q. However, to maintain the focus of the paper, most of PXCMs considered in this work have parallel sinusoidal beams with the same in thickness ($Q=Q'=10$, $t=t'$; see Table B1).

After analyzing these two design options at *zeroth* level of hierarchy structure, we studied two potential design options in the *first level of* the hierarchy structure of 2D PXCMs. Triangular and square motifs are natural candidates for building the *first* hieratical level of 2D PXCMs because they can be tessellated in a 2D plane. The building blocks are assembled by combining the sinusoidal beams together into *first* level motif. The first type of frame connects the sinusoidal beams from their ends with spokes that converge at the center of a motif (Figure B1 d). The second type also connects all the sinusoidal beams via the ends, but form a polygon frame inside a motif.

To evaluate both design choices, we perform FE simulations of *S-type* 2D PXCMs with these two types of frames as it is shown in Figure B2 a and b. Under a displacement-controlled compressive load-unload cycle, both specimens collapsed steadily. However, the *F-d* curves (Figure B2c) indicate that the specimen with spokes (Figure B2 a) exhibits almost no hysteresis compared with the specimen with the center frame (Figure B2 b). Therefore, with adopt the center frame as the choice for *first* level of hierarchy (see Figure B2 b)

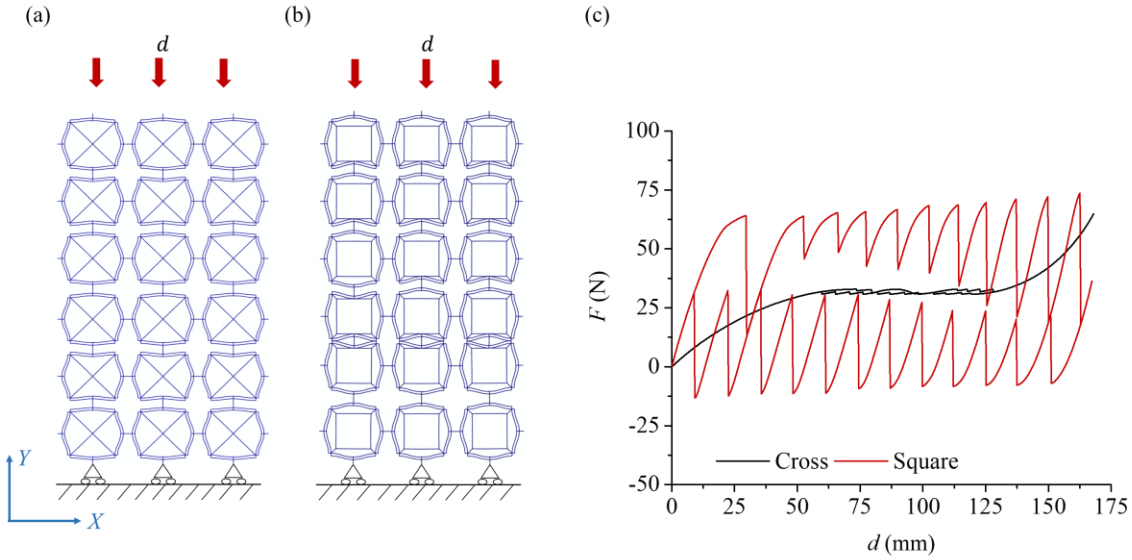

Figure B2: Performance of S-type 2D PXCMs with the two types of frames inside their motifs under a compressive load-unload cycle. (a) FEA model of *S-type* 2D PXCM with cross structures inside their motifs. (b) FEA model of square 2D PXCM with polygon frames inside their motifs. (c) *F-d* curves of two designs indicate that with polygon frame inside a motif, *S-type* 2D PXCM can dissipate more energy.

The determination of the second level of hierarchy follows a similar analysis through FEM analysis. The square motifs can be tiled easily as shown in Figure 5.1 e. Choosing the support structures for these triangular shape motifs is not straightforward. Two alternative support structure topologies T_I and T_{II} are shown in Figure 5.1 e. To evaluate the support structure topology T_I, a corresponding prototype is fabricated by an Object Connex500 3D printer with a photo-cured polymer (RGD 8530, $E = 1GPa$ and $\sigma_y = 19\ MPa$). The sinusoidal beams are designed to remain elastic during the phase transformation. Ten compressive load-unload cycles were applied on the specimen using a universal testing machine (MTS Insight 10 equipped with a 10 kN load cell MTS 661.19F-02) (Figure B3 a and b). We observe that the supports and frames of the PXCM deform just enough to

eliminate any constrain to the sinusoidal beams to obtain bistability. The hysteresis curves indicate that the energy dissipation is mostly plastic deformation rather than phase transformation. Therefore, regular tiling (T_I) does not lead to a functionally two-dimensional PXCM. The arrangement shown in (T_{II}) with triangular motifs located at the nodes of a regular hexagon is not a tiling as it includes some empty space at the center of the hexagon. As it is shown in the main paper, this arrangement leads to a functionally 2D PXCM. Optimization could be performed to improve the performance of 2D PXCMs in terms of energy dissipation, strength, or initial stiffness.

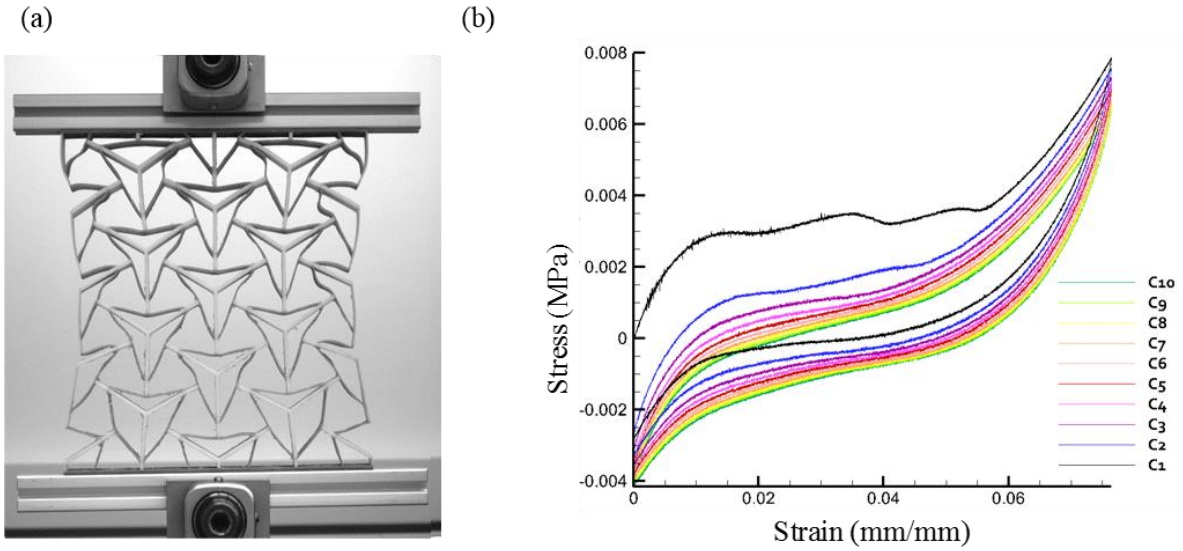

Figure B3: Example of an unsuccessful design. T-type 2D PXCM with TI arrangement show plastic deformation under ten compressive load-unload cycles.

B2. Characterization 2D PXCMs

Uniaxial, quasi-static, compressive load-unload tests were performed to characterize the response of the *S-type* and *T-type* PXCMs along the various axes of symmetry of the materials. These tests were carried out under displacement control. Four specimens corresponding to four tests are fabricated (Figure 5.3-Figure 5.6). The volumes of samples are displayed in Table B2. These load cases are tested using nonlinear finite element analysis. This analysis helps us understand whether or not there is phase transformation, acknowledging that the applied displacement in the beams is a function of θ, where θ is the angle between the loading direction and axis of symmetry of a sinusoidal beam (see Figure B4 c). The applied displacement on each sample follows Eq. B1:

$$d = 2A \sum_{i=1}^{n} cos\ (\theta_i) \qquad \text{(B 1)}$$

where A is the amplitude of a sinusoidal beam, θ_i is the angle between the axis of symmetry of the i^{th} sinusoidal beam structure and the loading direction, and n is the total number of such sinusoidal beam structures along any column of motifs in the material sample. All the specimens are tested with three compressive load-unload cycles with the loading rate of 1 *mm/min*.

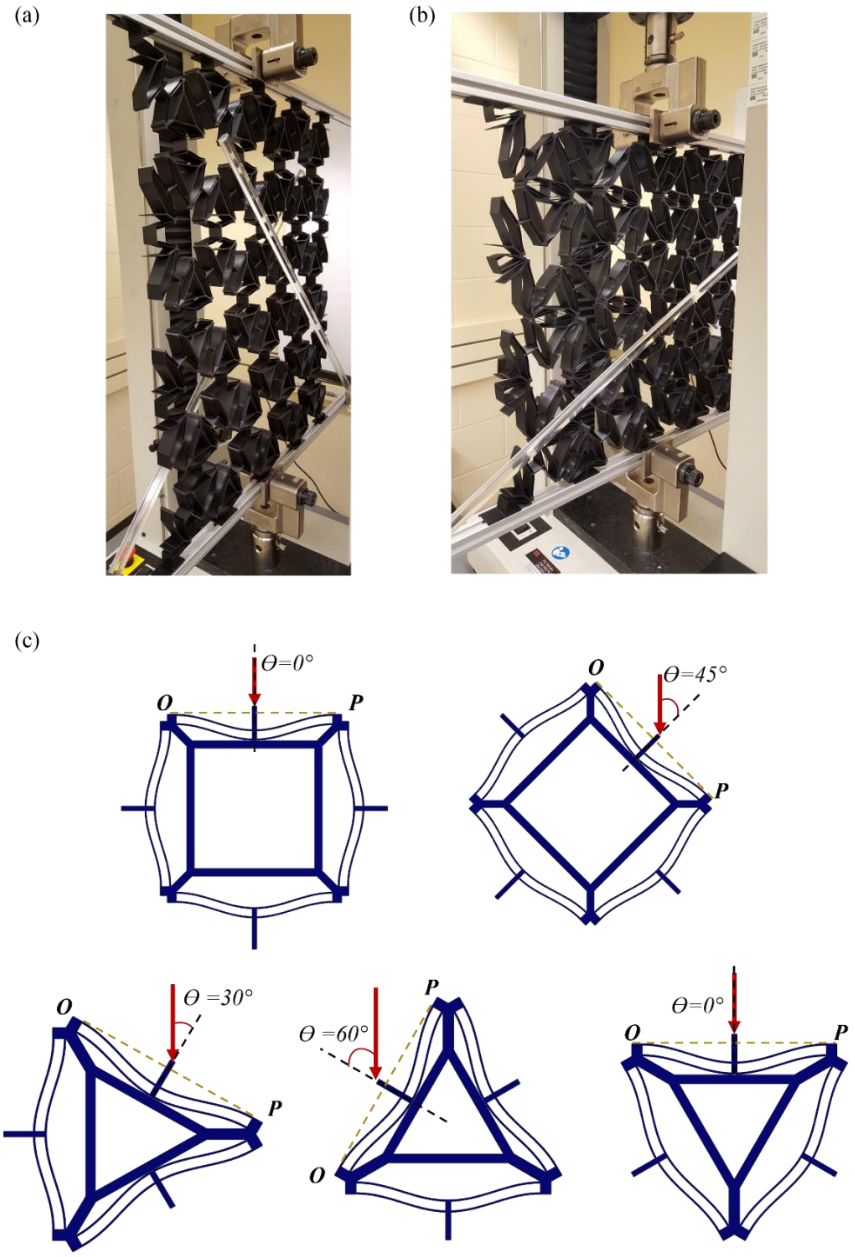

Figure B4: Experimental set up for the uniaxial loading tests on four samples. (a) undeformed and (b) deformed T-type at loading {0°, 60°, 120°} under uniaxial loading condition. Two acrylic bars are employed to laterally constrain the specimen at front and back to eliminate out of plane buckling. (c) FEM results showing how the cells undergo complete phase transformation, even when the applied displacement is a function of the angle θ.

B3. Results and Discussions

Figure B5 shows the *F-d* curves of each sample under three compressive load-unload cycles from experiments. Table B3 displays the energy dissipation of all the specimens among three back-to-back load-unload cycle. The variation among different cycles is between 1% and 8%. With the exception of the *S-type* 2D PXCMs loaded at {45°, 135°}, all the samples exhibit energy dissipation reduction after the first loading cycle. After the first loading cycle, the energy dissipation variation between second and third cycles decreases (Table B3-B4).

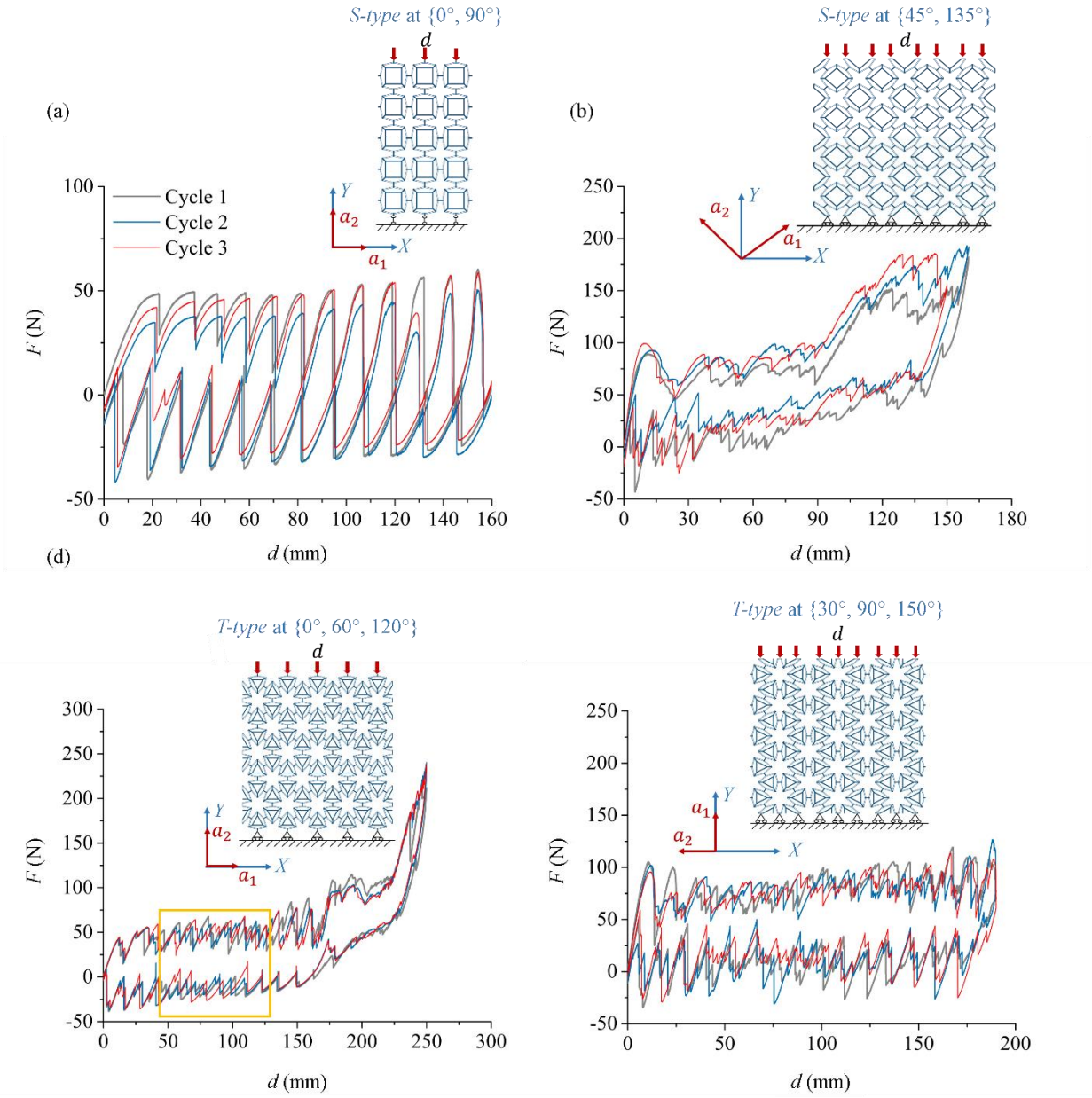

Figure B5: Experimental *F-d* curves for three compressive load-unload cycles.

B3.1 Phase Transformation Path

The observation from the tests confirm that most of the mechanisms under phase transformation through different level of asymmetry configurations. For instance, when the *S-type* 2D PXCM sample is loaded at {0°, 90°}, half of the sinusoidal beams happen to have their axes of symmetry overlapped with the loading direction. These sinusoidal beams transformed through the symmetric configurations, which is defined as the mechanisms go through the primary pathway (Figure B6a). The other half of the sinusoidal beams do not go through phase transformation because the loading direction is perpendicular to their axes of symmetry. The *F-d* relation (Figure B5 a) of this specimen indicates that *S-type* 2D PXCM under loading angle {0°, 90°} show bistable behavior and energy dissipation. The materials perform differently when the loading direction for the sample is not aligned with axes of symmetry for a subset of the constituent mechanisms (Figure B5 b -d).When *S-type* 2D PXCM is loaded at {45°, 135°} loading angles (Figure B5 b), every sinusoidal beam has its axis of symmetry 45° rotated from the loading direction (θ=45°). This larger angle θ causes all the sinusoidal beams transform though more asymmetric configurations (Figure B6 b) compared with the previous case. As a result, the specimen exhibits mostly metastable behavior and lower energy dissipation capacity. In such cases, when a mechanism transforms via such an asymmetric configuration, we say that those mechanisms go through a secondary pathway. When the *T-type* 2D PXCM is loaded at {0°, 60°, 120°}, one third of sinusoidal beams with their axes of symmetry align with the loading direction. These sinusoidal beams go through the primary pathway; similar to half of the sinusoidal beams in the *S-type* 2D PXCM at loading angles {0°, 90°}. The rest of sinusoidal beams, which have their axes of symmetry 60° rotated from the loading direction, transform through the asymmetric configurations and exhibit metastable behavior (Figure B6 c). The *T-type* 2D PXCM at {30°, 90°, 150°} has one third of sinusoidal beams parallel to the loading direction. These sinusoidal beams clearly do not exhibit phase transformation. The rest of sinusoidal beams have their axes of symmetry 30° rotated from the loading direction (θ=30°). These sinusoidal beams transform through the noticeable asymmetric configurations, therefore we define the mechanisms go through secondary pathway as well. Since the angle θ is relatively small compared with the previous two cases, the sample shows bistability and relatively high energy dissipation (Figure B6d)

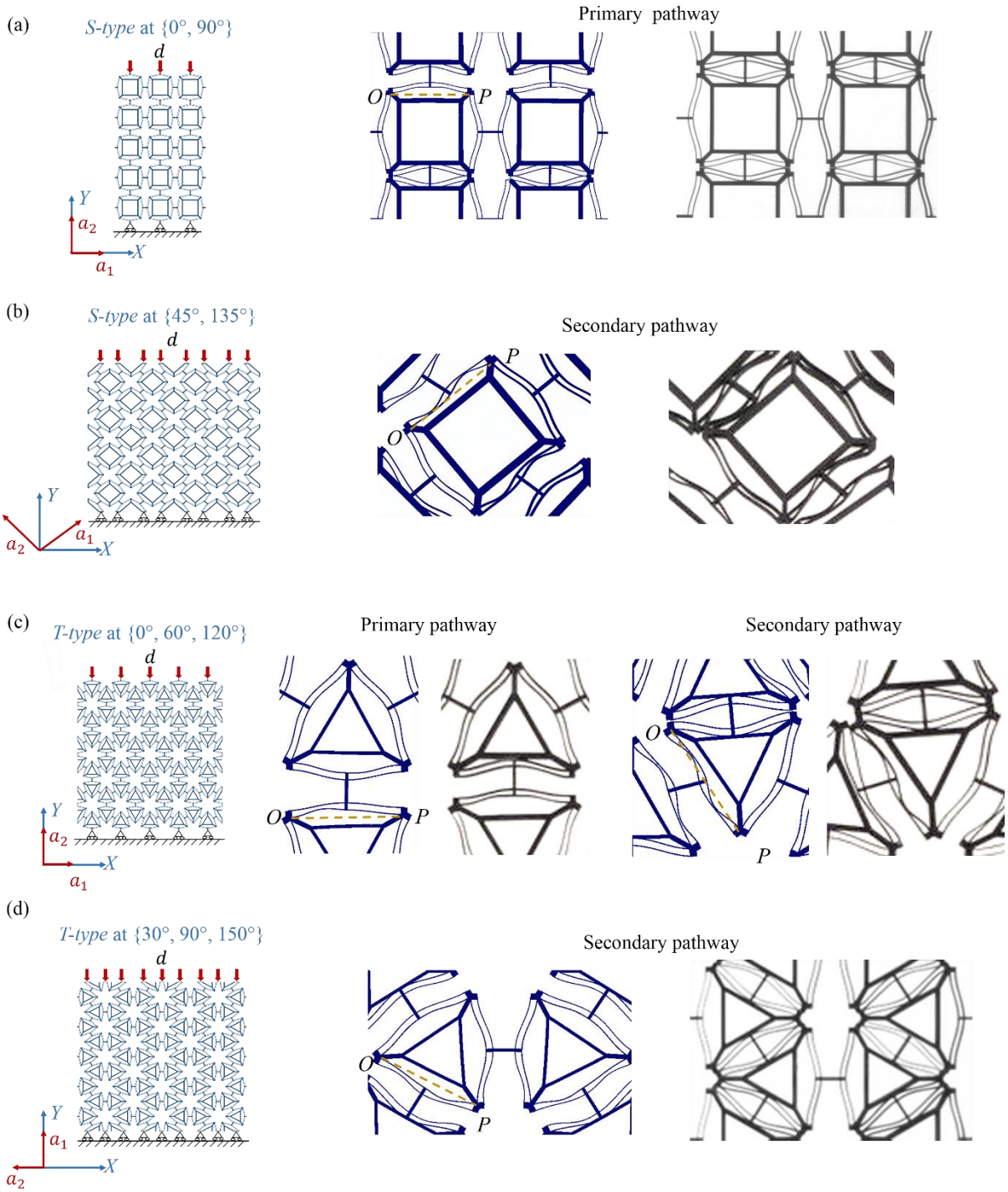

Figure B6: The simulations (left) and experiments (right) show that the sinusoidal beams have phase transformation through more asymmetry configurations when the angle θ between the loading direction and their axes of symmetry increase.

B3.2. Phase Transformation in a Single Mechanism

The experiments and FE simulations discussed in this paper show that the angles between loading directions and axes of symmetry of sinusoidal beams affect the performance of materials in terms of bistability and energy dissipation capacity. In order to better understand this influence, we perform ancillary FE simulations of a single mechanism under loads applied at various angles, θ (see Figure B7 a). Figure B7 b shows the *F-d* responses as a function of the angle θ. We note that the mechanism response is clearly bistable for θ =0 with a well defined second stable configuration and a long region with negative stiffness. However, the mechanisms become metastable as θ increases, and the negative stiffness region in the response shrinks rapidly as θ increases from 0° to 15°. The negative stiffness region disappears completely for θ > 15° (see Figure B7 b)

As discussed, energy dissipation in PXCMs arises from the non-equilibrium release of energy accompanying the traversal of the limit points during the loading and unloading of these materials. Specifically, the energy dissipation in a material with a 'sufficiently' large number of motifs is proportional to the area bounded by the envelope curve shown by a dashed line in Figure B7 c-f [19,60]. Figure B7 g shows a plot of this area as a function of θ. We note that the area appears to decrease exponentially with increasing θ and becomes nearly zero for θ =15°. This shows that the energy dissipation capacity of the single mechanism degrades quickly as the inclination of the applied load with respect to its axis of symmetry increases, and it disappears completely for inclinations as small as 15 degrees. Based on the observations, we conclude that the larger the angle between loading direction and the axes of symmetry of a sinusoidal beam, the lower their ability to produce bistable behavior. This eventually adversely affects the capability of the material to dissipate energy. However, the observations from the tests on 2D PXCMs show that when the angle θ is larger than 15°, the material still exhibit bistable behavior and energy dissipation capacity (Figure B5). This is due to the collective behavior of all the cells, which produce enough lateral constraint even for those sinusoidal beams that have higher values of θ. This is discussed in the next subsection.

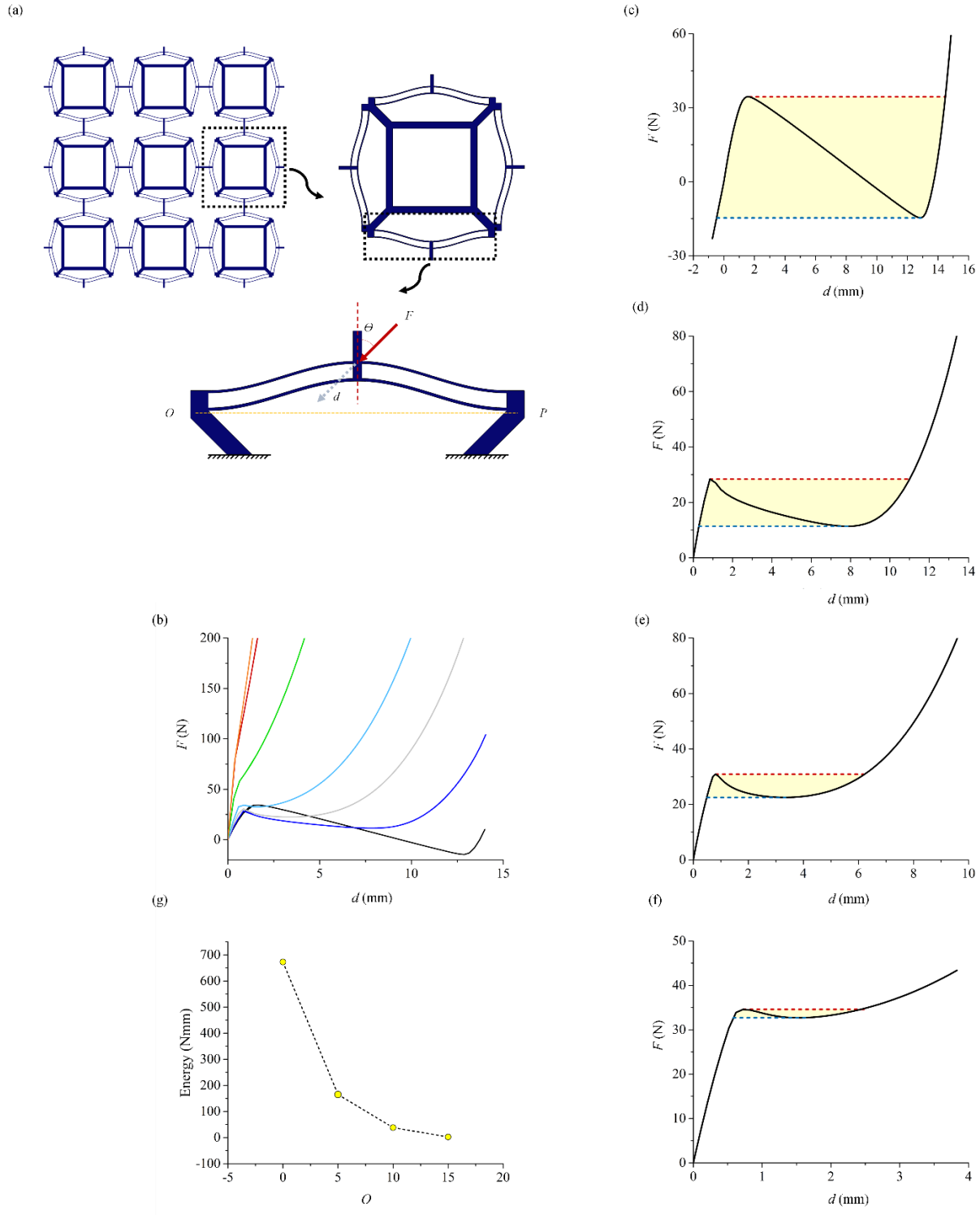

Figure B7: Performance of a single mechanism under the different loading direction. (a) A mechanism from S-type 2D PXCM is subtracted to study. (b) F-d relations of the mechanism when the angle between loading direction and axes of symmetry increases from 0° to 60°. (c)-(f) F-d relations of the mechanism when θ=0°,5°,10°, and 15°. Highlight area is proportional to the energy dissipation in materials is composed of a large number of mechanisms. (g) This area decreases exponentially with increasing θ.

B3.3. Phase Transformation in a 2D PXCMs

The *S-type* 2D PXCM has four axes of symmetry, but only two of these are aligned with axes of symmetry for its constituent single mechanisms. When a loading direction for these PXCMs is aligned with an axis of symmetry of the material that also happens to be an axis of symmetry for a subset of its constituent mechanisms, this subset of mechanisms contributes the most to the total energy dissipation of the specimen. Half of the mechanisms in the *S-type* PXCM are aligned with their axis of symmetry lying along the 0 degree direction, and the other half have their axis of symmetry along the 90 degree direction (see Figure 5.3). The mechanisms aligned at 0 degrees are not deformed significantly, and hence do not contribute to the total energy dissipation of the sample when the mechanism is loaded along 90 degrees. Similarly, the mechanisms aligned with 90 degrees do not contribute to energy dissipation when the sample is loaded along 0 degrees. Moreover, as the same number of mechanisms are active contributors to the total energy dissipation when the material sample is loaded along 0 and 90 degrees, we expect the total energy dissipation to be similar in these two cases.

The situation is different when the loading direction for the sample is not aligned with axes of symmetry for a subset of the constituent mechanisms (Figure 5.4 -Figure 5.6). Based on the prior discussion, we expect any mechanisms oriented in a direction such that their axis of symmetry is inclined 15 degrees or more with respect to the load direction to have a very small contribution to the overall energy dissipation (see Figure B7). However, an ensemble of mechanisms behaves somewhat differently than the single mechanism due to the internal degrees of freedom possessed by the individual motifs and its interaction with their neighbors. We notice that the individual cells in an ensemble reorient themselves during the deformation of the material such that they reduce the inclination of the force deforming a mechanism with respect to the axis of symmetry of the mechanism undergoing transformation (see Figure B8-Figure B10). This reorientation happens via rotation of the individual motifs based on which subset of its constituent mechanisms is transforming. Thus, we can observe the same motif rotating clockwise and counter-clockwise at different points in the loading history (Figure B9 & Figure B10). This behavior results in some energy dissipation contribution even from mechanisms that were oriented such that the direction of their axis of symmetry was inclined by 15 degrees or more with respect to the external force in the undeformed configuration. Moreover, the percentage of sinusoidal beams that undergo

transformation in *S-type* 2D PXCM significantly increases from 50%, when it is loaded at 0°/ 90°, to 100% when a is loaded at 45°.

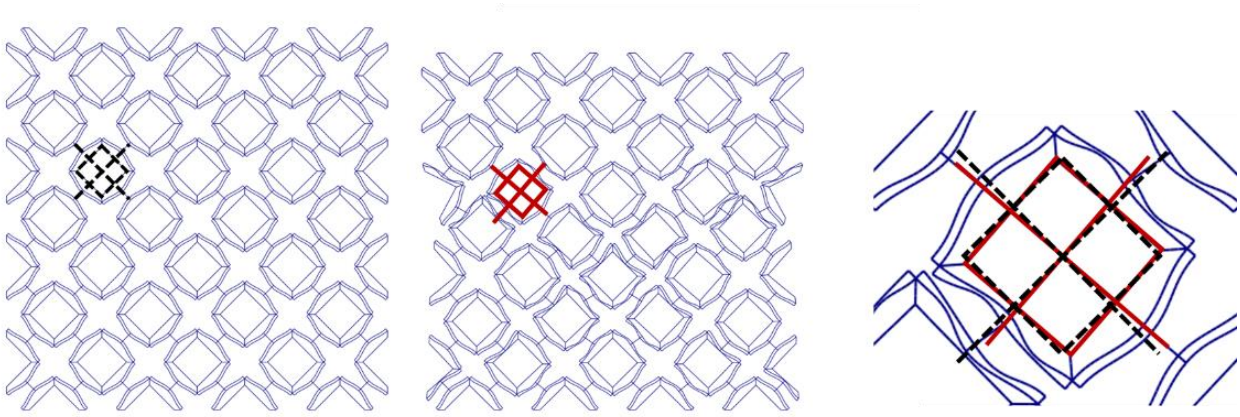

Figure B8: S-type 2D PXCM at {45°, 135°} loading angle show the rotation in the individual motif.

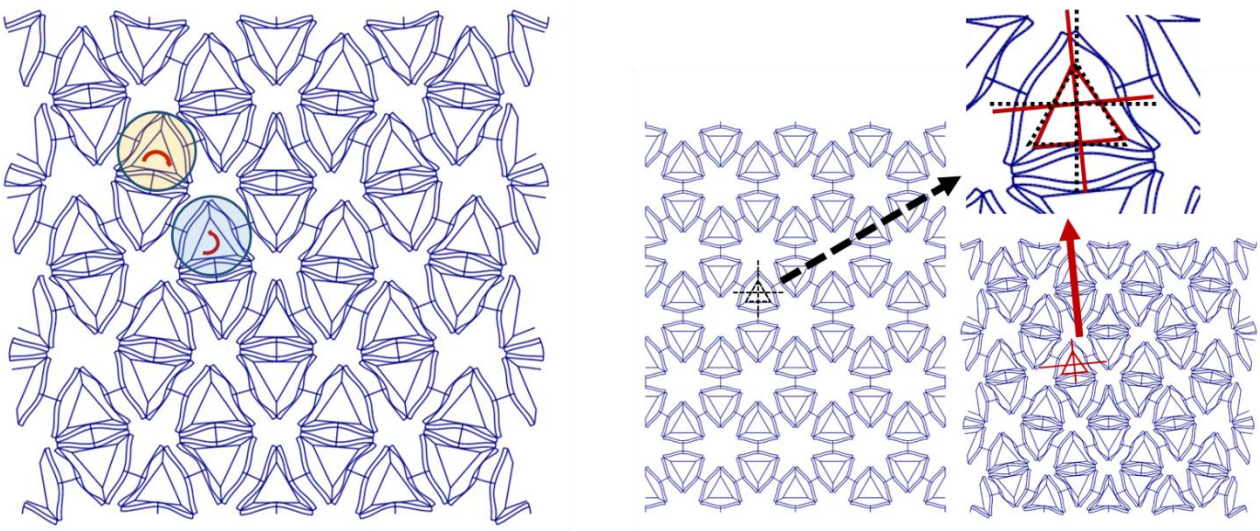

Figure B9: For *T-type* 2D PXCM at {0°, 60°, 120°} loading angle, the same motif rotating clockwise and counter-clockwise at different points in the loading history

Thus the relative small difference of the energy dissipation behavior of the *S-type* 2D PXCM to the direction of the in-plane loading can be explained by two counteracting trends: 1) a decrease in the energy dissipation contribution of an individual mechanism with an increase in the inclination of the applied load with respect to its axis of symmetry and 2) an increase in the number of mechanisms contributing to the energy dissipation of the sample as a whole with an increase in

the inclination of the applied load with respect to the axis of symmetry of any one subset of mechanisms. The behavior of both *T-type* 2D PXCMs can be explained in a similar manner.

We observe that the *T-type* material, which has more axes of reflectional symmetry then the *S-type*, exhibits slightly lower variation in energy dissipation with changes in the loading direction than the *S-type* material. This suggests that further increases in the number of axes of reflectional symmetry for the unit cell are likely to reduce the variation in energy dissipation with the changes in loading direction, with the advantage that the relative density of the material does not change significantly while increasing the symmetry of the unit cell.

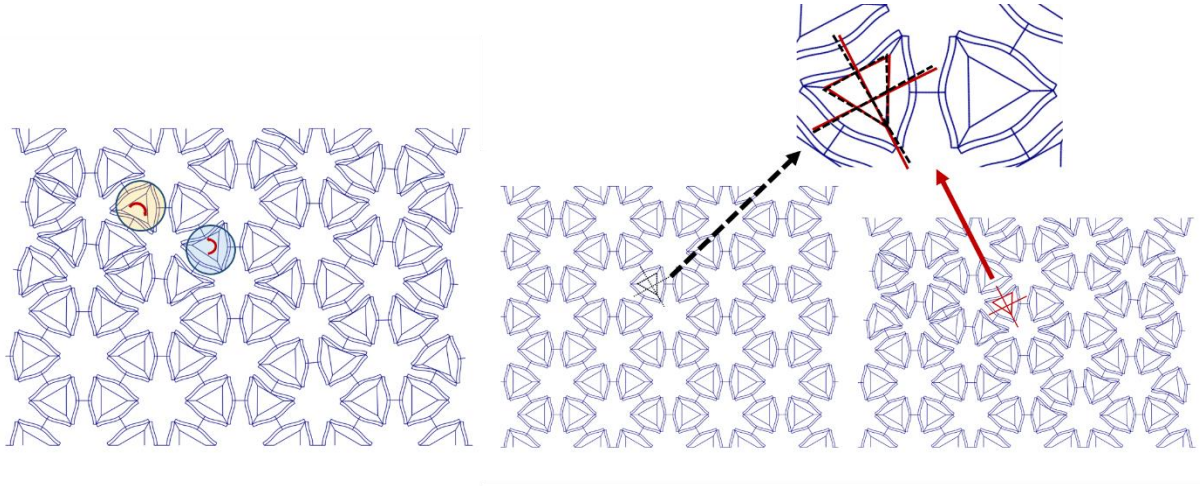

Figure B10: For *T-type* 2D PXCM at {30°, 90°, 150°}, the same motif rotating clockwise and counter-clockwise at different points in the loading history.

To verify the energy dissipation presented above is still produced by the PXCM when its base material remains in the elastic regime, we carefully analyze other type of sources for potential energy dissipation sources. This will allow us to examine and estimate how much of the total energy dissipated by a PXCM sample can be attributed to the primary and secondary pathways. Figure B5 show respectively the *F-d* responses of the *S-* and *T- type* PXCM samples when they are loaded at 0 degrees, for three back-to-back load-unload cycles. Irreversible (e.g. plastic) deformation across the successive cycles is negligibly small after the first cycle for all four load cases considered in this study (Table B4). This is confirmed not only by the *F-d* response (Figure B5), but also by a posteriori examination of the specimens that showed no sign of permanent

deformation. This is to be expected, as we designed the mechanisms such that it remained in the elastic strain regime over the complete load-unload cycle.

Estimation of the energy dissipation via the other secondary pathways listed above is not straightforward. The mechanisms are designed to have a bistable mechanical response. They exhibit snap-through behavior under force control, but not under displacement control. If we subject a single mechanism to the same range of deformation under force and displacement controlled conditions, it will dissipate energy via all available dissipation pathways in the former case. However, under displacement control, it does not undergo a snap-through and, hence, it does not exhibit dissipation due to the snapping action of the mechanism. We can estimate the energy dissipated by a mechanism via all dissipation pathways except the snapping action by subtracting the energy dissipated by the mechanism under displacement control from that under force control. Since the S-type PXCM loaded at {0°, 90°} showed the most irreversible deformation in successive load-unload tests, we choose that load case to estimate energy dissipation through pathways other than the snapping action of the beams. The average energy dissipated by the entire sample in cycles 2 - 3 is 6594 mJ (see Table B5). We subject a single mechanism from this sample to four successive load-unload cycles under displacement control with a cross head travel rate of 1mm /min (See Figure B11). The energy dissipated during a complete load-unload cycle is obtained by measuring the area between the loading and unloading curve (See Table B7 & Table B8). The average energy dissipated by a single mechanism over cycles 2 - 4 is 17.5 mJ (see Table B8). Since, 36 such mechanisms undergo a complete load-unload cycle during a complete load-unload cycle on the entire PXCM sample (see Figure 5.3), we estimate the total energy dissipated by the entire sample due to pathways other than the snapping action of the beams to be 630 mJ. Thus, assuming that all 36 of these mechanisms exhibit identical energy dissipation behavior we estimate that all secondary dissipation pathways other than plastic deformation dissipate approximately 10% of the total energy dissipated by the *S-type* PXCM sample when it is loaded at 0° and 90°.

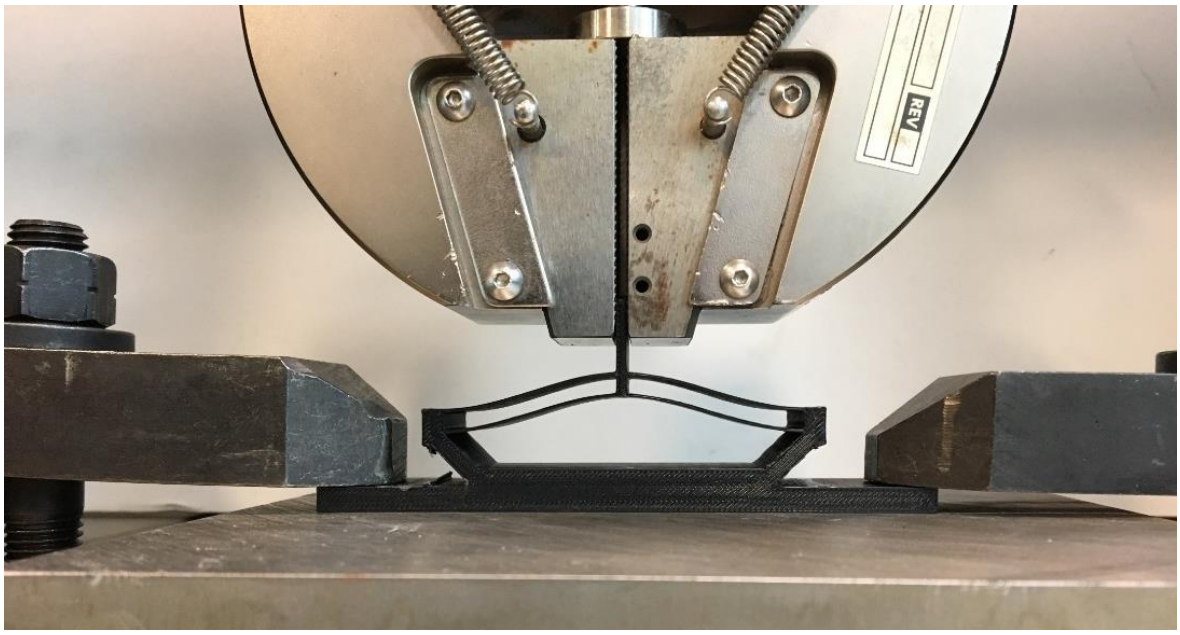

Figure B11: A single mechanism under displacement control with a crosshead travel rate of 1mm per minute.

B.3.4. Auxetic behavior

Under the uniaxial loading conditions along different axes of symmetry, both *S-type* and *T-type* samples exhibit auxetic behavior from FE simulations and experiments (See Figure 5.3-Figure 5.7, and Figure B12). These samples undergo contraction in the *X* direction when they are compressed in *Y* direction. To illustrate this effect, the Poisson's ratio ($v = -\frac{\varepsilon_Y}{\varepsilon_X}$) of *S-type* loaded at {45°,135°} and *T-type* at {30°,90°,120°} is plotted vs time in Figure B12 b and d.

The strain in *Y* direction is calculated by dividing average displacement of all the nodes on top of the sample by the original sample width *w*: $\varepsilon_Y = \frac{\overline{u_Y}}{w}$. The strain in *X* direction is calculated by the subtracting the average displacement in *X* direction of all the nodes on left side to right side and dividing the original length of the sample *L*: $\varepsilon_x = \frac{\overline{u_x^r}}{L} - \frac{\overline{u_x^l}}{L}$. Based on the geometry and typology of two samples, when mechanisms fully collapsed (Equation B1), the Poisson's ratio of *S-type* at {45°, 135°} is expected to be around -1, and *T-type* at {30°,90°,120°} should be around -0.28. This analytical value and FE simulations results are plotted together at Figure B12 b and d. It shows the good agreement between the Poisson's ratio from FE simulation and analytical results. By having these auxetic behaviors, 2D PXCMs gain more benefits such as high indentation resistance, shear

modulus, fracture toughness, and synclasticity [55] . These benefits extend the application of 2D PXCMs into medical stent, adaptive clothing, and medical cast [54,56,57].

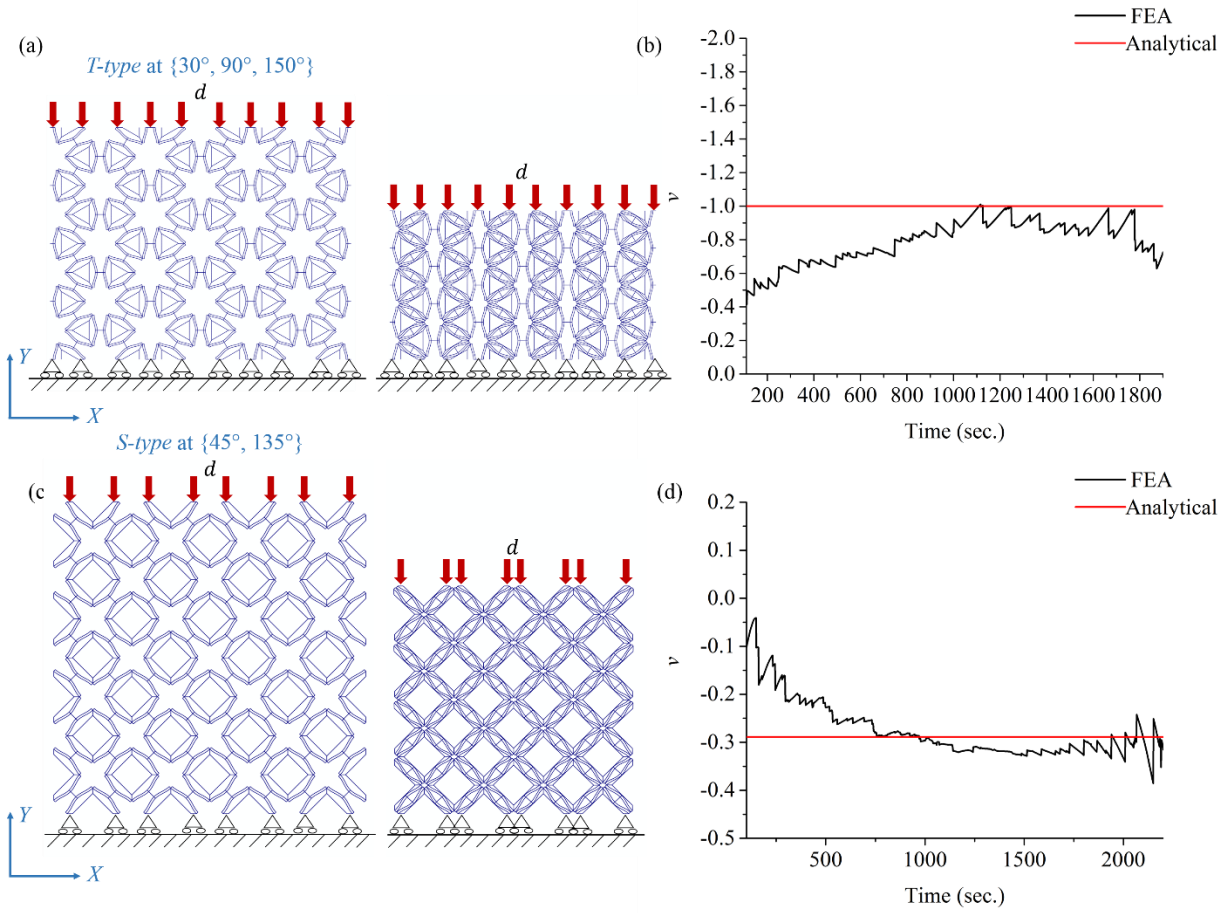

Figure B12: Poisson's ratio variation over time obtained from the numerical simulations and compared with the analytical prediction.

B4 Finite Element Simulations

Finite element models are created to quickly capture the essential mechanical response of 2D PXCMs under different loading angles. Element type, element size, contact condition, and base material properties were first studied to determine the most effective simulation set up and assess potential source of error and uncertainties.

B4.1. Element Type

To select a type of computational effective element, we create FE models of a 2D PXCM elementary mechanism (i.e. sinusoidal beam) with clamped-clamped boundary conditions and

under displacement control with different elements types (Figure B13 a). The geometry of the sinusoidal beam is identical to the sinusoidal beams employed in the *T* and *S-type* 2D PXCMs.

(a) (b)

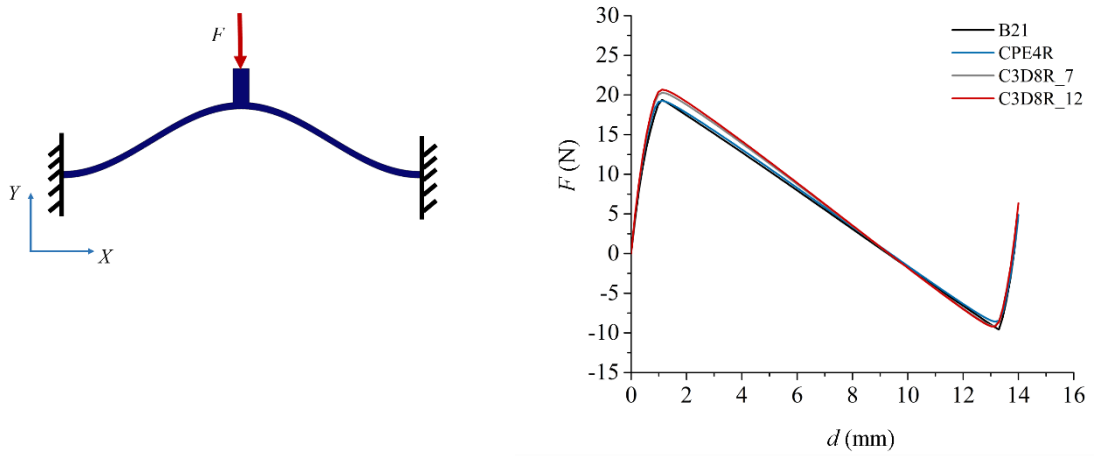

Figure B13: FE models of the elementary mechanism. (a) FE model is an elementary mechanism under the clamped-clamped boundary condition. (b) There is no significant difference can be observed by using different types of element.

The elements selected are: two-node linear beam element (B21), four-node bilinear, reduced integration with hourglass control (CPE4R) and eight-node brick element with reduced integration (C3D8R). For 2D and 3D models, 7 elements are assigned throughout the beam thickness (element size = 0.1 mm). Additionally, to check convergence for the 3D model, a model with sinusoidal beam with 12 C3D8R elements throughout the sinusoidal beam thickness is created. The *F-d* relations of four models are plotted in Figure B13b. As it can be observed in the figure, there is no significant difference between the models with B21, CPE4R, and C3D8R elements. We choose B21 for all the simulations as it is the most computationally efficient and it enables us to create larger models with multiple motifs.

B4.2. Convergence study

Once the element type is chosen, a convergence study is conducted on the sinusoidal beam model with B21 elements. The element size varies from 4 mm to 2 mm. The *F-d* relation curves of five models with these various elements size are shown in Figure B14 a. Since only minor variation can be observed from the *F-d* curves, the peak force F_p of each curve is used to quantify the

difference. We plot F_p against element size as shown in Figure B14 b. The peak load converges when the element size reduced to 2.5 mm. We chose the element size 2.17 mm which is smaller than the threshold of convergence (this is shown as red dot shown in Figure B14 b.

(a)

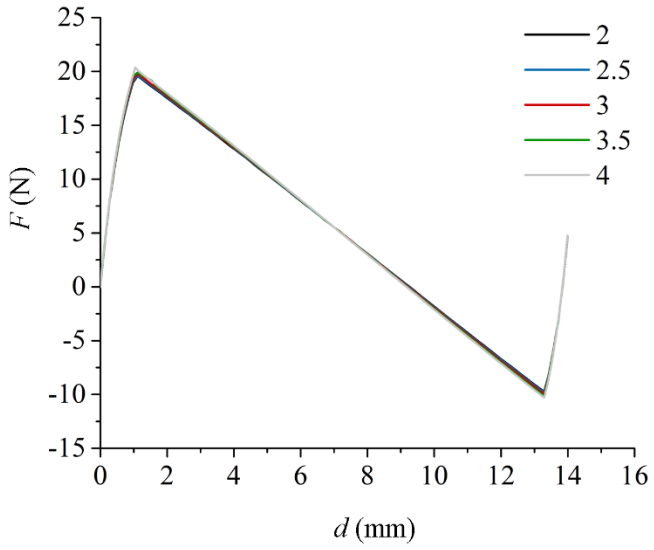

(b)

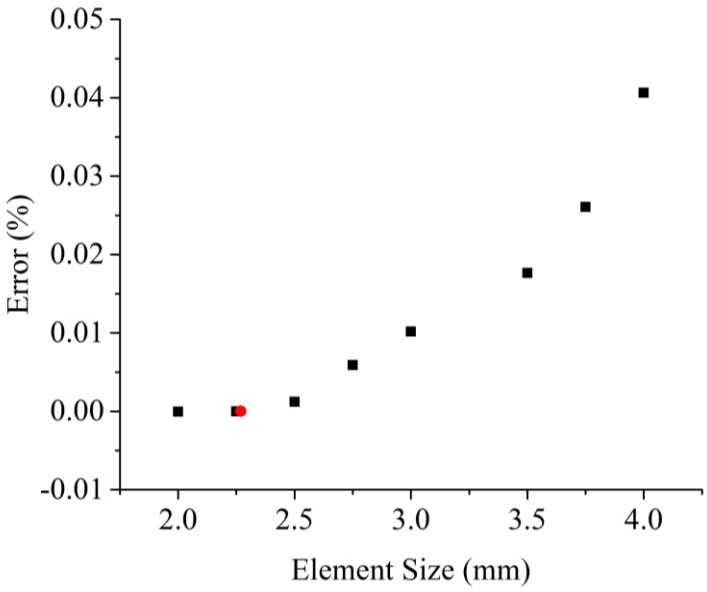

Figure B14: Convergence study of FE models. (a) *F-d* relations of FE models with element size varies from 2-4 do not show noticeable difference. (b) Peak load of sinusoidal beam starts to converge at 2.5 mm.

B4.3. Friction coefficient

Contact between adjacent beams was modeled using the small sliding formulation in Abaqus 6.14. Coulomb friction with a friction coefficient of $\mu = 0.1$ is assumed to be active at all contact interfaces. This value is selected based on the Typical Properties of Generic Acrylonitrile Butadiene Styrene (ABS)[61]. For generic ABS materials, the coefficient of friction varies from 0.1-0.5. To check the sensitivity of the friction coefficient in our models, we build FE models of the *S-type* PXCM loaded under {0°, 90°} (with μ varying from 0.1 to 0.5). The *F-d* relations of these models are shown in Figure B15. The model with $\mu = 0.1$ exhibits slightly lower valley force when the 11th mechanism buckles at the very end of the loading cycle. This is an indication that contact (and friction) only plays a role when most of the motifs are already transformed/collapsed. Overall, as it is evident in Figure B15, friction seems to play a minor role in full compression and $\mu = 0.1$ is reasonable assumption to made for FE simulation.

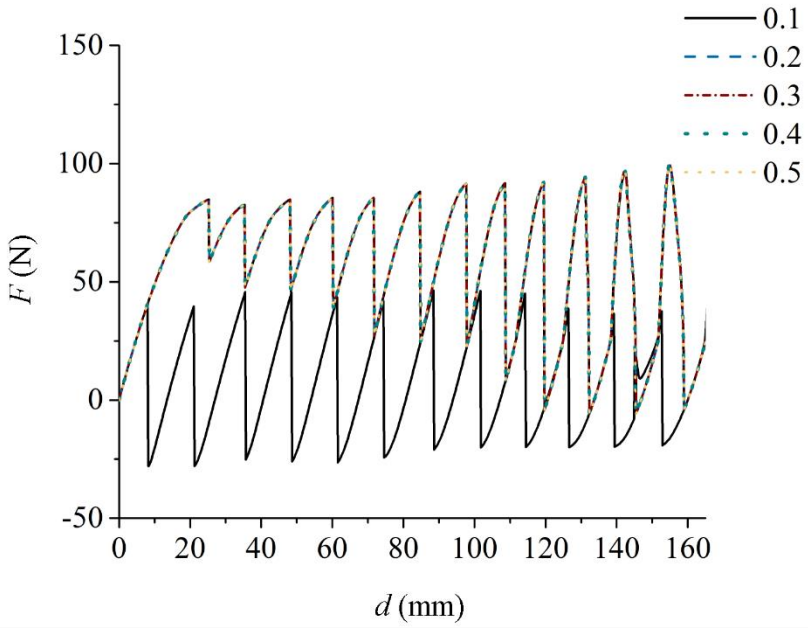

Figure B15: *F-d* relationship of a *S-type* PXCM sample under the loading angle {0°, 90°} with different friction coefficient.

B4.4. Base material properties

Three-point bending tests are conducted to determine mechanical properties of the base material. Test setup is shown in Figure B16 a. Four increasing load-unload cycles are applied on three

samples as shown in Figure B16 b. Sample B1 and B2 have identical cross section areas (i.e., 0.7 mm × 25 mm) compared with the elementary mechanism of 2D PXCMs. Sample S1 also has the same thickness 0.7 mm, but half of the width (i.e. 13 mm) compared with 2D PXCMs (Table B9) Figure B16 b shows the *F-d* relation of sample B2 under four increasing displacement load-unload cycles.

During the first two load-unload cycles, the sample exhibits approximately linear elastic behavior. A plateau is reached when the strain increases to 0.9% and 1.2% at cycle 3 and 4 which indicates that the base material exhibits nonlinear behavior under the large strain. However, for simplicity, we assume a linear elastic material model for the FE simulations, where the modulus is derived from the zero-strain tangent to the *F-d* curves obtained from a 3-point bending test (Table B10). This simplification allows us to capture the essential mechanics of the material behavior in a computationally efficient manner, but it sacrifices the accuracy of the force prediction. This factor could cause the FE models to overestimate the mechanical response of the PXCMs compared with the experiments. To assess the uncertainties introduced by this approach we develop FE models of all four 2D PXCMs samples where we assign a minimum, average and maximum elastic modulus. Such analysis can provide lower and upper bounds on the *F-d* curves are displayed in Figure B17. The energy dissipation calculated in each sample is summarized in Table B11. Due to the uncertainty of elastic modulus of base material, assuming all the 2D PXCM samples have a constant elastic modulus can cause the energy dissipation capacity of these materials varies from -6% to 7%.

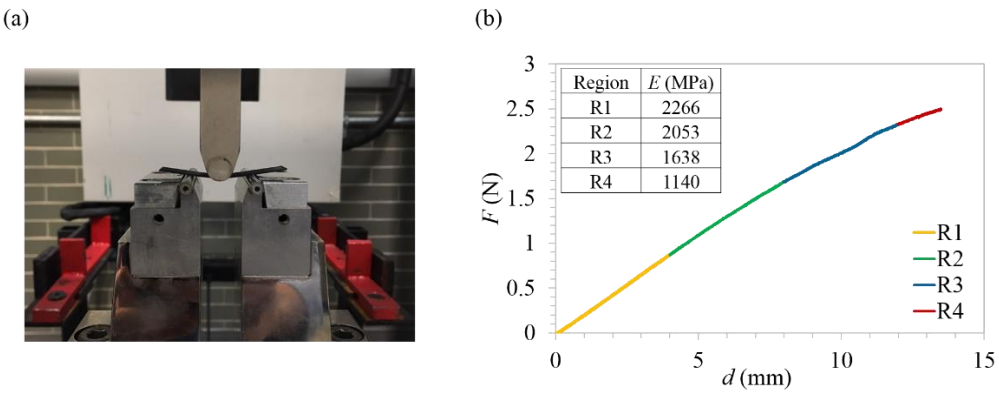

Figure B16: Three-point bending test to determine material properties of the base materials. (a) Experiment setup. (b) Applied displacement and reaction force vary with time. (c)-(f) *F-d* relation of sample under different load-unload cycles.

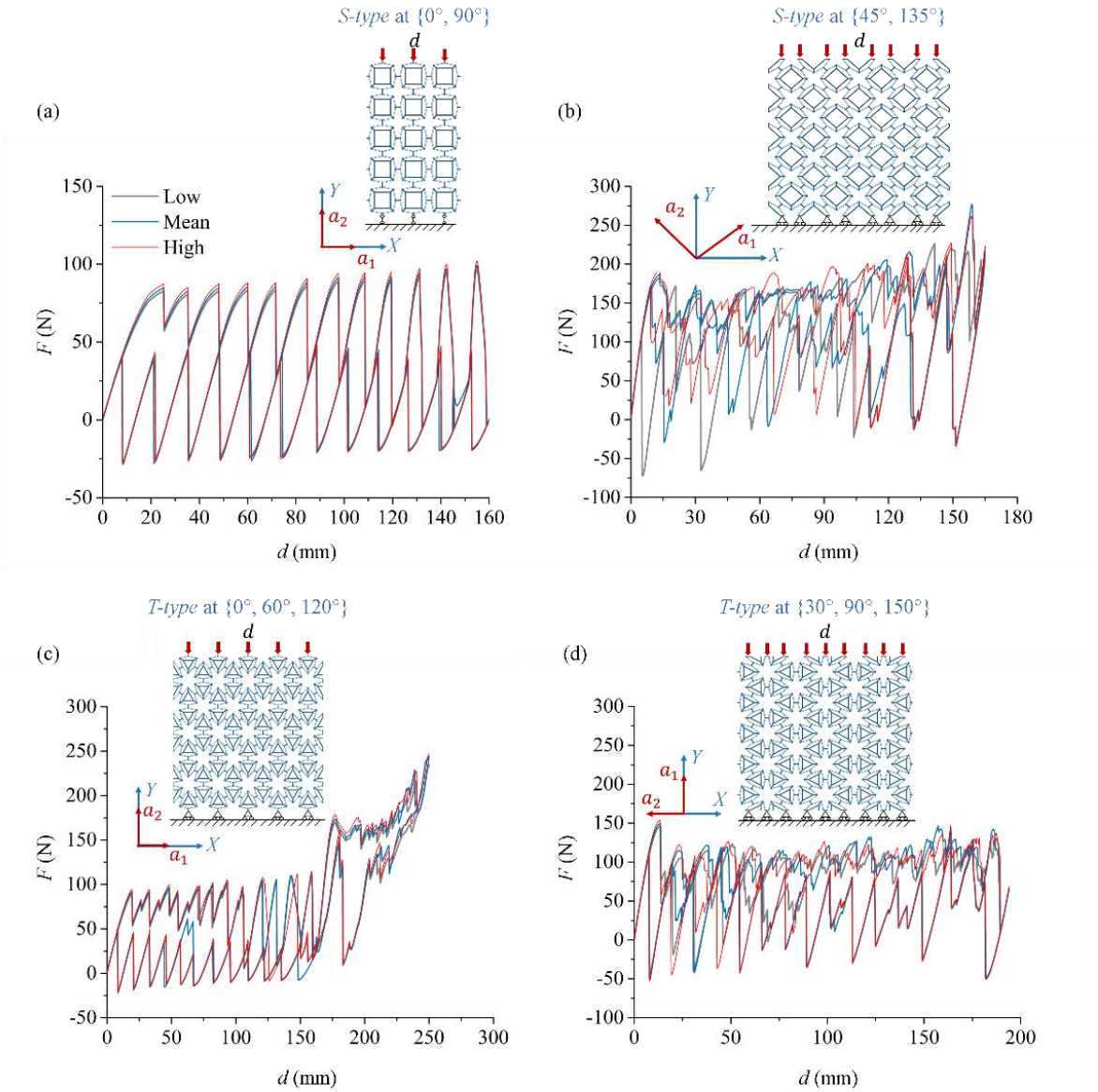

Figure B17: *F-d* relation of 2D PXCMs with minimum, average, and maximum base materials properties. (a) A *S-type* PXCM sample under three compressive load-unload cycle at {0°, 90°}. (b) A *S-type* PXCM sample under three compressive load-unload cycle at {45°, 135°}. (c) A *T-type* PXCM sample under three compressive load-unload cycle at {0°, 60°, 120°}. (d) A *T-type* PXCM sample under three compressive load-unload cycle at {30°, 90°, 150°}.

B5. Energy dissipation rate

Energy dissipation rate is another important factor for engineering applications. To understand the how loading angle influence the energy dissipation rate in 2D PXCMs, we plot the energy dissipation for four samples as a function of the applied displacement. Energy dissipation in PXCMs occurs in a discontinuous way through discrete steps corresponding to snap-through

transitions in individual building blocks. However, we can define an average energy dissipation rate in the following way: we load the material up to a snap-through at a displacement and then unload it completely. As such the average energy dissipation rate, at that given displacement, can be defined as the ratio between the energy dissipated in this complete load-unload cycle and the applied displacement. This is repeated for all snap-through events to get the average energy dissipation rate for different displacement values through its loading history. For this we use all the data from Figure 5.3 to Figure 5.6. These *F-d* curves can be discretized into cycles. Each cycle starts form the initial state, loads to a snap back point and then unloads back to the initial state (Figure B18a). The initial stiffness is used to extrapolate the unloading path after snap back happens. Figure B18 a demonstrates the first loading and loading cycle as an example. S0 represents *S-type* PXCM under loading angle {0°, 90°}, S45 represents *S-type* PXCM under loading angle {45°, 135°}, T0 represents *T-type* PXCM under loading angle {0°, 60°, 120°}, and T90 T0 represents *T-type* PXCM under loading angle {30°, 90°, 150°}. T0 exhibits two distinguished regions therefore named by T0-1 and T0-2. Energy dissipation rate per unit volume and unit mass are used to evaluate the performance of 2D PXCMs under different loading directions (Figure 5.7 c and Figure B18b). Both plots show *S-type* PXCM loaded at {45°, 135°}, *T-type* PXCM loaded at {30°, 90°, 150°}, and the first region for *T-type* PXCM loaded at {0°, 60°, 120°} show the similar energy dissipation rate. *S-type* PXCM under loading angle {0°, 90°} shows higher energy dissipation rate. *T-type* PXCM is not sensitive to the loading direction compared with *S-type* PXCM. To have explicit comparison, liner interpolation is used to quantify the energy dissipation per unit value and mass varies with applied displacement. Linearized curves are shown in Figure B18c-d and the slope of each sample is displayed in Table B12. It shows that before *T-type* PXCM loaded from {0°, 60°, 120°} enter the second region, *T-type* PXCM has identical energy dissipation rate per unit volume and mass under a load comes from any the reflectional axes of symmetry. The energy dissipation rate for *T-type* PXCM is about two third of the one calculated for the *S-type* PXCM under at {0°, 90°}. The *S-type* at {45°, 135°}, shows 23% higher energy dissipation rate compared with the *T-type* PXCM. Once loading *T-type* PXCM along {0°, 60°, 120°} to the second region, the energy dissipation rate reduces to half. Overall, *S-type* PXCM loaded under {0°, 90°} shows highest energy dissipation rate compared to the other cases. The *S-type* at {45°, 135°} and *T-type* PXCM under all the loading angles show similar energy dissipation rate until *T-type* PXCM enters the second region under the loading direction {0°, 60°, 120°}.

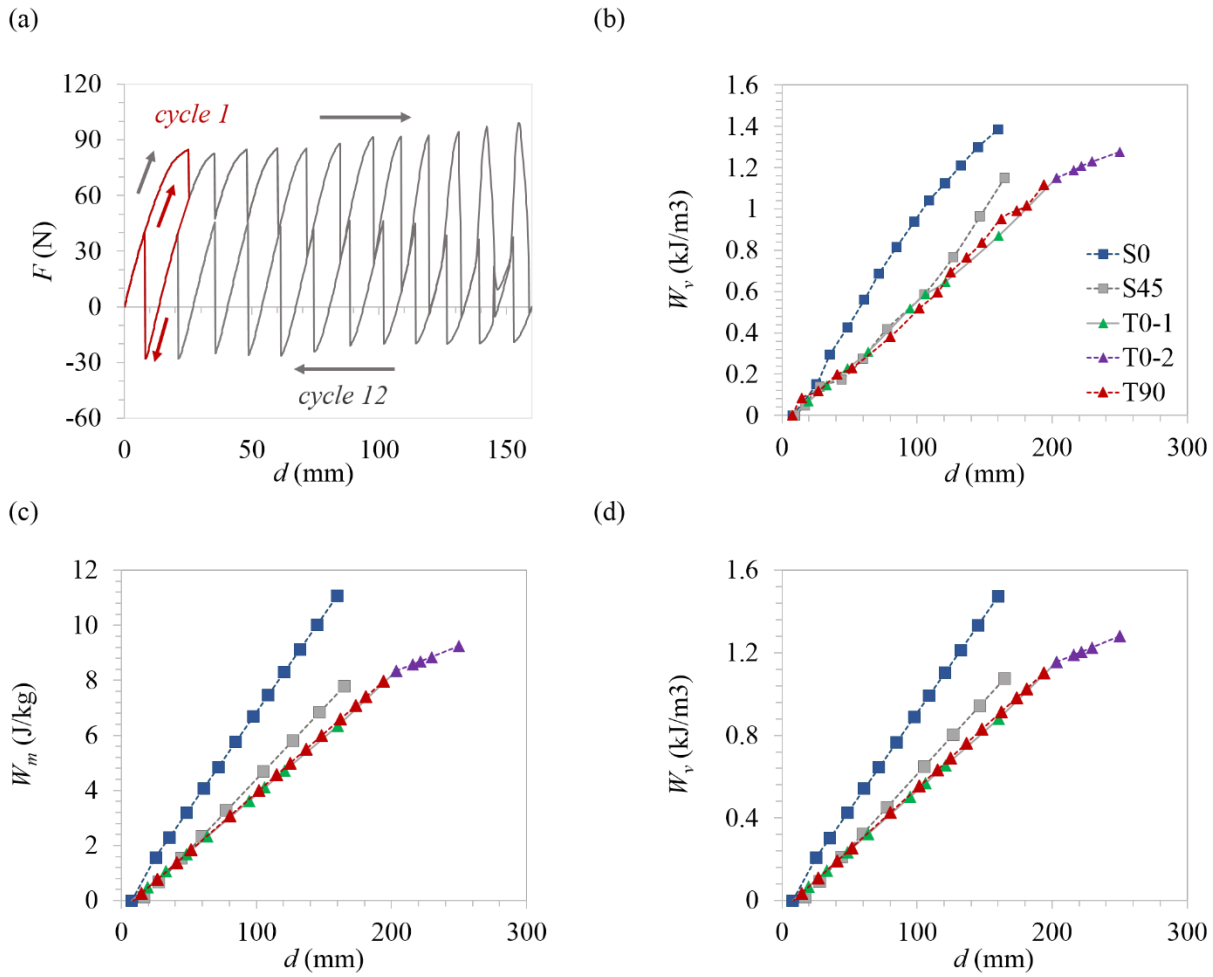

Figure B18: Energy dissipation rate of *T-type* PXCM is not sensitive to loading direction. *S-type* PXCM shows higher energy dissipation rate when load comes along the 0° compared with 45°. (a) Demonstrate energy dissipation of cycle 1 and cycle 12. (b) Energy dissipation per unit volume of four samples varies with time. (c)-(d) Energy dissipation per unit mass and per unit volume of four samples varies with time after linear curve fitting.

B6. Biaxail loading condition

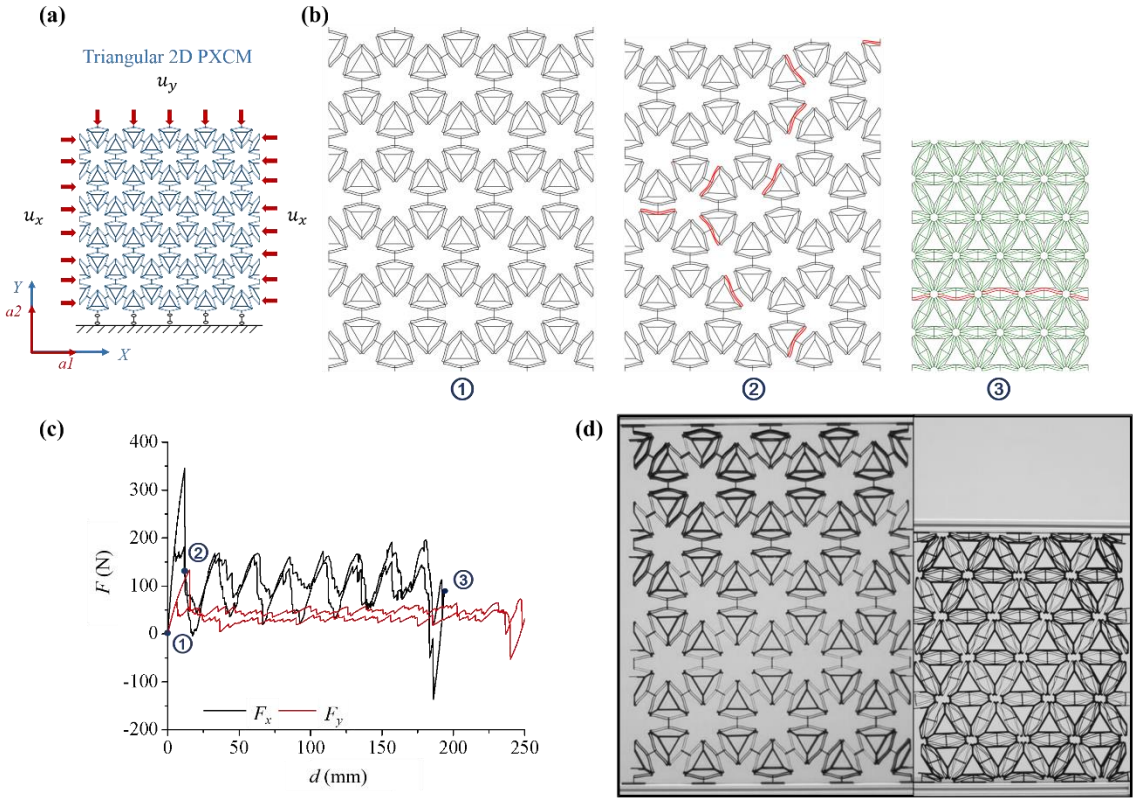

Figure B19: Performance of a *T-type* PXCM sample under one biaxial compressive load-unload cycle. (a) The sample is under uniaxial loading condition and supported by rollers at bottom. (b) Phase transformation sequence of the three characteristic states from FE simulation. (c). *F-d* relation of the sample from FE simulation and Experiment. (d) Two states of the sample corresponding to initial and final deformed configurations.

We created FE simulations to investigate the response of a *T-type* PXCM under biaxial loading condition. The schematic for this load case is shown in Figure B19a where the a_1 axis is aligned with the *X*-axis and a_2 axis is aligned with the *Y*-axis. To ensure all the building blocks achieve phase transformation at the same time, the loading rate in the *X* direction is 0.39 mm/min and in *Y* direction is 1 mm/min. Figure B19b shows the undeformed and deformed configurations of the sample at three salient points during its compression as obtained from the finite element simulations. The corresponding points are labelled on the *F-d* response in Figure B19c. The sinusoidal beams are color coded according to their status at any point during the deformation process. The beams rendered in gray are still in phase 1 (according to the definition in Design Considerations section Figure 5.1b) , those shaded green have already transformed to phase 2, and the red ones are undergoing phase transformation.

Unlike the response of *T-type* PXCM under the uniaxial loading condition, all the building blocks undergo phase transformation under the biaxial loading condition. Expect at loading-unloading transition point, *T-type* PXCM exhibits higher serrated loading and unloading plateau force in the *X* direction than in the *Y* direction. The peak force is reduced to around 50% in both *X* and *Y* directions after the first building block transformed (See Figure B19c). The ratio of energy dissipation capacity of in *X* to *Y* direction is 1.3 (Table B13 and video 6).

B7. Tables

Table B1: Values assigned to various design parameters in Figure 5.2

Parameters	Dimension (mm)
t	0.7
t'	0.7
t_{stiff}	4.2
$t_{central}$	2.1
s	3.5
A	7
λ	71

Table B2: The volume of the undeformed the samples.

Specimen Name	Size (mm^3)
S-type 0°	6125000
S-type 45°	10400625
T-type 0°	11041875
T-type 90°	11041875

Table B3: Summary of energy dissipation of four samples under the three compressive load-unload cycles.

Specimen	Cycle	Dissipated Energy (Nmm)	Variation (%)
T-type 0°	1	15017	5%
	2	14043	-2%
	3	13894	-3%
Average		14318	
T-type 90°	1	13426	5%
	2	12689	-1%
	3	12265	-4%
Average		12793	
S-type 0°	1	7189	6%
	2	6366	-6%
	3	6823	0.5%
Average		6792	
S-type 45°	1	11016	8%
	2	10218	0.1%
	3	9402	-8%
Average		10212	

Table B4: Energy dissipation varies slightly among cycle 2 and 3.

Sample	Cycle	Dissipated Energy (Nmm)	Variation (%)
T-type 0°	2	12689	1.7%
	3	12265	-1.7%
Avg. cycle 2&3		12477	
T-type 90°	2	14043	0.5%
	3	13894	-0.5%
Avg. cycle 2&3		13969	
S-type 0°	2	6366	-3.5%
	3	6823	3.5%
Avg. cycle 2&3		6595	
S-type 45°	2	10218	4.2%
	3	9402	-4.2%
Avg. cycle 2&3		9810	

Table B5: Energy dissipation per unit volume of 2D PXCMs and 1D PXCMs along different loading angles corresponding to their axes of symmetry.

T-type PXCM				*S-type* PXCM				1D PXCM	
Experiment		FEA		*Experiment*		*FEA*		FEA	
Angle	W_v	Angle	W_v	Angle	W_v	Angle	W_v	Angle	W_v
°	kJ/m^3	°	kJ/m^3	°	kJ/m^3	°	kJ/m^3	°	kJ/m^3
0	1.27	0	1.28	0	1.08	0	1.39	0	3.32
30	1.11	30	1.12	45	0.94	45	1.15	180	3.32
60	1.27	60	1.28	90	1.08	90	1.39		
90	1.11	90	1.12	135	0.94	135	1.15		
120	1.27	120	1.28	180	1.08	180	1.39		
150	1.11	150	1.12	225	0.94	225	1.15		
180	1.27	180	1.28	270	1.08	270	1.39		
210	1.11	210	1.12	315	0.94	315	1.15		
240	1.27	240	1.28	360	1.08	360	1.39		
270	1.11	270	1.12						
300	1.27	300	1.28						
330	1.11	330	1.12						
360	1.27	360	1.28						

Table B6: Energy dissipation per unit mass of 2D PXCMs and 1D PXCMs along different loading angles corresponding to their axes of symmetry.

T-type PXCM				*S-type* PXCM				1D PXCM	
Experiment		FEA		*Experiment*		FEA		FEA	
Angle	W_m	Angle	W_m	Angle	W_m	Angle	W_m	Angle	W_m
°	J/kg	°	J/kg	°	J/kg	°	J/kg	J/kg	J/kg
0	10.49	0	9.21	0	9.49	0	10.42	0	21.60
30	9.26	30	8.07	45	7.82	45	8.34	180	21.60
60	10.49	60	9.21	90	9.49	90	10.42		
90	9.26	90	8.07	135	7.82	135	8.34		
120	10.49	120	9.21	180	9.49	180	10.42		
150	9.26	150	8.07	225	7.82	225	8.34		
180	10.49	180	9.21	270	9.49	270	10.42		
210	9.26	210	8.07	315	7.82	315	8.34		
240	10.49	240	9.21	360	9.49	360	10.42		
270	9.26	270	8.07						
300	10.49	300	9.21						
330	9.26	330	8.07						
360	10.49	360	9.21						

Table B7: The energy dissipated by the entire sample in cycles 2 – 3.

Sample 1			
Cycle	*Ed* (mJ)	*Ea* (mJ)	*Ed/Ea*
2	50.5	164.1	31%
3	21.1	130.2	16%

Table B8: The energy dissipated by the entire sample in cycles 2 – 4.

Sample 2			
Cycle	*Ed* (mJ)	*Ea* (mJ)	*Ed/Ea*
2	17.91	119.68	15%
3	17.45	117.66	15%
4	17.26	116.15	15%

Table B9: Dimension of three-point bending test samples.

Sample	L (mm)	t (mm)	w (mm)
S1	24	0.7	13
B1	72	0.7	25
B2	73	0.7	25

Table B10: Summary of three-point bending tests.

	Cycle	d_{max} (mm)	m	ε_{max}	E_0 (MPa)
S1	1	1.2	3.12	0.9%	2303
	2	2.4	3.16	1.8%	2333
	3	3.7	3.01	2.7%	2222
	4	4.9	3.00	3.6%	2212
B1	1	3.6	0.23	0.3%	2220
	2	7.2	0.23	0.6%	2224
	3	10.9	0.23	0.9%	2228
	4	14.5	0.23	1.2%	2228
B2	1	3.7	0.22	0.3%	2266
	2	7.3	0.22	0.6%	2316
	3	11.0	0.22	0.9%	2325
	4	14.6	0.22	1.2%	2330
Min		1.224	0.219	0.003	2212
Average		7.076	1.174	0.012	2267
Max		14.601	3.160	0.036	2333

Table B11: Energy dissipation of four 2D PXCM samples with base material has minimum, average, and maximum elastic modulus.

Sample	Elastic Modulus	Dissipated Energy (Nmm)	Variation (%)
T-type 0°	E_{min}	13434	-1%
	E_{mean}	13729	1%
	E_{max}	13461	-1%
Average		13541	
T-type 90°	E_{min}	11067	-6%
	E_{mean}	12029	2%
	E_{max}	12379	5%
Average		11825	
S-type 0°	E_{min}	8134	-2%
	E_{mean}	8260	-1%
	E_{max}	8582	2%
Average		8325	
S-type 45°	E_{min}	13530	7%
	E_{mean}	11940	-6%
	E_{max}	12524	-1%
Average		12665	

Table B12: Energy dissipation rate *S*- and *T-type* 2D PXCMs.

Sample	Energy dissipation rate	
	per unit mass	per unit volume
S0	0.071	0.0094
S45	0.052	0.0071
T0-1	0.042	0.0058
T0-2	0.019	0.0027
T-90	0.043	0.0060

Table B 13: Energy dissipation capacity of *T-type* PXCM under biaxial loading condition.

Direction	W (Nmm)	W_v (kJ/m^3)	W_m (J/kg)
X	6892.2	0.727	6.335
Y	5191.3	0.547	4.772

B8. List of Videos

Video 1: Functionally 2D Phase Transforming Cellular Materials (PXCMs)- *S-Type* at 0 degrees

Performance of a *S-type* PXCM sample under one compressive load-unload cycle at {0°, 90°}. (a) The sample is under uniaxial loading condition and supported by rollers at bottom. (b) Phase transformation sequence of the three characteristic states from FE simulation. (c). *F-d* relation of sample from FE simulation and Experiment. (d) The states of the sample at initial and final deformed configurations.

https://youtu.be/7SSe4m_OH_w

Video 2: Functionally 2D Phase Transforming Cellular Materials (PXCMs)- *S-Type* loaded at 45 degree

Performance of a *S-type* PXCM sample under one compressive load-unload cycle at {45°, 135°}.The sample is under uniaxial loading condition and supported by rollers at bottom. Phase transformation sequence of the three characteristic states from FE simulation vs. experiments. *F-d* relation of sample from FE simulation and Experiment.

https://youtu.be/jm_lTxPArf0

Video 3: Functionally 2D Phase Transforming Cellular Materials (PXCMs)- *T-Type* loaded at 0 degree

Performance of a *T-type* PXCM sample under one compressive load-unload cycle at {0°, 60°, 120°}. The sample is under uniaxial loading condition and supported by rollers at bottom. Phase transformation sequence of the three characteristic states from FE simulation vs. Experiments. *F-d* relation of sample from FE simulation and Experiment.

https://youtu.be/LZagL31YR3g

Video 4: Functionally 2D Phase Transforming Cellular Materials (PXCMs)- *T-Type* loaded at 90 degree

Performance of a *T-type* PXCM sample under one compressive load-unload cycle at {0°, 60°, 120°}. The sinusoidal beams are color coded according to their status at that point in the deformation. The beams rendered in gray are still in phase 1, those shaded green have already transformed to phase 2, and the red ones are undergoing phase transformation.

https://youtu.be/m2gCBAmHu0Q

Video 5: Functionally 2D Phase Transforming Cellular Materials (PXCMs)- *T-Type* loaded at 90 degree

Performance of a *T-type* PXCM sample under one compressive load-unload cycle at {30°, 60°, 120°}. The sample is under uniaxial loading condition and supported by rollers at bottom. Phase transformation sequence of the three characteristic states from FE simulation vs. experiments. *F-d* relation of sample from FE simulation and Experiment.

https://youtu.be/ENMFlFrS88E

Video 6: Functionally 2D Phase Transforming Cellular Materials (PXCMs)- *T-Type* under biaxial conditions

Performance of a *T-type* PXCM sample under biaxial conditions

https://youtu.be/uZlHEX4vsOI

Video 7: Functionally 2D Phase Transforming Cellular Materials (PXCMs)- *S-Type* loaded at 0, 90, 45, and 135 degrees

Performance of a *S-type* PXCM sample under one compressive load-unload cycle at {0°, 90°} and {45°, 135°}. The sample is under uniaxial loading condition and supported by rollers at bottom. Phase transformation sequence of the three characteristic states from FE simulation vs. experiments. *F-d* relation of sample from FE simulation and Experiment.

https://youtu.be/TnrUo72rxkk

Video 8: Functionally 2D Phase Transforming Cellular Materials (PXCMs)- *T-Type* PXCM with single sinusoidal beam as building block and spokes inside motifs loaded at 0, 30, 60, 90, 120, and 150 degrees

Performance of a *T-type* PXCM sample under one compressive load-unload cycle at {0°, 60°, 120°} and {30°, 90°, 150°}. *T-Type* PXCM with single sinusoidal beam as building block and spokes inside motifs.

https://youtu.be/czDJqA1Pfns

REFERENCES

1. Duerig, T. W., Stöckel, D. & Keeley, A. *Actuator and Work Production Devices*. *Engineering Aspects of Shape Memory Alloys* (Butterworth-Heinemann Ltd, 2013).
2. Shaw, J. A., Churchill, C. B., Lagoudas, D. C. & Kumar, P. Shape Memory Alloys. 1–20 (2010).
3. Sirohi, J. & Chopra, I. Fundamental understanding of piezoelectric strain sensors. *J. Intell. Mater. Syst. Struct.* **11**, 246–257 (2000).
4. Sullivan, T. N., Zhang, Y., Zavattieri, P. D. & Meyers, M. A. Hydration-Induced Shape and Strength Recovery of the Feather. *Adv. Funct. Mater.* **28**, 1–9 (2018).
5. Liu, Z. Q., Jiao, D. & Zhang, Z. F. Biomaterials Remarkable shape memory effect of a natural biopolymer in aqueous environment. *Biomaterials* **65**, 13–21 (2015).
6. Guo, Q. *et al.* Fast nastic motion of plants and bioinspired structures. *J. R. Soc. Interface* **12**, (2015).
7. Khandelwal, A. & Buravalla, V. Models for Shape Memory Alloy Behavior: An overview of modeling approaches. *Int. J. Struct. Chang. Solids* **1**, 111–148 (2009).
8. Wayman, C. M. & Duerig, T. W. An Introduction to Martensite and Shape Memory. *Eng. Asp. Shape Mem. Alloy.* 3–20 (1990).
9. Kheirikhah, M. M., Rabiee, S. & Edalat, M. E. *A review of shape memory alloy actuators in robotics*. *Lecture Notes in Computer Science (including subseries Lecture Notes in Artificial Intelligence and Lecture Notes in Bioinformatics)* **6556 LNAI**, (2011).
10. Machado, L. G. & Savi, M. A. Medical applications of shape memory alloys. *Brazilian J. Med. Biol. Res.* **36**, 683–691 (2003).
11. Wilde, K., Gardoni, P. & Fujino, Y. Base isolation system with shape memory alloy device for elevated highway bridges. *Eng. Struct.* **22**, 222–229 (2000).
12. Song, G., Ma, N. & Li, H. N. Applications of shape memory alloys in civil structures. *Eng. Struct.* **28**, 1266–1274 (2006).
13. Brinkmeyer, A., Santer, M., Pirrera, A. & Weaver, P. M. Pseudo-bistable self-actuated domes for morphing applications. *Int. J. Solids Struct.* **49**, 1077–1087 (2012).
14. Brinkmeyer, A., Pirrera, A., Santer, M. & Weaver, P. M. Pseudo-bistable pre-stressed morphing composite panels. *Int. J. Solids Struct.* **50**, 1033–1043 (2013).

15. Zhao, Q. *et al.* A bioinspired reversible snapping hydrogel assembly. *Mater. Horizons* **3**, 422–428 (2016).
16. Mao, Y. *et al.* 3D Printed Reversible Shape Changing Components with Stimuli Responsive Materials. *Sci. Rep.* **6**, 24761 (2016).
17. Wu, J. *et al.* Multi-shape active composites by 3D printing of digital shape memory polymers. *Sci. Rep.* **6**, 1–11 (2016).
18. Yang, C. *et al.* 4D printing reconfigurable, deployable and mechanically tunable metamaterials. *Mater. Horizons* (2019).
19. Restrepo, D., Mankame, N. D. & Zavattieri, P. D. Phase transforming cellular materials. *Extrem. Mech. Lett.* **4**, 52–60 (2015).
20. Frenzel, T., Findeisen, C., Kadic, M., Gumbsch, P. & Wegener, M. Tailored Buckling Microlattices as Reusable Light-Weight Shock Absorbers. 5865–5870 (2016).
21. Findeisen, C., Hohe, J., Kadic, M. & Gumbsch, P. Journal of the Mechanics and Physics of Solids Characteristics of mechanical metamaterials based on buckling elements. **102**, 151–164 (2017).
22. Debeau, D. A., Seepersad, C. C. & Haberman, M. R. Impact behavior of negative stiffness honeycomb materials. *J. Mater. Res.* **33**, 290–299 (2018).
23. Ha, C. S., Lakes, R. S. & Plesha, M. E. Design , fabrication , and analysis of lattice exhibiting energy absorption via snap-through behavior. *Mater. Des.* **141**, 426–437 (2018).
24. Pontecorvo, M. E., Barbarino, S., Murray, G. J. & Gandhi, F. S. Bistable arches for morphing applications. *J. Intell. Mater. Syst. Struct.* **24**, 274–286 (2013).
25. Haghpanah, B., Salari-Sharif, L., Pourrajab, P., Hopkins, J. & Valdevit, L. Architected Materials: Multistable Shape-Reconfigurable Architected Materials (Adv. Mater. 36/2016). *Adv. Mater.* **28**, 8065 (2016).
26. Che, K. & Qi, H. J. Three-Dimensional-Printed Multistable Mechanical Metamaterials With a Deterministic Deformation Sequence. **84**, 1–10 (2018).
27. Shan, S. *et al.* Multistable Architected Materials for Trapping Elastic Strain Energy. 4296–4301 (2015).
28. Ren, C., Yang, D. & Qin, H. Mechanical Performance of Multidirectional Buckling-Based Negative Stiffness Metamaterials : An Analytical and Numerical Study. (2018).

29. Prasad, J. & Diaz, A. R. Synthesis of Bistable Periodic Structures Using Topology Optimization and a Genetic Algorithm. *J. Mech. Des.* **128**, 1298 (2006).
30. Danso, L. A. & Karpov, E. G. Cusp singularity-based bistability criterion for geometrically nonlinear structures. *Extrem. Mech. Lett.* **13**, 135–140 (2017).
31. Rafsanjani, A. & Pasini, D. Bistable auxetic mechanical metamaterials inspired by ancient geometric motifs. *Extrem. Mech. Lett.* **9**, 291–296 (2016).
32. Silverberg, J. L. *et al.* Using origami design principles to fold reprogrammable mechanical metamaterials. *Science (80-.).* **345**, 647–650 (2014).
33. Babaee, S. *et al.* 3D soft metamaterials with negative poisson's ratio. *Adv. Mater.* **25**, 5044–5049 (2013).
34. Santer, M. & Pellegrino, S. Compliant multistable structural elements. *Int. J. Solids Struct.* **45**, 6190–6204 (2008).
35. Correa, D. M., Seepersad, C. C. & Haberman, M. R. Mechanical design of negative stiffness honeycomb materials. *Integr. Mater. Manuf. Innov.* **4**, 8 (2015).
36. Shan, S. *et al.* Multistable Architected Materials for Trapping Elastic Strain Energy. *Adv. Mater.* **27**, 4296–4301 (2015).
37. Rafsanjani, A. & Pasini, D. Bistable auxetic mechanical metamaterials inspired by ancient geometric motifs. *Extrem. Mech. Lett.* **9**, 291–296 (2016).
38. Qiu, J. An Electrothermally-Actuated Bistable MEMS Relay for Power Applications. *Massachusetts Inst. Technol.* 94 (2003).
39. Qiu, J., Lang, J. H. & Slocum, A. H. a Curved Beam Bistable Mechanism Bi Stable Beam Model. **13**, 137–146 (2004).
40. Pennycuick, C. J. *Modelling the Flying Bird*. (2008).
41. Wang, B., Yang, W., McKittrick, J. & Meyers, M. A. Keratin: Structure, mechanical properties, occurrence in biological organisms, and efforts at bioinspiration. *Prog. Mater. Sci.* **76**, 229–318 (2016).
42. Wang, B. & Meyers, M. A. Light like a feather: A fibrous natural composite with a shape changing from round to square. *Adv. Sci.* **4**, 1–10 (2017).
43. McKittrick, J. *et al.* The structure, functions, and mechanical properties of keratin. *Jom* **64**, 449–468 (2012).

44. Laurent, C. M. *et al.* Nanomechanical properties of bird feather rachises : exploring naturally occurring fibre reinforced laminar composites. (2014).
45. Zhang, Y., Restrepo, D., Velay-lizancos, M. & Mankame, N. D. Energy dissipation in functionally two-dimensional phase transforming cellular materials. *Sci. Rep.* 1–11 (2019).
46. Hector, K. W., Restrepo, D., Bonilla, C. T., Hector, L. G. & Zavattieri, P. D. Mechanics of Chiral Honeycomb Architectures With Phase Transformations. **86**, 1–15 (2019).
47. M.F. Ashby, A.G. Evans, N.A. Fleck, L.J. Gibson, Wadley, J.W. Hutchinson, and H. N. G. W. Making metal foams. *Met. Foam.* 6–23 (2000).
48. Correa, D. M. *et al.* Negative stiffness honeycombs for recoverable shock isolation. *Rapid Prototyp. J.* **21**, 193–200 (2015).
49. Shaw, J. A. & Kyriakides, S. Thermomechanical aspects of NiTi. *J. Mech. Phys. Solids* **43**, 1243–1281 (1995).
50. Rief, M., Gautel, M., Oesterhelt, F., Fernandez, J. M. & Gaub, H. E. Reversible Unfolding of Individual Titin Immunoglobulin {Domains} by AFM. *Science (80-.).* **276**, 1109–1112 (1997).
51. Benichou, I. & Givli, S. Structures undergoing discrete phase transformation. *J. Mech. Phys. Solids* **61**, 94–113 (2013).
52. Hopkins, J. B., Lange, K. J. & Spadaccini, C. M. Designing Microstructural Architectures With Thermally Actuated Properties Using Freedom , Actuation , and Constraint Topologies. **135**, (2019).
53. Jonathan, B., Link, C. & Lee, H. Polytope Sector-Based Synthesis and Analysis of Microstructural Architectures With Tunable Thermal Conductivity and Expansion. (2019).
54. Lakes, R. S. & Elms, K. Indentability of Conventional and Negative Poisson's Ratio Foams. *J. Compos. Mater.* **27**, 1193–1202 (1993).
55. Saxena, K. K., Das, R. & Calius, E. P. Three Decades of Auxetics Research − Materials with Negative Poisson's Ratio: A Review. *Adv. Eng. Mater.* **18**, 1847–1870 (2016).
56. Ali, M. N., Busfield, J. J. C. & Rehman, I. U. Auxetic oesophageal stents: Structure and mechanical properties. *J. Mater. Sci. Mater. Med.* **25**, 527–553 (2014).
57. Papadopoulou, A., Laucks, J. & Tibbits, S. Auxetic materials in design and architecture. *Nat. Rev. Mater.* **2**, 17078 (2017).

58. Rafsanjani, A., Akbarzadeh, A. & Pasini, D. Snapping Mechanical Metamaterials under Tension. *Adv. Mater.* **27**, 5931–5935 (2015).
59. Che, K., Yuan, C., Wu, J., Jerry Qi, H. & Meaud, J. Three-Dimensional-Printed Multistable Mechanical Metamaterials With a Deterministic Deformation Sequence. *J. Appl. Mech.* **84**, 011004 (2016).
60. Haghpanah, B., Shirazi, A., Salari-Sharif, L., Guell Izard, A. & Valdevit, L. Elastic architected materials with extreme damping capacity. *Extrem. Mech. Lett.* **17**, 56–61 (2017).
61. Acrylonitrile Butadiene Styrene (ABS) Typical Properties Generic ABS | UL Prospector. Available at: https://plastics.ulprospector.com/generics/1/c/t/acrylonitrile-butadiene-styrene-abs-properties-processing.

VITA

Yunlan Zhang was born in Beijing, China. She received a bachelor's degree in Civil Engineering from The Ohio State University in 2013. She went on to pursue a coursework-only master's degree in Civil Engineering with an emphasis on Structural Engineering at Purdue University, which she received in May 2014. After her coursework-only master's degree, the author began the work for her Ph.D. dissertation, which she completed in December 2019.

PUBLICATIONS

Sullivan, T. N., Zhang, Y., Zavattieri, P. D. & Meyers, M. A. Hydration-Induced Shape and Strength Recovery of the Feather. Adv. Funct. Mater. 28, 1–9 (2018).

Zhang, Y., Enebechi, C. N., Hector, K., Carter, G., Grillo, V., Min, A., Restrepo, D., Mankame N. M. & Zavattieri, P. D. “Phase Transforming Cellular Materials (PXCMs) Simulator”, *https://nanohub.org/tools/pxcm/*, (2018).

Zhang, Y., Restrepo, D., Velay-lizancos, Mankame N. M. & Zavattieri, P. D. Energy dissipation in functionally two-dimensional phase transforming cellular materials. Sci. Rep. 1–11 (2019).